TECHNIQUES FOR DETERMINING HIDDEN PROPERTIES
OF LARGE-SCALE POWER SYSTEMS

BY

SAURAV MOHAPATRA

DISSERTATION

Submitted in partial fulfillment of the requirements
for the degree of Doctor of Philosophy in Electrical and Computer Engineering
in the Graduate College of the
University of Illinois at Urbana-Champaign, 2015

Urbana, Illinois

Doctoral Committee:

      Professor Thomas J. Overbye, Chair
      Professor Peter W. Sauer
      Associate Professor Deming Chen
      Dr. James D. Weber, PowerWorld Corporation
      Research Scientist Dr. Katherine M. R. Davis

ABSTRACT

The contributions in this dissertation are towards augmenting and enhancing the knowledge in power system equivalent modeling, and dynamic mode estimation. Work related to these respective topics is presented herein in two parts – (i) Network Based Methods, and (ii) Measurement Based Methods.

The first part focuses on the problem of creating limit preserving equivalents (LPEs). There is a push to develop LPEs for power system interconnections to be used in markets and reliability studies. The equivalents that exist for these interconnections do not capture thermal limits of equivalent lines, which results in their transmission limits being significantly different from the original interconnection limits. Assigning non-infinite and non-zero limits to equivalent lines is the niche of this work. This is done by considering an unloaded network, which is operating point independent. A solution method is developed and discussed, which is capable of assigning lower, best and upper estimates for equivalent line limits, and is proposed for use towards developing LPEs.

In the second part, a relatively new method for simultaneous modal analysis of multiple time-series signals is presented. Here, Dynamic Mode Decomposition (DMD) is successfully applied towards transmission-level power system measurements in an implementation that is able to run in real-time. Since power systems are considered as non-linear and time-varying, on-line modal identification is capable of monitoring the evolution of large-scale power system dynamics by providing a breakdown of the constituent oscillation frequencies and damping ratios, and their respective amplitudes. The outputs provided by DMD can enable on-line spatio-temporal analyses, improve situational awareness, and could even contribute towards control strategies. This work presents the theory of DMD, followed by results and visualization. It shows that using frequency and voltage data together helps with precision, while maintaining fast calculation speeds. The key advantage

of this implementation is its relatively fast computation; for example, it is able to process each time-window, consisting of 3392 signals with 211 time points, in 0.185 s. Modal content alarm processing, and efficient wide-area modal visualization are two proposed on-line applications.

The desire to reduce model-dependency has driven measurement-based modal identification methods, as an alternative to analyzing linearized system models. Using this relatively fast DMD algorithm, this work also presents an interactive modal-identification tool for spatio-temporal analysis of measurement data. The tool can automatically scan through measurements, and display the values of oscillation frequency and damping ratio, as well as reconstruct signals. The use of this tool, its options, and visualization capabilities are illustrated using simulated measurements from an interconnected power grid.

DMD being a data-driven modeling technique is able to handle large data sets and has shown fast computation times. The by-products of DMD provide an understanding of the wide-area spatio-temporal structures in power systems. Studies based on a large-scale model of an interconnected power grid are presented, along with visualizations that elucidate the spatial structure of wide-area dynamics, and their dependency on operating points.

To my parents and sister, for their love and support,

and

in loving memory of …
my grandfather, Gokula Nanda Mahapatra (1927-2004),
my grandmother, Sita Mahapatra (1937-2010),
and my aunt, Dr. Gayatri Mahapatra (1957-2006).

I will always treasure our relationship, and think on you with fond
memories, warm feelings, and a special place in my heart.
– "Doc", Back to the Future III

iv

ACKNOWLEDGMENTS

TABLE OF CONTENTS

CHAPTER 1

INTRODUCTION

Voltages, frequencies, power flows, and even locational marginal pricing are a few of the monitored quantities, or measurements, that can be obtained from electric power systems. These measurements contain hidden information, which could be traced to the physical attributes of an electric grid. Measurement-driven knowledge about electric power systems can be of value to power system operators and engineers. Due to the large volume of data being collected from interconnected power systems, it is likely that some identifiable characteristics might go unnoticed, or the degree of difference detected might seem impertinent at one location. This is where the notion of discovering hidden data, reinforced with concepts from data mining and wide-area power system modeling, is useful for improving existing practices in the industry. This thesis uses these concepts to contribute towards enhancing power system equivalents, and incorporating measurements into the current planning and operating procedures. This type of work could be thought of as a form of steganalysis, which is the study of detecting, as reliably as possible, the presence of hidden data [1], and then investigating it [2].

The spatial structure of interconnected power systems is a fascinating attribute. Figure 1.1 shows one such spatial aspect – the geo-spatial structure of the North American electric grid. From a graph-theory perspective, the lines/branches in the transmission and distribution networks can be thought of as edges, with the vertices being the buses/nodes. Depending on the modeling approach, i.e., bus-bar or node-breaker, the size and complexity of a power system model can greatly vary, with the latter being more complex. Regardless of the depth in modeling, the underlying spatial structure is a key characteristic that defines the power flow solution of a network.

Electrical parameters of transmission lines are a key spatial property of power systems, just like any electrical circuit. Kron [3] and Ward [4] developed techniques to mathematically manipulate and produce lower-order

1

Figure 1.1: An aerial illustration of the geo-spatial structure of the North American electric grid. Transmission lines at voltage levels higher than 160 kV have been artificially colored. Adapted from [6].

"equivalent" circuits that preserved certain electrical properties of a network, and hence were useful for implementing fast and reasonably accurate approximations to large network problems. With the advent of computer programming in finding solutions to network problems, Sato and Tinney developed efficient methods for obtaining and modifying the impedance matrix in their 1963 paper "Techniques for Exploiting the Sparsity of the Network Admittance Matrix" [5]. Several works in the field of static equivalent modeling and solution techniques are built on the fundamental contributions by Kron, Ward, Sato and Tinney, who had based their work on identifying and taking advantage of the spatial structure of networks. Researchers today continue to develop newer methods for power system equivalents, with the goal that additional or specific properties can be preserved. Part I of this thesis focuses on a spatially inspired solution to improve equivalent modeling.

To exploit the structure of a problem/system, it is required that the structure be known [7]. For example, Figure 1.2 shows the Jacobian matrix structure for a power flow problem. As seen, it is very sparse, and it is this sparsity that is taken advantage of during power flow solutions. There is also a type of equivalent modeling technique that retains the "backbone" of a power system by aggregating nodes based on their connectivity so that the
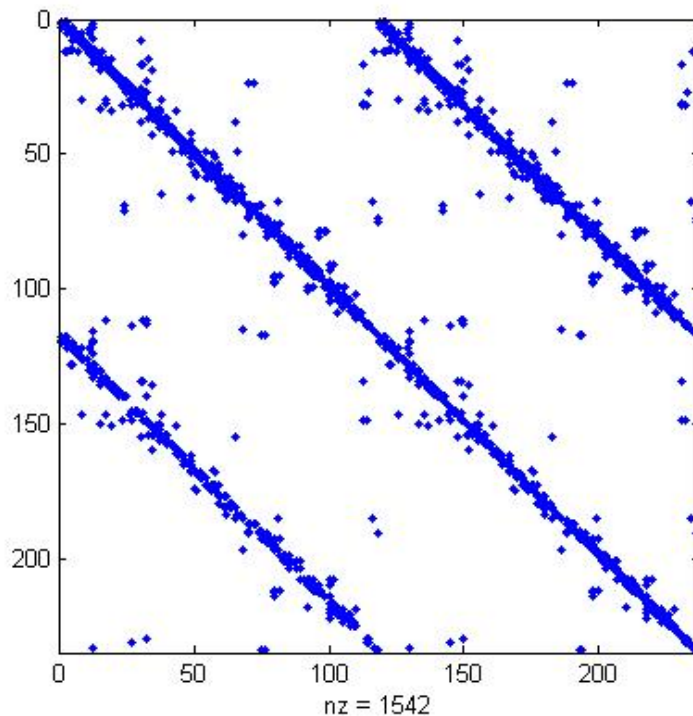
Figure 1.2: Sparse Jacobian matrix of a power flow.

macro-structure of the system can be preserved. However, the limit values of equivalent lines are lost while building equivalents. Since limit information for the equivalent is hidden in the original network, the work in Part I uses the understanding of spatial structures to assign line limits to the fictitious lines introduced during the equivalencing process. This allows the notion of network limits to be preserved in equivalent models.

Until now the discussion was on static attributes and spatial structures. However, electric grids are not always static. There are thousands of dynamic components that enable the proper operation and control required in interconnected power systems. During changing load patterns, or disturbances resulting from planned/unplanned events, these components respond, and hence power systems exhibit dynamic behavior. These dynamic properties can be modeled by a set of differential-algebraic equations (DAE), succinctly described as

3

$$\dot{\mathbf{x}} = \mathbf{f}(\mathbf{x}, \mathbf{y}, \mathbf{u}), \tag{1.1a}$$

$$\mathbf{0} = \mathbf{g}(\mathbf{x}, \mathbf{y}), \tag{1.1b}$$

where $\mathbf{x}$ is the vector of state variables, $\mathbf{y}$ is the vector of algebraic variables, and $\mathbf{u}$ is the vector of input variables.

This DAE model is generally nonlinear, both in terms of the first-order differential equations in (1.1a) and in terms of the algebraic equations in (1.1b). For the purpose of modeling in the transient stability time frame, the network is considered to be in quasi-steady state. Here, the interaction of states and phasor measurements (i.e., $\tilde{V} = |V|\angle\theta$) is less obvious, but does have a structure. Analogous to a power flow Jacobian in Figure 1.2, the Jacobian of a DAE model is shown in Figure 1.3. The spatial connectivity of the dynamic components with the electrical network can clearly be seen. It is this spatial connectivity, or rather a weighted version of it, which associates dynamic states to measurements of output signals. The notion of participation factors of states in observed modes present in power system measurements is well known from a model-driven perspective. The discussion of local and inter-area modes is also closely related to this.

Not very different is the notion of spatial topology that presents a network

Jacobian Matrix Structure
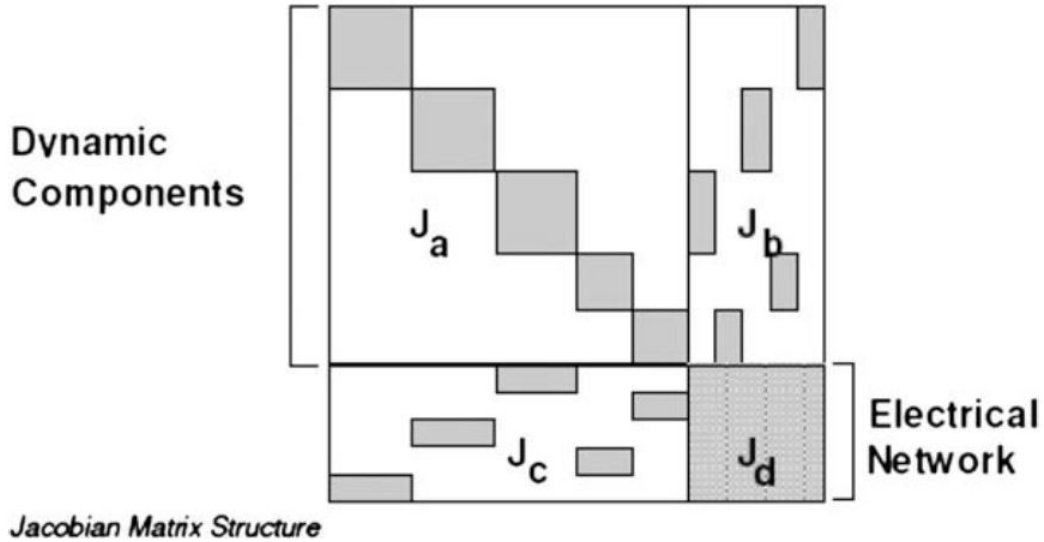
Figure 1.3: Structure of the Jacobian of differential-algebraic equations for a power system dynamic model.

view as to how the primary objects become interconnected via the contextual objects [8]. A DAE model can be thought of as consisting of dynamic objects that become mutually interdependent, due to an electrical network, which hence plays a significant role in the overall dynamic behavior of a power system.

In static equivalent modeling, the dominant contextual features of the electrical network are preserved, and that allows certain steady-state attributes to be captured in equivalents. These have also been augmented with methods that retain dynamic properties, hence resulting in dynamic equivalents. In contrast to model-driven analyses, there is a recent push to utilize high quality digital measurements that are now available from Phasor Measurement Units (PMUs), Frequency Disturbance Recorders (FDRs), and Digital Fault Recorders (DFRs), in addition to SCADA (Supervisory Control and Data Acquisition) measurements. It becomes more interesting to think about the inverse problem, given measurement signals from interconnected power systems. It is known that the underlying "context" of the electrical network coupled with the dynamic parameters of components defines dynamic behavior. However, is it possible to infer certain characteristics of the network and/or some dynamic parameters from wide-area measurements? A part of this question is tackled in Part II. This work presents a real-time measurement-driven modal identification technique, which is able to distill measurement datasets into one part that captures topology and a second part that captures temporal evolution. It is this separation of the topos and chronos that allows for fast modal identification and clear visualization. Various facets of the modal identification problem are discussed, and supported with studies and visualization of power system dynamic behavior. Of course, these measurement-driven methods could be augmented/reconciled with some knowledge from models, and that continues to be a research effort.

For clarity, the work in this thesis is divided into two parts, as each part tackles a different research problem. However the common theme of steganalysis binds this thesis together. The premise is that there is hidden information in power system data, which requires a mix of several approaches to uncover. The work in this dissertation corroborates this central idea, by utilizing techniques that help preserve or uncover seemingly hidden properties of large scale electric power systems.

5

1.1 Network Based Methods

The thesis begins with a focus on the "spatial" i.e. "network-related" characteristics of power systems. In particular, this part describes how certain key characteristics of power system networks can be preserved, while generating their reduced order models, or in other words power system equivalents. Equivalents of large, interconnected power system networks are commonly used to perform faster system analyses, such as security assessment, market simulations, etc. While creating equivalents, the characteristics to be preserved are application-specific. However, in general, the characteristics of interest are usually the ones that impact bulk system analysis and/or equivalent modeling.

The work presented here is a part of a project titled "Development of Attribute Preserving Network Equivalents." Prior work in this area provides algorithms to retain attributes such as line flows, locational marginal prices, etc. Similar to these, Part II of this thesis presents novel techniques that were developed to embed limit information in equivalents so that the physical constraints of lines are not forgotten, hence preserving the thermal limits of transmission lines – an important attribute that had not been considered so far in the literature.

1.2 Measurement Aided Methods

The second part of the thesis seeks to gain a better understanding of both the spatial and temporal behavior of interconnected power systems. This is done by implementing measurement-driven methods on power system time-series, dynamics data, corresponding to transient disturbances. A steganalysis based approach is taken to extract as much information as is detectable in the measurements. This work is a part of a project titled "Power Grid Spectroscopy." It focuses on tackling the inverse problem of understanding underlying power system behavior solely from measurements.

These measurement-based analysis methods were motivated by the field of fluid dynamics. The chapters in this part introduce a technique known as Dynamic Mode Decomposition (DMD), and propose various uses. Although DMD was first introduced in fluid mechanics, the work presented in this part

of the thesis presents the first known large-scale application of this fast and robust technique to power system modal analysis.

While the techniques presented here are based on measurement data, it does not imply that they are only suitable for model-less applications. It should be noted that they can be further enhanced by applying them in a model-augmented framework.

Part I

Network Based Methods

CHAPTER 2

LINE LIMIT PRESERVING POWER SYSTEM BACKBONE EQUIVALENT

Nomenclature

$$\Pi \quad = \quad \{\mathcal{B}, \mathcal{T}, \{y_{l\in\mathcal{T}}\}, \{F_{l\in\mathcal{T}}\}\}, \text{Unloaded power system network, consisting of buses, line connectivity, line admittances and line limits}$$

$$\mathcal{A} \quad = \quad \text{Set of all buses to be eliminated from a network}$$

$$\mathcal{E}_k \quad = \quad \text{Set of maximal adjacent buses, to be eliminated during stage } k \text{ of line limit calculation, such that } \bigcup\{\mathcal{E}_k\} = \mathcal{A} \text{ and } \mathcal{E}_i \cap \mathcal{E}_j = \emptyset, \text{ where } i \neq j$$

$$\mathcal{C} \quad = \quad \text{Set of buses to be eliminated during a stage of line limit calculation, } \mathcal{C} \subseteq \mathcal{A}$$

$$\mathcal{N} \quad = \quad \text{Set of lines in the pre-elimination network of a stage of line limit calculation}$$

$$\mathcal{S} \quad = \quad \{\text{Set of pre-elimination neighbor buses of } c \in \mathcal{C}\} \setminus \mathcal{C}$$

$$\mathcal{H} \quad = \quad \{l = (u,v) \mid u,v \in \mathcal{S}, u \neq v, l \in \mathcal{N}\}$$

$$\mathcal{L} \quad = \quad \{l = (u,v) \mid u,v \in \{\mathcal{C} \cup \mathcal{S}\}, u \neq v, l \in \{\mathcal{N} \setminus \mathcal{H}\}\}$$

$$y_l \quad = \quad \text{Admittance of } l \in \mathcal{L}, \text{ in } pu$$

$$F_l \quad = \quad \text{Non-directional line limit of } l \in \mathcal{L}, \text{ in MW}$$

$$\mathcal{W} \quad = \quad \{w = (u,v) \mid u,v \in \mathcal{S}, u \neq v\}, \text{ Set of non-directional transfers of interest of a stage of line limit calculation}$$

$$\phi_l^w \quad = \quad \text{Lossless decoupled power transfer distribution factor for line } l \in \mathcal{L}, \text{ given transfer } w \in \mathcal{W}, 0 < \phi_l^w \leq 1$$

$$P^w \quad = \quad \min_{l\in\mathcal{L}}\left\{\frac{F_l}{\phi_l^w}\right\}, \text{ Non-directional total transfer capability between buses in transfer } w \in \mathcal{W}, \text{ given only the line limits of } l \in \mathcal{L}, \text{ in MW}$$

$$\widetilde{\mathcal{N}} = \text{Set of lines in the post-elimination network of a stage of line limit calculation}$$

$$\widetilde{\mathcal{L}} = \{l = (u,v) \mid u, v \in \mathcal{S}, u \neq v, l \in \{\widetilde{\mathcal{N}} \setminus \mathcal{H}\}\}$$

$$\widetilde{y_l} = \text{Admittance of } l \in \widetilde{\mathcal{L}}, \text{ in } pu$$

$$\widetilde{F_l} = \text{Non-directional line limit of } l \in \widetilde{\mathcal{L}}, \text{ in MW}$$

$$\widetilde{\phi}_l^w = \text{Lossless decoupled power transfer distribution factor for line } l \in \widetilde{\mathcal{L}}, \text{ given transfer } w \in \mathcal{W}, 0 < \widetilde{\phi}_l^w \leq 1$$

$$\widetilde{P}^w = \min_{l \in \widetilde{\mathcal{L}}} \left\{ \frac{\widetilde{F_l}}{\widetilde{\phi}_l^w} \right\}, \text{ Non-directional total transfer capability between buses in transfer } w \in \mathcal{W}, \text{ given only the line limits of } l \in \widetilde{\mathcal{L}}, \text{ in MW}$$

$$\widetilde{\mathcal{F}} = \{\widetilde{F_l} \mid l \in \widetilde{L}\}, \text{ Set of line limits in the post-elimination network of a stage of line limit calculation}$$

$$m^w = \frac{\widetilde{P}^w - P^w}{P^w}, \text{ Normalized total transfer capability mismatch for transfer } w \in \mathcal{W} \text{ of a stage of line limit calculation}$$

$$\mathcal{M} = \{m^w \mid w \in \mathcal{W}\}, \text{ Set of normalized total transfer capability mismatches of a stage of line limit calculation}$$

$$\underline{\Psi} = [\psi_l^w] = \left[\widetilde{\phi}_l^w P^w \right], \text{ for row and column corresponding to } w \in \mathcal{W} \text{ and } l \in \widetilde{\mathcal{L}} \text{ respectively}$$

Note:

1. During a stage of line limit calculation, if $|\mathcal{S}| = \sigma$, and if no equivalent lines are ignored, then in general, $\left| \widetilde{\mathcal{L}} \right| = |\mathcal{W}| = {}^{\sigma}C_2 = \frac{1}{2}(\sigma^2 - \sigma)$.

2. In the set notations of $\mathcal{H}, \mathcal{L}, \mathcal{W}, \widetilde{\mathcal{L}}$ the 2-tuple (u,v) is non-directional, i.e., $(u,v) = (v,u)$.

3. All variables, except Π, $\mathcal{A}$ and $\mathcal{E}_k$, have a dependency on the stage of line limit calculation. This could be denoted by an additional super/subscript; however, since the goal is to elaborate on one general stage of line limit calculation, the super/sub-script has been dropped.

2.1 Steady State Equivalent Modeling

The idea of developing equivalents of larger power system models is not new. Initially, equivalent models were built to analyze power system interconnec-

tions, which were computationally too big to be handled by computers of their time. In addition, not every power system component needed to be distinctly represented in models of bulk transmission grids; this aggregation process also enhanced the techniques to build an equivalent. The two names that come to mind are Kron [3] and Ward [4], who developed the fundamental methods for building equivalents. Since then, several others have modified and enhanced their techniques based on engineering insights and heuristics. Even though computers now are more capable of handling large power system cases for off-line analyses, equivalent cases are still useful as they can provide good intuition and aid in faster calculations. An example is a 36-bus equivalent of the Northeast Power Coordinating Council area [9]. Although the attribute preservation type of work being presented in this chapter is targeted towards building larger equivalents, the work in [9] corroborates the use of equivalents in long-term economic studies. Preserving attributes will also improve the reliability of equivalent models, and possibly aid in closer to real-time applications.

2.1.1 Limit preserving power system equivalent

In an original power system model, line admittances and line thermal limits are usually known because they correspond to physical lines. While building an equivalent, buses in a power system are classified into study and external areas, after which the buses in external areas are eliminated. A method like Kron reduction [3] can be used to determine the connectivity and line admittances of the post-elimination unloaded network. However, this network will contain equivalent lines, which are fictitious and their limits are not known. Therefore, the notion of transmission limits could be significantly lost in an equivalent, which would diminish the usefulness of an equivalent during different loading conditions. This has motivated the idea of creating limit preserving power system equivalents, so that an equivalent can be used to study a variety of operating conditions, instead of just one.

The basics of assigning equivalent line limits have been presented in [10]. They involve sequential single bus eliminations, and are based on power transfer distribution factors (PTDFs) [11, 12]. Equivalent line limits are found by matching total transfer capabilities (TTCs) between the pre- and

post-elimination unloaded networks. However, an exact solution may not always exist. In previous work [10], upper estimates were determined by using inequality constraints, and lower estimates were based on discrete minimization of a cost function. Although this was able to provide meaningful bounds on equivalent line limits in smaller networks, its discrete nature caused the lower estimate to undesirably decline towards zero when eliminating a sequence of several buses from a large interconnection network. To design an algorithm tailored for interconnections, these basics are revisited, and improved upon in Sections 2.3 and 2.4.

In the broader scheme of developing equivalents to represent power system interconnections, it is not sufficient to just assign line limits to equivalent lines. Apart from the clever selection of study/external areas, there also needs to be a method for assigning equivalent bus-injections by "redistributing" loads and generators from the external areas to the study areas. There is literature in which such techniques are developed; these need to be enhanced to support building limit preserving equivalents (LPEs). Ward equivalents [4] are very often used, which are based on Kron reduction [3] for calculating equivalent line parameters, and also are capable of reallocating power injections from external areas to boundary buses. Although an approximation, the basic Ward injection method is able to produce a power system equivalent. Several modified Ward schemes have been developed since the original method in 1949. Other than their subtle differences, the generators from the external areas usually get split up because their power injections are reassigned to different boundary buses. Recently developed, the modified Ward equivalent with an inverse power flow scheme can overcome the aforementioned limitation [13]. This method is suitable for generation planning, which might require the retention of external generators as individual units. Another technique is the Radial, Equivalent and Independent (REI) method [14], which considers a group of adjacent buses to be eliminated, chooses one of them as a REI bus, moves all generation and load from all the buses in this group to the REI bus, retains the REI bus, and eliminates the other buses in the group with Kron reduction. Both the modified Ward and REI methods are useful for assigning equivalent bus-injections. Such methods have been applied to develop interconnection equivalents to aid in tasks like generation planning [15].

The basic Ward, modified Ward and REI techniques all rely on a solved

power flow. This implies that the derived equivalent is based on a specific operating point. To make an equivalent, which is useful for an approximate loading condition (i.e. a set of operating points), heuristics need to be used, which can be application specific. Also, available transfer capability (ATC) [16] can have both directional and operating-point dependency [10]. Embedding the operating point in an equivalent is not desirable as it will restrict its use in simulating other operating points. Moreover, applications such as optimal and security-constrained optimal power flow (OPF and SCOPF) conventionally require non-directional line limits [17]. Keeping these in mind, it is envisioned that an LPE will be built through an LPE algorithm, which would first require determining the buses to be eliminated. Once the study/external areas are determined, this LPE algorithm would find equivalent line limits of an unloaded network, then find the equivalent bus-injections, and finally reload the equivalent network, resulting in an LPE.

2.1.2 Line limit calculation for equivalent networks

The methods to build equivalents, described earlier, are able to calculate the electrical parameters of equivalent lines, but are unable to assign line limits to them. In most commercial software packages, a default limit value of "zero" is displayed for equivalent lines. This is interpreted by the software as an infinite capacity for that equivalent line. Intuition tells us that it is impossible for an equivalent line to have an infinite capacity, especially if it originated from a sub-network with a finite transmission capacity. Hence, the goal is to assign meaningful bounds that are less than infinity. Section 2.2 will discuss the preliminary work from [10]. Next, the development of a quadratic program formulation is outlined in Section 2.3, first with a 4-bus example, and then applied to the IEEE 118-bus test system. Section 2.4 discusses results, further improvements to the general algorithm, computational aspects, and the use of heuristics to further enhance calculations. Lastly, conclusions and future work are summarized.

2.2 Assignment of Limits to Equivalent Lines

In this section, an improved method for calculating line limits for equivalent networks is presented. This technique also involves sequential single bus eliminations in an order dictated by Tinney scheme 2 [18], and is based on PTDFs [11, 12]. However, unlike the work in [10], the objective of this limit preserving network – quadratic program (LPN-QP) formulation – is to minimize the sum of the square of the mismatch in normalized TTCs of all transfers of interest between the pre- and post-elimination unloaded networks. TTC is used, instead of ATC, to prevent operating point dependency. The necessity and the development of the LPN-QP formulation is illustrated with the elimination of one bus from a 4-bus network, after which the formulation is generalized and applied towards the elimination of 56 buses from the IEEE 118-bus test network.

2.2.1 Elimination of one bus from a 4-bus network

In this example, Bus 1 is eliminated from a 4-bus network (Figure 2.1a) to create a 3-bus network (Figure 2.1b). The parameters of these two networks are summarized in Table 2.1. Kron reduction is used to compute the admittance of equivalent lines $(2, 3)$, $(2, 4)$ and $(3, 4)$, and their limits are to be calculated. To reiterate, only an unloaded system is being considered to ensure no operating point dependency. By reducing the limit value of line $(1, 4)$ from 60 to 20 MW, it is observed that the solution changes from being
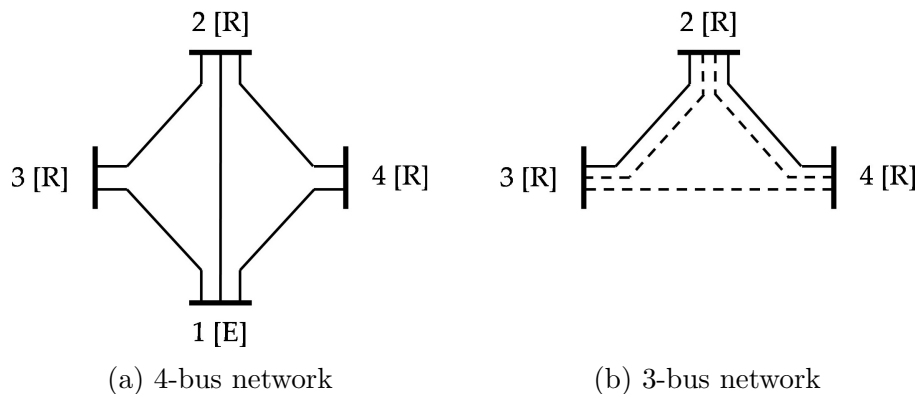

(a) 4-bus network   (b) 3-bus network

Figure 2.1: Elimination of bus 1 from a 4-bus unloaded network. (Labels – [R]: Retained, and [E]: Eliminated.)

exact to non-exact. This example is used to outline the proposed solution method and the LPN-QP formulation.

In the first step, three sets are identified:

(i) set of lines that become eliminated, $\mathcal{L} = \{(1,2),(1,3),(1,4)\}$,

(ii) set of equivalent lines created, $\widetilde{\mathcal{L}} = \{(2,3),(2,4),(3,4)\}$, and

(iii) set of transfers of interest, $\mathcal{W} = \{(2,3),(2,4),(3,4)\}$.

Next, the PTDFs, ϕ_l^w for $l \in \mathcal{L}$ are calculated, and then together with line limits, F_l for $l \in \mathcal{L}$, the TTCs, P^w for $w \in \mathcal{W}$ are calculated in (2.1). While calculating TTCs, only the limits of lines in $\mathcal{L}$ are considered, because it is the goal of every stage of elimination to match the transmission limits of the equivalent lines with those that become eliminated. Moreover, lines $(2,3)$ and $(2,4)$ will continue to exist and assert their limits in the equivalent network. Following from this argument, the set of transfers of interest are between those pairs of buses that the equivalent lines are incident on, i.e., $\mathcal{W}$.

$$
\begin{aligned}
P^{(2,3)} &= \min \left\{ \frac{F_{(1,2)}}{\phi_{(2,3)}^{(2,3)}}, \frac{F_{(1,3)}}{\phi_{(2,4)}^{(2,3)}}, \frac{F_{(1,4)}}{\phi_{(3,4)}^{(2,3)}} \right\}, \\
P^{(2,4)} &= \min \left\{ \frac{F_{(1,2)}}{\phi_{(2,3)}^{(2,4)}}, \frac{F_{(1,3)}}{\phi_{(2,4)}^{(2,4)}}, \frac{F_{(1,4)}}{\phi_{(3,4)}^{(2,4)}} \right\}, \\
P^{(3,4)} &= \min \left\{ \frac{F_{(1,2)}}{\phi_{(2,3)}^{(3,4)}}, \frac{F_{(1,3)}}{\phi_{(2,4)}^{(3,4)}}, \frac{F_{(1,4)}}{\phi_{(3,4)}^{(3,4)}} \right\}.
\end{aligned}
\tag{2.1}
$$

Table 2.1: Parameters for 4-bus and 3-bus networks.

	4-bus network			3-bus network	
Line	Admittance (p.u.)	Line limit (MW)	Line	Admittance (p.u.)	Line limit (MW)
$(1,2)$	$-\jmath 16.67$	100	$(2,3)_{eq}$	$-\jmath 4.32$	?
$(1,3)$	$-\jmath 8.33$	70	$(2,4)_{eq}$	$-\jmath 3.70$	?
$(1,4)$	$-\jmath 7.14$	**60 ↘ 20**	$(3,4)_{eq}$	$-\jmath 1.85$	?
$(2,3)$	$-\jmath 12.50$	90	$(2,3)$	$-\jmath 12.50$	90
$(2,4)$	$-\jmath 10.00$	80	$(2,4)$	$-\jmath 10.00$	80

Note: As the limit of line $(1,4)$ is reduced from 60 to 20 MW, the solution changes from being exact to non-exact

$$\min \left\{ \frac{\widetilde{F}_{(2,3)}}{\widetilde{\phi}^{(2,3)}_{(2,3)}}, \frac{\widetilde{F}_{(2,4)}}{\widetilde{\phi}^{(2,3)}_{(2,4)}}, \frac{\widetilde{F}_{(3,4)}}{\widetilde{\phi}^{(2,3)}_{(3,4)}} \right\} = P^{(2,3)},$$

$$\min \left\{ \frac{\widetilde{F}_{(2,3)}}{\widetilde{\phi}^{(2,4)}_{(2,3)}}, \frac{\widetilde{F}_{(2,4)}}{\widetilde{\phi}^{(2,4)}_{(2,4)}}, \frac{\widetilde{F}_{(3,4)}}{\widetilde{\phi}^{(2,4)}_{(3,4)}} \right\} = P^{(2,4)}, \qquad (2.2)$$

$$\min \left\{ \frac{\widetilde{F}_{(2,3)}}{\widetilde{\phi}^{(3,4)}_{(2,3)}}, \frac{\widetilde{F}_{(2,4)}}{\widetilde{\phi}^{(3,4)}_{(2,4)}}, \frac{\widetilde{F}_{(3,4)}}{\widetilde{\phi}^{(3,4)}_{(3,4)}} \right\} = P^{(3,4)}.$$

Similarly with the post-elimination network, PTDFs, $\widetilde{\phi}^w_l$ for $l \in \widetilde{\mathcal{L}}$ are calculated, and together with equivalent line limits, $\widetilde{F}_l$ for $l \in \widetilde{\mathcal{L}}$, the expressions for post-elimination TTCs are equated to the TTC values from (2.1). The only unknowns in (2.2) are the $\widetilde{F}_l$ terms. A re-statement of (2.2) is $\widetilde{F}_l = \max \left\{ \widetilde{\phi}^w_l P^w = \psi^w_l \mid w \in \mathcal{W} \right\}$, for $l \in \widetilde{\mathcal{L}}$, along with the caveat that every equivalent line limit is a result of a different binding transaction. This caveat is important because it ensures that (2.2) continues to be satisfied. When $F_{(1,4)} = 60$ MW, (2.3) shows the calculated values for $\underline{\Psi}$.

Criteria for an exact solution: If the max. value in each column of $\underline{\Psi}$ (for each equivalent line) also belongs to different rows of $\underline{\Psi}$ (for each transfer), then the equivalent line limits are the max. value in each column of $\underline{\Psi}$.

Hence, an exact solution exists for this case, and $\widetilde{F}_{(2,3)_{eq}} = 50.8$ MW, $\widetilde{F}_{(2,4)_{eq}} = 41.4$ MW and $\widetilde{F}_{(3,4)_{eq}} = 28.5$ MW.

$$\underline{\Psi}|_{[F_{(1,4)}=60 \text{ MW}]} = \begin{bmatrix} \mathbf{50.8} & 5.2 & 19.2 \\ 4.8 & \mathbf{41.4} & 18.6 \\ 29.9 & 31.5 & \mathbf{28.5} \end{bmatrix}. \qquad (2.3)$$

However, because equivalent line limits do not "redistribute" themselves in the same way as equivalent line admittances, an exact solution does not always exist.

2.3 Quadratic Optimization Method

For that case, (2.2) is normalized with their respective P^w values, and a mismatch variable, m^w, is introduced. This allows each of the equality constraints to be relaxed, and creates an artificial feasible region for finding a

non-exact solution for equivalent line limits. This does not imply that an exact solution could be somehow uncovered. If a stage of elimination fails the *criteria for an exact solution*, it is impossible to find a point in this artificial feasible region which corresponds to all mismatches being zero. The next best alternative is to express this as a quadratic program (QP) in (2.4), which minimizes the sum of the square of the mismatches. This QP in (2.4) is referred to as the strong formulation.

$$\underset{\substack{\widetilde{F}_{(2,3)},\widetilde{F}_{(2,4)},\widetilde{F}_{(3,4)}, \\ m^{(2,3)},m^{(2,4)},m^{(3,4)}}}{\text{minimize}} \quad \left(m^{(2,3)}\right)^2 + \left(m^{(2,4)}\right)^2 + \left(m^{(3,4)}\right)^2,$$

$$\text{s.t.} \quad m^{(2,3)} = \min\left\{\frac{\widetilde{F}_{(2,3)}}{\psi_{(2,3)}^{(2,3)}}, \frac{\widetilde{F}_{(2,4)}}{\psi_{(2,4)}^{(2,3)}}, \frac{\widetilde{F}_{(3,4)}}{\psi_{(3,4)}^{(2,3)}}\right\} - 1,$$

$$m^{(2,4)} = \min\left\{\frac{\widetilde{F}_{(2,3)}}{\psi_{(2,3)}^{(2,4)}}, \frac{\widetilde{F}_{(2,4)}}{\psi_{(2,4)}^{(2,4)}}, \frac{\widetilde{F}_{(3,4)}}{\psi_{(3,4)}^{(2,4)}}\right\} - 1, \qquad (2.4)$$

$$m^{(3,4)} = \min\left\{\frac{\widetilde{F}_{(2,3)}}{\psi_{(2,3)}^{(3,4)}}, \frac{\widetilde{F}_{(2,4)}}{\psi_{(2,4)}^{(3,4)}}, \frac{\widetilde{F}_{(3,4)}}{\psi_{(3,4)}^{(3,4)}}\right\} - 1,$$

$$\widetilde{F}_{(2,3)} \geq 0, \quad \widetilde{F}_{(2,4)} \geq 0, \quad \widetilde{F}_{(3,4)} \geq 0.$$

Finding a solution for the strong formulation yields values for $\widetilde{F}_l$ for $l \in \widetilde{\mathcal{L}}$ which are able to preserve the TTC as "best" as possible – this can be considered as a best-fit estimate. Sometimes it can be of interest to obtain lower and upper bounds for these limits, and so inequality conditions from (2.5) or (2.6) can be supplemented with (2.4), to provide a lower estimate or an upper estimate respectively.

$$m^{(2,3)} \leq 0, \quad m^{(2,4)} \leq 0, \quad m^{(3,4)} \leq 0. \qquad (2.5)$$

$$m^{(2,3)} \geq 0, \quad m^{(2,4)} \geq 0, \quad m^{(3,4)} \geq 0. \qquad (2.6)$$

These additional inequality conditions ensure that the solution strictly allows a negative or positive TTC mismatch, hence respectively corresponding to a lower estimate or an upper estimate. It is possible that best estimate might be equal to either the lower or the upper estimate in some cases. If all three estimates are equal, then this is the same as an exact solution as shown in (2.2), hence allowing this QP to converge on the same answer that

could be detected by the *criteria for an exact solution*.

The strong formulation is both non-linear and non-convex. To be able to solve the LPN-QP formulation, the three equality constraints from (2.4) are transformed into nine weaker inequality constraints of the form as shown in (2.7).

$$\widetilde{F_l} \geq \psi_l^w \left(m^w + 1 \right), \quad w \in \mathcal{W}, l \in \widetilde{\mathcal{L}}. \tag{2.7}$$

These are then combined per equivalent line to form three equality constraints of the form shown in (2.8). This equation signifies that, with some mismatch, each equivalent line limit value will be determined as a consequence of at least one of the transfers in $\mathcal{W}$ being limited.

$$\widetilde{F_l} = \max \left\{ \psi_l^w \left(m^w + 1 \right) \mid w \in \mathcal{W} \right\}, \quad l \in \widetilde{\mathcal{L}}. \tag{2.8}$$

Since each equivalent line has to limit at least one of three transfers, one of the inequality constraints (for each line) is picked as an equality constraint. The resulting expression is substituted to yield six inequality constraints (of the form as shown in (2.9), allowing the LPN-QP formulation to be specified only in terms of m^w. This reduction from six to three decision variables is desirable because it transforms the problem such that the objective function has a positive definite coefficient matrix.

$$\psi_l^{i_l} \left(m^{i_l} + 1 \right) \geq \psi_l^{j_l} \left(m^{j_l} + 1 \right), \quad j_l \in \{\mathcal{W} \setminus \{i_l\}\}, l \in \widetilde{\mathcal{L}}. \tag{2.9}$$

Using the inequality conditions in (2.9), $3^3 = 27$ QPs are formulated and solved. Depending on the equality conditions assumed for each $\widetilde{F_l}$, in each of the 27 cases, the value of $\widetilde{F_l}$ is calculated. Since (2.9) is a weaker formulation of the equality constraints in (2.4), there is a possibility that one of these 27 weaker QPs could be infeasible, or yield an answer that violates the equality conditions from the strong formulation in (2.4). Those cases are detected, and discarded. Then, the sum of square of mismatches is ranked, and the line limits from the QP with the smallest objective are chosen as the solution.

Given $F_{(1,4)} = 20$ MW, the *criteria for an exact solution* are not satisfied. Therefore, LPN-QP is used to obtain a non-exact solution, which is shown in Table 2.2. For comparison, the non-exact solution from LPN – Max. value/Hungarian (LPN-MH) (an older formulation developed in [10] is also

shown. The first improvement is the ability to find non-exact solutions from a range of feasible values rather than the just discrete values in $\underline{\Psi}$. In this example there was no difference observed in the upper estimate, but the values for the lower estimate are different. Two important conclusions can be made from the comparison of the lower estimates - (i) LPN-QP is able to find a better solution of line limits than LPN-MH, which reduces the TTC mismatch, and (ii) LPN-QP always assigns the best value of line limits required to have the minimum TTC mismatch, which ensures that every equivalent line captures one or more of the limits of the lines that become eliminated, other than the mismatch.

The limits from LPN-QP are collectively somewhat larger than the values from LPN-MH, which is more valuable – getting smaller than necessary lower estimates could lead to them converging towards zero through successive bus eliminations, which would still be a lower estimate but would be practically meaningless. The best estimate is a product of LPN-QP, which previously could not be obtained from LPN-MH. This is essentially the best-fit solution, where the sum of square of mismatches is 0.0363, as compared to 0.0576 and 0.0993 corresponding to the lower and upper estimates respectively. In short, the best estimate is suitable for use in approximate analyses, while the lower

Table 2.2: Equivalent line limits of the 3-bus system: LPN-MH vs. LPN-QP.

	Line or Transfer	Max. value/Hungarian		Quadratic program	
		Line limit (MW)	Normalized TTC mismatch (%)	Line limit (MW)	Normalized TTC mismatch (%)
Upper estimate	$(2,3)$	50.8	0.0	50.8	0.0
	$(2,4)$	13.8	0.0	13.8	0.0
	$(3,4)$	19.2	31.5	19.2	31.5
Best estimate	$(2,3)$	N/A	N/A	**50.8**	**0.0**
	$(2,4)$	N/A	N/A	**11.7**	**−15.2**
	$(3,4)$	N/A	N/A	**19.2**	**11.5**
Lower estimate	$(2,3)$	50.8	**−50.4**	50.8	**0.0**
	$(2,4)$	**13.8**	**0.0**	10.5	**−24.0**
	$(3,4)$	**9.5**	0.0	**19.2**	0.0

and upper estimates are suitable for conservative and optimistic analyses, respectively.

2.3.1 Generalizing LPN-QP

The LPN-QP formulation can be solved repeatedly for every stage of single bus elimination that does not have an exact solution. Lossless decoupled PTDF is used as an approximation for how power transfers distribute themselves over various lines, and a further assumption has been made that the transfers between first neighbor buses sufficiently capture the line loading effects due to other transfers that occur over a wider area. Also, only the limits of the lines getting eliminated in a step need to be considered to calculate pre-elimination TTCs. This, coupled together with considering only the transfers in $\mathcal{W}$, is being leveraged for the LPN-QP formulation. The outcome is a formulation of the general LPN-QP as shown in (2.10), termed as the strong formulation.

$$
\begin{aligned}
\underset{\widetilde{F}_l \in \widetilde{\mathcal{F}}, m^w \in \mathcal{M}}{\text{minimize}} \quad & M = \sum_{m^w \in \mathcal{M}} (m^w)^2, \\
\text{s.t.} \quad & m^w = \min_{l \in \widetilde{\mathcal{L}}} \left\{ \frac{\widetilde{F}_l}{\psi_l^w} \right\} - 1, \quad w \in \mathcal{W}, \\
& \widetilde{F}_l \geq 0, \qquad\qquad\qquad l \in \widetilde{\mathcal{L}}.
\end{aligned} \tag{2.10}
$$

This is then transformed into a weaker formulation in (2.11), which is more convenient to solve.

$$
\begin{aligned}
\underset{\widetilde{F}_l \in \widetilde{\mathcal{F}}, m^w \in \mathcal{M}}{\text{minimize}} \quad & M = \sum_{m^w \in \mathcal{M}} (m^w)^2, \\
\text{s.t.} \quad & \psi_l^{i_l} \left(m^{i_l} + 1 \right) \\
& - \psi_l^{j_l} \left(m^{j_l} + 1 \right) \geq 0, \quad j_l \in \{\mathcal{W} \setminus \{i_l\}\}, l \in \widetilde{\mathcal{L}}, \\
& m^w + 1 \geq 0, \quad w \in \mathcal{W}.
\end{aligned} \tag{2.11}
$$

where this is the form of one QP, which belongs to a set of all possible combinations of $\{i_l \mid l \in \widetilde{\mathcal{L}}\}$, i.e., $|\mathcal{W}|^{|\widetilde{\mathcal{L}}|}$ combinations. Solving these will give the best estimate. Inequality conditions from (2.12) or (2.13) can also be supplemented with (2.11), to calculate a lower or an upper estimate, respectively.

$$m^w \leq 0. \tag{2.12}$$

$$m^w \geq 0. \tag{2.13}$$

To solve, an interior point quadratic program solver from Matlab is used. The closely related problems are solved efficiently: if the best estimate formulation indicates that certain combinations are only feasible when $m^w = -1$ (i.e., $\widetilde{F}_l = 0$), then those combinations are discarded while solving the lower and upper estimates.

Every stage of elimination can potentially yield lower, best and upper estimates. If an exact solution exists, then all three estimates will be assigned same value. From the perspective of developing code, the calculations for upper and lower estimates can proceed independently of one another during each step of elimination. Also, these estimates are not mixed-and-matched with each other. For example, only lower estimates from the previous stage will be used to calculate the lower estimates for the next stage, and so on. This allows each estimate to capture inaccuracies within itself, and not propagate to the other estimates. The sequential bus elimination algorithm, with both LPN-MH and LPN-QP formulations, has been implemented.

2.3.2 Elimination of 56 buses from IEEE 118-bus test network

A 62-bus equivalent network, with equivalent line limits, is created from the IEEE 118-bus test network. The buses to be eliminated are randomly selected. Information about generators and loads from the IEEE 118-bus test system is ignored. Only an unloaded network is utilized to create a limit preserving network, which will be independent of operating point. The 56 buses to be eliminated are divided into sub-groups in such a way that each sub-group consists of maximal adjacent buses. In other words, if two buses being eliminated are adjacent or can be connected via a continuous path of other buses that are also being eliminated, they are assigned to the same sub-group. These 56 buses are partitioned into 31 mutually independent sub-groups.
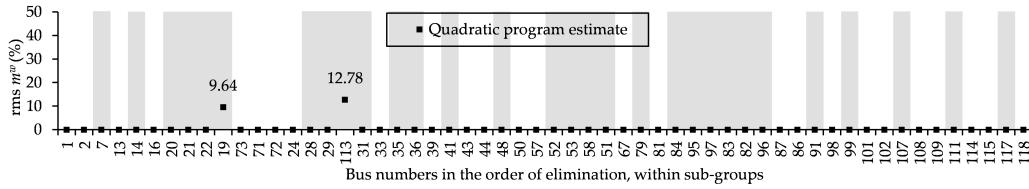
Sub-groups are of interest because the elimination of a bus from one sub-group has no effect on the elimination of a bus from another sub-group. How-
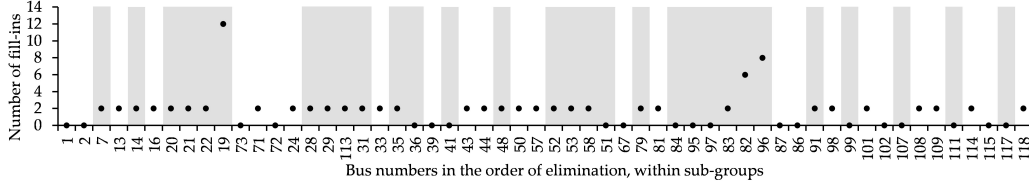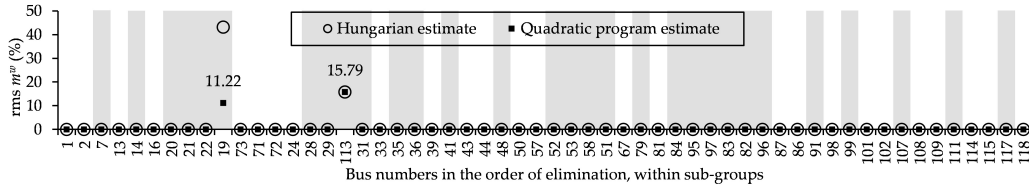
(a) Number of fill-ins each bus-elimination creates.
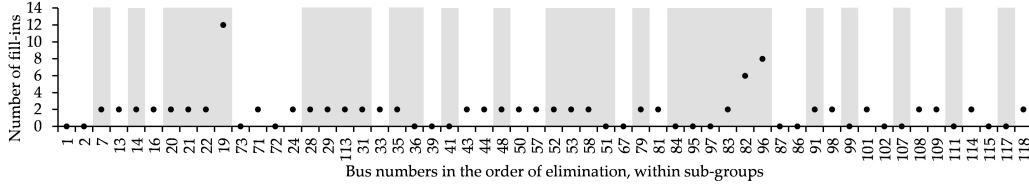
(b) Root mean square value of normalized TTC mismatch while calculating line limit upper estimate for each bus-elimination.

(c) Root mean square value of normalized TTC mismatch while calculating line limit best estimate for each bus-elimination.

(d) Root mean square value of normalized TTC mismatch while calculating line limit lower estimate for each bus-elimination.

Figure 2.2: Elimination of 56 buses (grouped into 31 non-overlapping sets, and displayed above in alternating bands of white and gray) from the IEEE 118-bus test network.

ever, within each sub-group, two buses might share a line and this creates a dependency on the elimination order. As these 31 sub-groups are independent, the same results are obtained if all 56 buses are sequentially eliminated, or eliminated through 31 parallel paths, each with sequential eliminations. They are essentially the same order of elimination, based on Tinney scheme 2. Figure 2.2a shows the number of fill-ins created in the $\underline{Y}_{\text{bus}}$ during single bus eliminations within each sub-group. The alternating bands of white and gray indicate the 31 sub-groups. Due to the Tinney scheme 2 elimination order, the number of fill-ins increases with the stage of elimination within

22

each sub-group.

During each stage of single bus elimination, the rms of normalized TTC mismatch, rms $m^w = \sqrt{M/|\mathcal{W}|}$, is recorded. A value of > 0 % indicates a non-exact solution; Figures 2.2b, 2.2c and 2.2d show the rms m^w values of all 56 single bus eliminations, and from both LPN-MH and LPN-QP solutions. In these three figures, the numerical labels within sub-groups $\mathcal{E}_6 = \{20, 21, 22, 19\}$ and $\mathcal{E}_8 = \{28, 29, 113, 31\}$ correspond to the rms m^w value from LPN-QP. These values indicate that LPN-QP is able to perform on-par with or better than LPN-MH for every single bus elimination.

It is interesting to observe that some sub-groups yield exact solutions for all eliminations within their group. This is an ideal scenario where the *criteria for an exact solution* are met, and there is no need for more computation to find non-exact solutions. When there is no exact solution for a single bus elimination within a sub-group, then all consecutive eliminations will yield lower, best and upper estimates. For example, within sub-group $\mathcal{E}_8$, elimination of bus 113 yields a lower, best and upper estimate. Thereafter, elimination of bus 31 yields an exact solution for each of these lower, best and upper estimates. This does not imply that the lines after the elimination of bus 31 have unique line limits; they continue to have lower, best and upper estimates. Only when all single bus eliminations within a sub-group have exact solutions, do all equivalent lines resulting from the elimination of that sub-group have unique line limits.

2.4   Discussion and Improvements

As described in Section 2.3.2, the elimination of buses from one sub-group has no effect on that of another sub-group. Considering one such sub-group, there still remains an elimination order dependency, unless all single bus eliminations yield exact solutions. For a single bus elimination, numerical experiments have shown that disproportionate line limits, or a significantly different ratio of F_l:y_l, for $l \in \mathcal{L}$, causes non-exact solution because the line limits are unable to redistribute themselves in an "exact manner." This is the reason for elimination order dependency. To analyze the extent of this dependency, sub-group $\mathcal{E}_8$ is used. As shown in Figure 2.3, the black arrows show the sequence of single bus eliminations. During sequential elimination,

with both LPN-MH and LPN-QP formulations, some form error is being minimized in each single bus elimination. However, it is of greater interest to minimize any discrepancy in TTCs between the pre- and post-elimination networks of the overall elimination of $\mathcal{E}_8$. Even though the elimination of bus 113 resulted in an rms mismatch of only 12.78 % for the best estimate (Figure 2.2c), the accumulation of errors through four single bus eliminations resulted in an overall rms mismatch of 18.2 % (Table 2.3). Comparing the overall rms mismatches from sequential eliminations from LPN-QP (7.6 %) seems to perform on par with LPN-MH (7.6 %) (Table 2.3). A possible reason for this could be because LPN-QP is locally optimal for each single bus elimination, and that causes more error build-up. Nevertheless, sequential single bus eliminations seem to accumulate relatively higher amounts of rms mismatch, which is undesirable.

2.4.1 Sub-group elimination

Instead of sequential single bus eliminations, sub-group elimination is introduced to circumvent elimination order dependency. As mentioned in Section 2.3.2, if two buses being eliminated are adjacent or can be connected via a continuous path of other buses that are also being eliminated, they are assigned to the same sub-group. With reference to the illustration of sub-group elimination in Figure 2.3, Kron reduction still occurs in stages shown by the sequence of black arrows, but the calculation of equivalent line limits is performed as a direct calculation shown by the grey arrow. This saves on computations within intermediate networks, which were previously needed to calculate PTDFs and solve LPN-QP formulations. Moreover, equivalent lines in intermediate networks eventually do not exist in the final post elimination network, for example equivalent lines $(17, 31)$, $(31, 32)$ and $(27, 31)$. All that matters is the calculation of equivalent line limits after the elimination of an entire sub-group. This insight is particularly useful when intermediate networks have significantly more equivalent lines than the network after the elimination of a sub-group.

Direct calculation is now used for eliminating sub-group $\mathcal{E}_8$. As seen in Table 2.3, the rms mismatches from a direct calculation are lower than those from a sequential calculation for both LPN-MH and LPN-QP formulations.
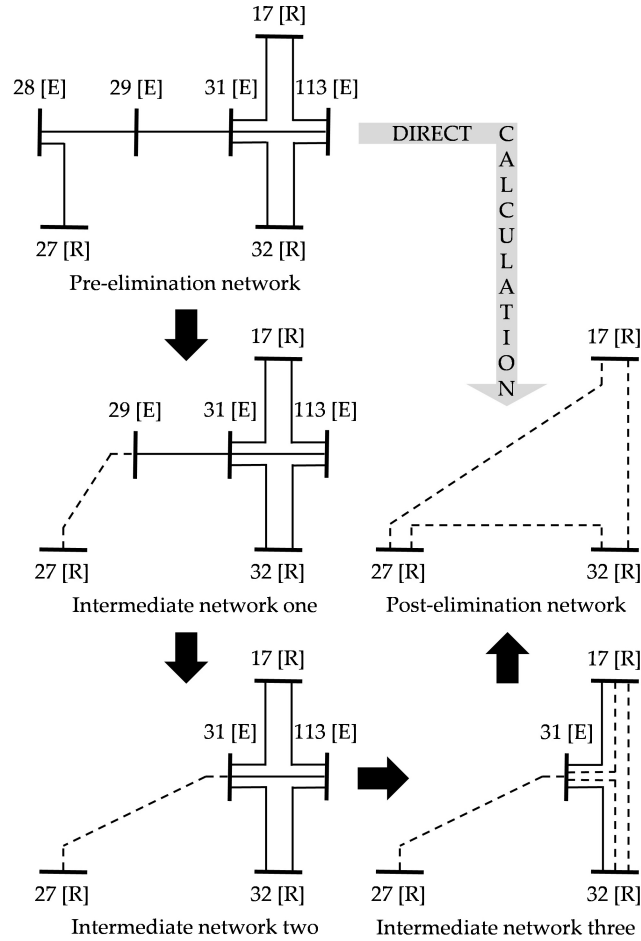
Figure 2.3: Elimination of buses 28, 29, 113 and 31 from a sub-network of the IEEE 188-bus test network.
(Black arrow shows sequence of single-node eliminations, and grey arrow shows direct calculation. Labels – [R]: Retained, and [E]: Eliminated.)

The best estimate's rms mismatch of 18.2 % is reduced to 3.7 %. This also yields a case where the rms mismatch values for the lower estimate is the same from both LPN-MH and LPN-QP (5.0 %). However, the corresponding limit of equivalent line $(27, 32)$ is 53.2 MW in the former and 48.6 MW in the latter formulation. This implies that the other two lines are sufficient in enforcing all three TTCs as long as the limit of equivalent line $(27, 32)$ is ≥ 48.6 MW. From an unloaded network perspective there is no difference in between the both answers, but once the network is reloaded, this will result in different ATC values.

For the IEEE 118-bus network, it takes about 323 seconds to solve for each (best, lower and upper) estimate of equivalent line limits after elimi-

Table 2.3: Rms mismatch: direct vs. sequential method.

| | | Max. value/Hungarian | | Quadratic program | |
| | | Seqn. | Direct | Seqn. | Direct |
	Transfer	Line limit (MW)	Line limit (MW)	Line limit (MW)	Line limit (MW)
Upper estimate	$(17, 27)$	63.5	44.7	63.5	44.7
	$(17, 32)$	170.8	121.8	170.8	121.8
	$(27, 32)$	54.6	53.2	54.6	53.2
	rms norm. TTC mismatch	*39.4 %*	*5.5 %*	*39.4 %*	*5.5 %*
Best estimate	$(17, 27)$	N/A	N/A	56.7	42.6
	$(17, 32)$	N/A	N/A	140.5	121.8
	$(27, 32)$	N/A	N/A	54.6	50.7
	rms norm. TTC mismatch	*N/A*	*N/A*	*18.2 %*	*3.7 %*
Lower estimate	$(17, 27)$	56.7	40.8	56.7	40.8
	$(17, 32)$	124.3	121.8	124.3	121.8
	$(27, 32)$	54.6	53.2	54.6	48.6
	rms norm. TTC mismatch	*7.6 %*	*5.0 %*	*7.6 %*	*5.0 %*

nating 56 buses. To build a limit preserving network that is independent of operating point, the answer from LPN-QP is the most accurate and least dependent/biased towards any operating point. With this new technique, LPNgroup (summarized in Algorithm 1 supersedes sequential single bus elimination, and is preferred.

2.4.2 Computational aspects, heuristics and insights

Not only does the LPNgroup algorithm save computation time, but the worst-case complexity for the direct calculation after elimination of buses in $\mathcal{E}_k$ is the same as sequentially calculating limits for the final single bus elimination in set $\mathcal{E}_k$. This is because $\mathcal{W}$ and $\widetilde{\mathcal{L}}$ are the same regardless of $\mathcal{C} = \mathcal{E}_k$ or $\mathcal{C} = \{$last bus to be eliminated from $\mathcal{E}_k\}$, for direct and sequential calculations respectively. It is scalable for large-scale systems because

Algorithm 1 LPNgroup algorithm for limit preserving network calculation concurrent sub-group eliminations.

Data: Π, $\mathcal{A}$

Result: Π_{final}

1: partition $\mathcal{A}$ into $\mathcal{E}_1, \ldots, \mathcal{E}_K$
2: initialize $\mathcal{N} \leftarrow \mathcal{T}$
3: **for** $k = 1 \ldots, K$ **do**
4:     $\mathcal{C} \leftarrow \mathcal{E}_k$
5:     reinitialize $\mathcal{S}$, $\mathcal{H}$, $\mathcal{L}$, $\mathcal{W}$
6:     recompute ϕ_l^w, P^w
7:     recompute $\widetilde{\mathcal{N}}$, $\widetilde{\mathcal{L}}$, $\widetilde{y}_l$ after elimination of buses in $\mathcal{C}$
8:     recompute $\widetilde{\phi}_l^w$, Ψ
9:     **if** *criteria for an exact solution is satisfied* **then**
10:       $\widetilde{F}_l = \max\{\psi_l^w \mid w \in \mathcal{W}\}$
11:     **else**
12:       reformulate problem with LPN-MH or LPN-QP
13:       solve LPN-MH or LPN-QP for $\widetilde{F}_l$
14:     **end if**
15:     $\mathcal{N} \leftarrow \widetilde{\mathcal{N}}$
16: **end for**
17: $\Pi_{\text{final}} \leftarrow \{\{\mathcal{B} \setminus \mathcal{A}\}, \widetilde{\mathcal{N}}, \{y_{l \in \widetilde{\mathcal{N}}}\}, \{F_{l \in \widetilde{\mathcal{N}}}\}\}$

---

each sub-group calculation is a small or medium-scale problem. In the LPN-QP formulation there is a concern about generating and solving $|\mathcal{W}|^{|\widetilde{\mathcal{L}}|}$ QPs, which can be a large number if external areas have many connections with the study areas. Research is in progress to better understand the structure of these QPs, which may lead to a better numerical solution method. Nonetheless, this is not a show-stopper because these are off-line calculations. Parallel processing can also be harnessed to solve these mutually independent QPs. Moreover, LPNgroup can be implemented to tackle each sub-group's $(\mathcal{E}_1, \ldots, \mathcal{E}_K)$ calculation in parallel. In short, highly parallel code can be implemented to run on dual/quad core CPUs, or even GPUs.

A bottle-neck is the possibility of having too many pre-elimination neighbor buses, i.e., $|\mathcal{S}| = \sigma$. A small change in σ from 3 to 4 causes a change in $|\mathcal{W}|$ or $|\widetilde{\mathcal{L}}|$ from $^3\mathrm{C}_2 = 3$ to $^4\mathrm{C}_2 = 6$, which increases the number of post-elimination PTDF calculations from $3^2 = 9$ to $6^2 = 36$, and finally the number of QPs generated increases from $3^3 = 27$ to $6^6 = 46656$. This might seem intimidating, but can be contained with the clever selections external areas. One heuristic could be selecting external sub-groups such that their

pre-elimination neighbor buses do not exceed 5. From a practical perspective, if there is a bus (or group of buses) which is connected to several other buses (for example > 5), then it might not be a good engineering decision to eliminate it. This rule might not be applicable in every context, but engineering insights will be valuable towards making a good selection of buses to eliminate. Ignoring equivalent lines with admittance magnitudes of $< 1.0\ pu$ could also be a useful heuristic. In this case, low admittance lines will simply be ignored from $\widetilde{\mathcal{L}}$. In some instances, if all equivalent lines incident at a particular bus can be ignored, then all transfers including that bus can also be ignored from $\mathcal{W}$. The formulations of LPN-MH and LPN-QP can be adjusted accordingly.

Seasonal variations in power flow patterns can diminish the usability of equivalent line limits for an interconnection equivalent. This is because power flow patterns in an equivalent heavily rely on the choice of buses that were eliminated (i.e., external area(s)), and on the method that was used to redistribute load and generation amongst the retained buses (i.e., study area(s)). As a heuristic, external area(s) should be determined in a manner that avoids eliminating transmission lines that participate in seasonal and relatively large import/export transactions. If this information is available (based on historical data or experience), it can be used to create an equivalent, resulting in equivalent line limits being more meaningful across different seasons. Otherwise, seasonal equivalents can be created, each of which may consist of slightly different study area(s). Nevertheless, it is to be noted that equivalent line limits, being calculated by the LPNgroup with the LPN-QP formulation, are operating point independent, because they are based on an unloaded network.

2.4.3 Key takeaways

LPNgroup with the LPN-QP formulation is being proposed as the preferred approach. No doubt that there may be significant mismatches in smaller-scale academic networks, but accuracy will be better for large-scale interconnection equivalents because power rarely flows from one extreme location to another. The methods developed in the above sections will provide a more meaningful alternative than assuming infinite equivalent line limits, which

is currently practiced in the industry. This will ensure that there is some preservation of transmission limits while developing equivalents. Like existing methods, there will continue to be a trade-off of accuracy. However, the goal is to utilize the LPNgroup-LPN-QP method in the broader framework, to develop an LPE that has equivalent line limits and is usable for a range of operating points that have similar power flow patterns. Work is in progress to interweave the LPNgroup-LPN-QP with REI and modified Ward methods, which will result in equivalents exhibiting lesser sensitivity to their original operating point and greater preservation of transmission limits. Ultimately, OPF, SCOPF, other planning analyses and newer real-time applications will benefit from the development of LPEs.

2.5 Future Work: Top-Down Simplified Method for Large-Scale Equivalents

Scalability of these type of algorithms is an important concern while assigning equivalent line limits. Even though such calculations would be done in an off-line manner, the computation time needs to be tractable while dealing with large-scale power system interconnections. In addition to this, the results obtained from these algorithms need to have some degree of agreement with the limits associated with the original system. Based on the analysis and studies presented in this chapter, equivalent line limits tend to be more meaningful when (i) the range between their upper and lower bounds is relatively small, and (ii) the lower bound is as large as possible.

As shown earlier in this chapter, the fundamental reason for not having exact solutions to equivalent line limits is because the lines' electrical parameters do not redistribute themselves in the same ratios as the lines' thermal limits. Therefore the choice of buses to retain plays an important role in ensuring that an equivalent could be meaningful in terms of both its power flow properties, as well as its transmission limits. The concept of back-bone equivalent [13] uses this idea to create groups such that they are geographically distant. Each of these groups can be represented by a single equivalent bus so that the resulting equivalent network retains the wide-area structure of the electric grid. This is illustrated in Figure 2.4. The image on the left shows an original network, and the image on the right shows an equiv-
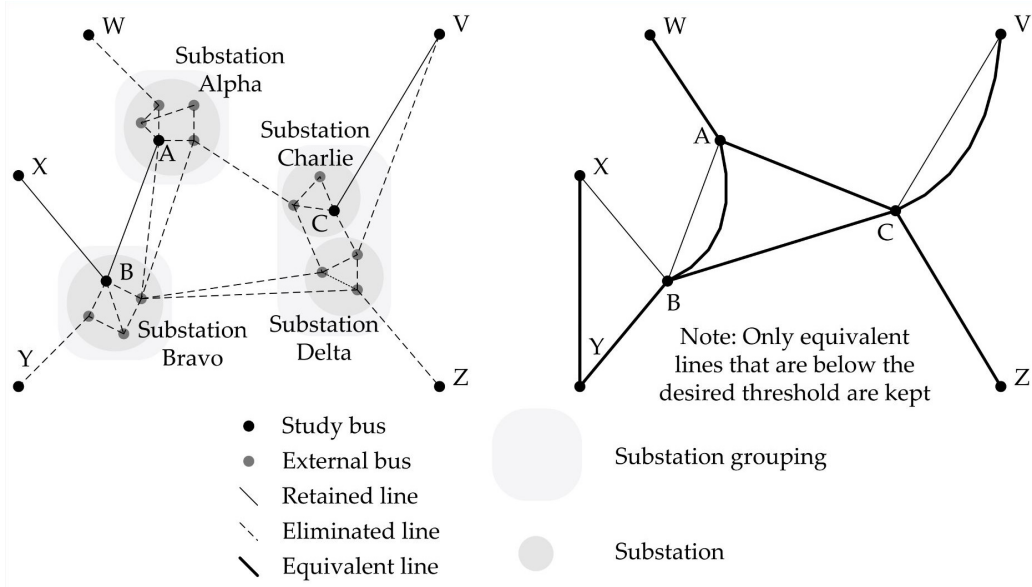
Figure 2.4: Illustration of top-down simplified concept.

alent network. In this example, the groups are considered to consist of one or mode substations. Substations are typically geographically distant, and hence, also electrically distant. This results in relatively fewer equivalent lines, which means fewer transmission paths, and hopefully more meaningful equivalent line limits. In contrast to the bottom-up LPNgroup-LPN-QP method, this would be considered top-down.

Preliminary work has been presented in [19], which illustrates the calculation of equivalent line limits for the North American Eastern Interconnection. This paper assumed a heuristic that the equivalent line connecting two buses in an equivalent network would also limit the TTC between the same two buses. (This heuristic can be loosely associated with LPN-QP when there is an exact solution.) The work presented in [19] has shown good computation times, but requires the inclusion of more heuristics, and better selection of buses. Work is in progress to improve on the method presented in [19], and hence scale the limit preserving network algorithm to be applicable towards an interconnection level system.

Part II

Measurement Aided Methods

CHAPTER 3

DYNAMIC MODE DECOMPOSITION FOR REAL-TIME MODAL IDENTIFICATION

3.1 Introduction

Electric power systems are never truly in steady state due to continuous small load fluctuations. However, control devices are able to keep a system's operating point within a narrow band during these small variations in load, which can be referred to as a pseudo-steady state. Sometimes planned/unplanned events can cause large perturbations that might result in more oscillatory behavior, and eventually lead to a new pseudo-steady state. These dynamics are known to occur in the transient stability time frame. Knowledge about the dominant oscillation modes characterizes a system's temporal evolution and stability attributes [20].

Modal identification from measurements provides information about oscillation frequencies and damping ratios, and their respective amplitudes and phase. Identifying poorly damped modes can help in tuning control strategies for better stabilization [20]. In today's highly interconnected electric grid, a disturbance originating from one part of the system can affect the entire system. Moreover, the presence of low-inertia and intermittent renewable generation units can also result in greater deviation from a desired operating point. These practical concerns in stability and control motivate the development of closer to real-time spatio-temporal awareness of a system's dynamic trajectories [21], which can be aided with accurate estimation of modes and mode shapes from measurements.

Modal estimation can be performed using any type of measurements (ambient, ring-down, or probing), and there are methods which are better suited for each data type (explained in Section 3.2). Ring-down analysis methods, such as Prony [22], Matrix Pencil (MPM) [23], Eigensystem Realization (ERA) [24] and Variable Projection (VPM) [24], have been applied to power

system measurements. However in this chapter, a method known as Dynamic Mode Decomposition (DMD), which originated in fluid dynamics in 2008 [25, 26], is implemented for ring-down analysis. First applied to power systems in [27], this work showed that DMD can be substantially faster than Prony.

This chapter focuses on the use of DMD for short time-interval modal identification for a wide-area interconnected power system. This chapter showcases DMD's strength in being able to accommodate a large set of measurement channels, while still remaining computationally fast. This chapter also shows that if different types of measurement channels are augmented with each other, it can help strengthen the precision of calculations, and hence allow a smaller time-window to be used. Before embarking on the details of DMD, the modal analysis problem is briefly described in Section 3.2, along with references to relevant past and current work that have been utilized in the industry. Next, mathematical theory of DMD is detailed in Section 3.3, followed by Section 3.4, which presents an application of DMD. Results and spatio-temporal visualization are shown, which convey the wealth of information extracted via DMD, so as to inspire its use by power system operators and in smart grid analytics. A discussion of DMD's fast computational speed is presented, and its use for on-line modal content monitoring is proposed. Benefits of utilizing both frequency and voltage data are presented, followed by a summary section.

3.2   Problem Statement and Literature Review

If a dynamic model of a power system is available, modal analysis could be done through the linearization of differential-algebraic equations (DAEs), representing a system and operating point of interest [28]. Apart from calculating modes, the participation factors (based on the eigenvectors of the linearized state matrix) reveal the impact of each state on each mode (and vice-versa). Some modes are affected by several states, and other modes are only impacted by a few states. Since different states can be associated with different geographic locations, modes are said to be local or inter-area depending on their geographic extent. Local and inter-area modes have also been observed in measurement data.

33

However, from a practical perspective, model-based modal analysis is challenging due to the time-varying nature of power systems. Approximate values can be obtained from calculations using planning models that usually run in an off-line manner. To reduce the dependency on models, and as an alternate approach, most measurement-driven modal analysis schemes calculate values of σ_i (damping), ω_i (angular frequency), c_i (amplitude) and ϕ_i (phase), and ultimately seek to reconstruct a signal as a sum of damped sinusoids,

$$\hat{y}(t) = \sum_{i=1}^{I} c_i e^{\sigma_i t} \cos(\omega_i t + \phi_i), \tag{3.1}$$

given the measurement signal $y(t)$. Typically this is done for a duration of time, $0 \leq t \leq T$. Methods like Prony, MPM, and ERA assume that the signal is an output of a linear time-invariant system, while VPM in [29] does not require this assumption, because non-linear basis functions can be chosen as part of VPM. Nevertheless, a signal can be expressed in terms of eigenvalues, $\lambda_i = \sigma_i \pm j\omega_i$. Similar to equation (3.1), a sum of damped sinusoids can be represented in discrete-time,

$$\hat{y}[n] = \sum_{j=1}^{J} d_j \left(\mu_j\right)^n, \tag{3.2}$$

for $n \in [0, N]$, $n \in \mathbb{Z}$, $d_j \in \mathbb{C}$, $\mu_j \in \mathbb{C}$, and where the sample number, n, and the sampling interval, Δt are related by the equation $n = t/\Delta t$. Typically, measurements are recorded with evenly-spaced samples, and therefore, the reconstructed signals in equations (3.1) and (3.2) are practically equivalent. The number of summation terms in equations (3.1) and (3.2) are I and J respectively. They satisfy the relationship $J - I =$ Number of complex conjugate eigenvalue pairs, because terms arising from complex conjugate pairs of the discrete-time eigenvalues (μ_j and $\overline{\mu}_j$) map to a single term in the continuous time summation in equation (3.1), i.e.,

$$d_j(\mu_j)^n + \overline{d}_j(\overline{\mu}_j)^n = c_i e^{\sigma_i n \Delta t} \cos(\omega_i n \Delta t + \phi_i). \tag{3.3}$$

Many methods calculate λ_i by finding μ_j from a discrete-time series, and require the time-series signal(s) to be uniformly sampled. If there are missing measurements, or signals are being combined from two or more sources, then interpolation and re-sampling are needed. Some implementations of these

34

methods have incorporated an optional pre-processing step for removing the initial/final/mean value of the signal and/or removing linear or quadratic trends [30, 31]. Some methods also incorporate the filtering of noise, and this also has proven useful in improving accuracy in some cases.

Methods like Prony [32], MPM [33, 34], and ERA [35] use a two-step procedure to first estimate the eigenvalues and then estimate the mode shapes [36, 37]. The origin of the Prony method can be traced to [32] from the field of Civil Engineering in 1974, and the work in [22] is the first application to power system data in 1990. In this method, the number of discrete-time eigenvalues, J, is specified as an input. The work in [38] clearly outlines the steps, and also shows its relation to the linear system prediction property. The idea behind MPM was first presented in the signal processing field, also in 1974 [33, 34], and appeared in power system literature in 1990 [23]. It is based on singular value decomposition (SVD) of measurement data, with a threshold applied to the singular values, and then calculation of μ_j from an estimated J-order backward linear prediction filter. ERA originated in aerospace engineering and was first published in 1985 [35], but its first application in power systems seems to appear only in 1993 [24]. This method is very similar to DMD, but obtains μ_j from the eigen decomposition of $\mathbf{A}' = \mathbf{\Sigma}^{-\frac{1}{2}}\mathbf{U}^{\mathrm{H}}\mathbf{Y}_1\mathbf{V}\mathbf{\Sigma}^{-\frac{1}{2}}$, as opposed to $\tilde{\mathbf{A}}$ shown later in equation (3.14) (Section 3.3).

Once μ_j has been calculated using one of the above-mentioned steps, the second step estimates the amplitudes and phases of the respective modes. The relation $\sigma_i + \mathrm{j}\omega_i = (\ln|\mu_j| + \mathrm{j}\angle\mu_j)/\Delta t$ for $-\pi < \angle\mu_j \leq \pi$, can be used to obtain the decay rates and angular frequencies. Thereafter the signal can be represented as

$$\hat{y}(t) = \sum_{i=1}^{I} c_i e^{\sigma_i t}[\cos\phi_i\cos(\omega_i t) - \sin\phi_i\sin(\omega_i t)]. \qquad (3.4)$$

In the continuous-time domain, there is no requirement for measurement samples to be equi-spaced. Each measurement point can be expressed as the sum shown in equation (3.4). By recognizing that the known quantities are σ_i, ω_i and t, and the unknowns are c_i, ϕ_i, the reconstruction can be represented by equation (3.5).

$$\hat{\mathbf{y}} = \mathbf{\Phi\beta}, \tag{3.5a}$$

$$\underbrace{\mathbf{\Phi}_{(t,*)}}_{1 \times (J+1)} = \begin{bmatrix} \left[e^{\sigma_i t} \cos(\omega_i t) \quad e^{\sigma_i t} \sin(\omega_i t) \right]^{\mathrm{T}}_{(2J-2I) \times 1} \\ \left[e^{\sigma_i t} \cos(\omega_i t) \right]_{(2I-J) \times 1} \\ 1 \end{bmatrix}^{\mathrm{T}}, \tag{3.5b}$$

$$\underbrace{\mathbf{\beta}}_{(J+1) \times 1} = \begin{bmatrix} \left[c_i \cos\phi_i \quad c_i \sin\phi_i \right]^{\mathrm{T}}_{(2J-2I) \times 1} \\ \left[c_i \cos\phi_i \right]_{(2I-J) \times 1} \\ c_0 \end{bmatrix}. \tag{3.5c}$$

An additional unknown, c_0, is also added to capture any dc offset present in the signal(s). This is a linear problem, which can be solved using a least-squares optimization method,

$$\underset{\mathbf{\beta}}{\text{minimize}} \, \|\mathbf{y} - \mathbf{\Phi\beta}\|_2^2, \tag{3.6}$$

where the solution is calculated with the pseudo-inverse of $\mathbf{\Phi}$, and $\mathbf{\beta}$ is obtained as $\mathbf{\beta} = \mathbf{\Phi}^\dagger \mathbf{y}$. In contrast, VPM [31, 29] recasts the linear least squares problem in expression (3.6) into a nonlinear least squares problem in (3.7). $\mathbf{\beta}$ can then be eliminated, and σ_i and ω_i (encapsulated as γ) are allowed to be decision variables.

$$\underset{\mathbf{\gamma}}{\text{minimize}} \, \left\| (\mathbf{I} - \mathbf{\Phi}_\gamma \mathbf{\Phi}_\gamma^\dagger \mathbf{y} \right\|_2^2. \tag{3.7}$$

This non-linear optimization problem for VPM (expression (3.7)) can be solved iteratively, with an initial guess of $\mathbf{\gamma}$. Then the values of $\mathbf{\beta}$ can be calculated. The work in [31, 29] uses an initial guess from ERA, and implements a line search method enabled by having a symbolic derivative of the objective function in (3.7). It is presented in [29] that VPM is superior to the other three methods as it can better minimize the difference between the $\hat{y}(t)$ and $y(t)$. This VPM implementation is also said to give tight control over the desired solution; however, details of the speed of this iterative algorithm were not mentioned in [29].

The industry has continued to seek alternatives so as to monitor system dynamics more closely, and for maintaining good operating points [39]. Work

36

has been done using a system identification approach [40], and also with ambient measurements [41, 42]. Methods like stepwise-regression [43] have also been formulated as an add-on to Prony analysis. Newer methods have been designed to better understand the error bounds in mode estimation [44], and also provide an understanding of the transfer-function representation of power systems [45]. Some of these measurement-based methods have also been tested with measurements taken during probing conditions. The concept of modal energy trending has recently been used, which utilizes a combination of frequency-domain and SVD methods [46, 47].

Similar to some other methods, DMD also consists of two steps, first estimating the modal frequency and damping, and then their respective amplitude and phase. One by-product of DMD's first step is a mapping between underlying dynamics and measurements, which is strategically used in simplifying the second optimization step (not done in Prony, MPM, and ERA). An assumption in DMD is an approximately constant linear mapping between consecutive measurement samples during one time-window. Despite this assumption, there is a firm theoretical foundation for applying DMD towards analyzing nonlinear power system dynamics [48]. DMD is considered as a numerical algorithm for finding the modes of the infinite-dimensional linear Koopman operator, which is defined for any nonlinear system [49]. Koopman modes are closed related to the system modes, and hence DMD modes accurately represent the system modes [50]. Arnoldi schemes in [51] and [52] are related to DMD via a similarity transformation [26], and in theory can also estimate Koopman modes; however, they are less robust than DMD, and hence not suitable for practical implementations. These Arnoldi schemes have been applied towards power systems [53, 54], but DMD has only been recently applied in [27].

3.3 Dynamic Mode Decomposition

DMD is inherently an ensemble spectral analysis technique, and therefore modal identification is done using a multi-signal approach. As shall be shown, a key advantage in the application of DMD to power systems is its computational speed. DMD is known to be able to extract coherent structures in either simulated or real measurements (even with noise) and associate them

to single oscillation frequencies [50], i.e. modes. DMD requires uniformly sampled measurements; for this, $N + 1$ samples are gathered for a time-window of interest, $\mathcal{T}_{[t-T,t]}$, with a sample interval of Δt and duration of T. Therefore, $T = N\Delta t$. Given M signals, each with $N + 1$ samples, these values are cast into a matrix,

$$\mathbf{Y} = \begin{bmatrix} \mathbf{y}_0 & \mathbf{y}_1 & \dots & \mathbf{y}_n & \dots & \mathbf{y}_N \end{bmatrix} \in \mathbb{C}^{M \times (N+1)}. \tag{3.8}$$

For generality, and from the perspective of the DMD algorithm, these measurements could be complex valued. Next, $\mathbf{Y}$ is separated into two matrices: $\mathbf{Y}_0 = \begin{bmatrix} \mathbf{y}_0 & \dots & \mathbf{y}_{N-1} \end{bmatrix}$ and $\mathbf{Y}_1 = \begin{bmatrix} \mathbf{y}_1 & \dots & \mathbf{y}_N \end{bmatrix}$. By assuming an approximately constant linear mapping, $\mathbf{A}$, consecutive measurement samples can be related by

$$\mathbf{y}_n \approx \mathbf{A}\mathbf{y}_{n-1}, \qquad \text{for} \qquad n = [1, N], n \in \mathbb{Z}, \tag{3.9}$$

for a time duration, T, and hence $\mathbf{Y}_1$ and $\mathbf{Y}_0$ are related by,

$$\mathbf{Y}_1 = \mathbf{A}\mathbf{Y}_0 + \boldsymbol{\rho}\boldsymbol{\eta}_N^{\mathrm{T}}, \tag{3.10}$$

where $\boldsymbol{\rho}\boldsymbol{\eta}_N^{\mathrm{T}}$ is the residual error. The work in [49] and [50] elaborates on the orthogonality of $\boldsymbol{\rho}$ to the measurement space spanned by the columns of $\mathbf{Y}_0$. Based on the projection theorem, this is the smallest possible error [49].

3.3.1 Estimation of oscillation frequencies and damping ratios

An economy-sized SVD is performed for $\mathbf{Y}_0$. Here, $\mathbf{U}$ consists of the left singular vectors or the Proper Orthogonal Decomposition (POD) modes that contain the spatial structures (referred to as topos), and $\mathbf{V}$ that contains the temporal structures (referred to as chronos) [50, 55]. The title of the paper in [56] – "On the Hidden Beauty of the Proper Orthogonal Decomposition" – aptly describes $\mathbf{U}$, which will play an instrumental role in a later stage (see equations (3.16a)). Out of the N singular values gathered, R non-zero values are selected based on a user-defined threshold. (From numerical experiments with different systems and dynamic events, this threshold tends to be dependent on the magnitude of time-constants associated with the dynamic models. For practical large-scale systems, this threshold value could

be tuned over time, and made more robust across a range of operating conditions.) This creates a diagonal matrix $\boldsymbol{\Sigma}$ with R singular values, and $\mathbf{U}$ and $\mathbf{V}$ are altered accordingly. This results in the following:

$$\mathbf{Y}_0 = \mathbf{U}\boldsymbol{\Sigma}\mathbf{V}^{\mathrm{H}}, \tag{3.11a}$$

$$\mathbf{U} = \begin{bmatrix} \mathbf{u}_1 \dots & \mathbf{u}_M \end{bmatrix}^{\mathrm{T}} \in \mathbb{C}^{M \times R}, \quad \text{and} \quad \mathbf{U}^{\mathrm{H}}\mathbf{U} = \mathbf{I}, \tag{3.11b}$$

$$\mathbf{V} = \begin{bmatrix} \mathbf{v}_1 \dots & \mathbf{v}_N \end{bmatrix}^{\mathrm{T}} \in \mathbb{C}^{N \times R}, \quad \text{and} \quad \mathbf{V}^{\mathrm{H}}\mathbf{V} = \mathbf{I}. \tag{3.11c}$$

DMD provides a lower dimensional optimal representation $\tilde{\mathbf{A}}$ (equation (3.12)), which is essentially the projection of $\mathbf{A}$ onto a POD basis. The reference in [48] provides details on the implication of this change of basis, and goes on to establish that an empirical reconstruction of $\hat{\mathbf{A}}$ is in fact merely a projection of the actual $\mathbf{A}$ in the range of the column span of $\mathbf{Y}_0$. This is logical because only the modes perturbed and contained in the measurements can be empirically estimated.

$$\tilde{\mathbf{A}} = \mathbf{U}^{\mathrm{H}}\mathbf{A}\mathbf{U} \qquad \text{where} \qquad \tilde{\mathbf{A}} \in \mathbb{C}^{R \times R}. \tag{3.12}$$

By substituting $\mathbf{Y}_0$ from (3.11a) into (3.10), while ignoring the residual term, and with some matrix manipulations, the following is obtained:

$$\mathbf{Y}_1 = \mathbf{A}\mathbf{U}\boldsymbol{\Sigma}\mathbf{V}^{\mathrm{H}} \implies \mathbf{Y}_1\mathbf{V}\boldsymbol{\Sigma}^{-1} = \mathbf{A}\mathbf{U}, \tag{3.13}$$

which results an expression for $\mathbf{A}\mathbf{U}$ in (3.13) that can be substituted into (3.12) to obtain $\tilde{\mathbf{A}}$, which is a numerical lower dimensional optimal representation of the mapping between consecutive measurement snapshots from $\mathbf{Y}$. The reasons for the optimality of $\tilde{\mathbf{A}}$ is documented in [48].

$$\tilde{\mathbf{A}} = \mathbf{U}^{\mathrm{H}}\mathbf{Y}_1\mathbf{V}\boldsymbol{\Sigma}^{-1}. \tag{3.14}$$

Next, the eigen decomposition of $\tilde{\mathbf{A}} = \mathbf{E}\mathbf{D}_{\mu}\mathbf{E}^{-1}$ provides the discrete-time eigenvalues, μ_j, and the eigenvectors, $\mathbf{e}_j$. These discrete-time eigenvalues can be conveniently converted to continuous-time eigenvalues: $\sigma_i + \mathrm{j}\omega_i = \lambda_i = \ln(\mu_j/\Delta t = (\ln|\mu_j| + \mathrm{j}\angle\mu_j)/\Delta t$ for $-\pi < \angle\mu_j \leq \pi$.

3.3.2 Estimation of amplitudes and phases of respective modes

Since $\tilde{\mathbf{A}}$ is a lower-dimensional representation of the inter-snapshot mapping of the measurements, it can be said that the dynamics are governed by equation (3.15a), which has R states. These states are not the same as the states from a DAE model of a power system, but can be thought of as a set of hidden states, which the work in [57] alludes to.

$$\mathbf{x}_n = \tilde{\mathbf{A}}\mathbf{x}_{n-1} = \tilde{\mathbf{A}}^n \mathbf{x}_0 \tag{3.15a}$$

$$= \mathbf{E}(\mathbf{D}_\mu)^n \mathbf{E}^{-1}\mathbf{x}_0 = \mathbf{E}(\mathbf{D}_\mu)^n \boldsymbol{\alpha}. \tag{3.15b}$$

The initial "state" conditions, $\mathbf{x}_0$ are unknown. With a substitution of $\tilde{\mathbf{A}}$ into (3.15a), $\mathbf{x}_n$, can be represented in terms of an unknown $\boldsymbol{\alpha}$ that is the initial amplitude of each discrete-time eigenvalue. It should be noted that $\boldsymbol{\alpha} \in \mathbb{C}^{R \times 1}$, and represents both the amplitude and phase of the continuous time modes. The beauty of the POD modes contained in $\mathbf{U}$ is that they allow a snapshot of measurements at time point n, i.e., $\hat{\mathbf{y}}_n$, to be linearly related to $\mathbf{x}_n$. This plays an instrumental role in linking the two stages of this DMD implementation [58].

$$\hat{\mathbf{y}}_n = \mathbf{U}\mathbf{x}_n \tag{3.16a}$$

$$= \mathbf{U}\mathbf{E}(\mathbf{D}_\mu)^n \boldsymbol{\alpha} = \mathbf{U}\mathbf{E}\mathbf{D}_\alpha \mathrm{diag}[(\mathbf{D}_\mu)^n]. \tag{3.16b}$$

Further substituting $\mathbf{x}_n$ from (3.15b) into (3.16a) allows a snapshot of reconstructed signals, $\hat{\mathbf{y}}_n$, to be represented in terms of the unknown $\mathrm{diag}(\mathbf{D}_\alpha = \boldsymbol{\alpha}$. In this way, $\mathbf{Y}_0$ can be approximated with the following equation:

$$\hat{\mathbf{Y}}_0 = \mathbf{U}\mathbf{E}\mathbf{D}_\alpha \mathbf{V}_{\mathrm{and}}, \tag{3.17}$$

which contains R unknowns in the $\boldsymbol{\alpha}$ vector, and where

$$\mathbf{V}_{\text{and}} = \begin{bmatrix} \mu_1^0 & \mu_1^1 & \cdots & \mu_1^{N-1} \\ \mu_2^0 & \mu_2^1 & \cdots & \mu_2^{N-1} \\ \vdots & \vdots & \ddots & \vdots \\ \mu_R^0 & \mu_R^1 & \cdots & \mu_R^{N-1} \end{bmatrix}. \tag{3.18}$$

This allows the estimation of amplitude and phase to be formulated as a least squares optimization problem,

$$\underset{\boldsymbol{\alpha}}{\text{minimize}} \quad \|\mathbf{Y}_0 - \mathbf{UED}_\alpha \mathbf{V}_{\text{and}}\|_{\text{F}}^2, \tag{3.19}$$

which minimizes the square of the Frobenius norm of the difference between $\mathbf{Y}_0$ and $\hat{\mathbf{Y}}_0$. Similar to Prony, MPM, ERA, and VPM, the optimization could have been formulated in the continuous time-domain, but with the availability of evenly-sampled data from devices such as PMUs, FDRs, and DFRs, a reliable and fast optimization solution method can be utilized in the discrete-time domain.

$$\underset{\boldsymbol{\alpha}}{\text{minimize}} \quad J(\boldsymbol{\alpha}) = \left\|\boldsymbol{\Sigma}\mathbf{V}^{\text{H}} - \mathbf{ED}_\alpha \mathbf{V}_{\text{and}}\right\|_{\text{F}}^2. \tag{3.20}$$

The formulation in expression (3.19) is further modified through a substitution of $\mathbf{Y}_0$ from equation (3.11a), which simplifies to the formulation into expression (3.20). As seen here, the estimation of complex amplitudes, $\boldsymbol{\alpha}$, is independent of the POD modes (topos) of $\mathbf{Y}_0$. This reinforces the statement in (3.16a), as the problem minimizes the difference between the hidden states, rather than the measurements themselves. In a way, the optimization problem in (3.20) is meant to minimize the difference between the weighted-chronos (in the measurements) and the temporal evolution of the modes. This objective function can be equivalently represented as

$$J(\boldsymbol{\alpha}) = \boldsymbol{\alpha}^{\text{H}}\mathbf{P}\boldsymbol{\alpha} - \boldsymbol{\alpha}^{\text{H}}\mathbf{q} - \mathbf{q}^{\text{H}}\boldsymbol{\alpha} + s \tag{3.21a}$$

where $$\mathbf{P} = \left(\mathbf{E}^{\text{H}}\mathbf{E}\right) \circ \overline{(\mathbf{V}_{\text{and}}\mathbf{V}_{\text{and}}^{\text{H}})}, \tag{3.21b}$$

$$\mathbf{q} = \overline{\text{diag}(\mathbf{V}_{\text{and}}\mathbf{V}\boldsymbol{\Sigma}^{\text{H}}\mathbf{E})}, \tag{3.21c}$$

and $$s = \text{trace}(\boldsymbol{\Sigma}^{\text{H}}\boldsymbol{\Sigma}). \tag{3.21d}$$

The derivation of equation (3.21a) from equation (3.20) is based on linear

algebra manipulations, which are documented in [58]. The optimal value of $\boldsymbol{\alpha}$ that minimizes $J(\boldsymbol{\alpha})$ is

$$\boldsymbol{\alpha} = \mathbf{P}^{-1}\mathbf{q} \tag{3.22a}$$

$$= \left(\left(\mathbf{E}^{\mathrm{H}}\mathbf{E} \right) \circ \overline{\left(\mathbf{V}_{\mathrm{and}}\mathbf{V}_{\mathrm{and}}^{\mathrm{H}} \right)} \right)^{-1} \overline{\mathrm{diag}(\mathbf{V}_{\mathrm{and}}\mathbf{V}\boldsymbol{\Sigma}^{\mathrm{H}}\mathbf{E})}, \tag{3.22b}$$

where $\mathbf{M} \circ \mathbf{M}$ is the element-wise multiplication of matrices, and $\overline{\mathbf{M}}$ is the conjugate operation. Having a closed form solution is particularly useful, as it eliminates the need of iterations and initial conditions.

3.3.3   Signal reconstruction and performance evaluation metric

Since the application of DMD to power system measurements is intended for on-line modal identification, signals can also be efficiently reconstructed by choosing the appropriate rows and columns from matrices that are already used/calculated in the DMD algorithm. From equation (3.17), it can be shown that the reconstruction of measurement m and time point n is given by a summation of the individual modes weighted by their respective amplitudes, then mapped to R hidden states by the eigenvectors of $\tilde{\mathbf{A}}$, and then mapped via the POD modes to the mth signal. Succinctly, this is

$$\hat{y}_m[n] = \mathbf{u}_m^{\mathrm{T}} \sum_{r=1}^{R} \mathbf{e}_r \alpha_r \left(\mu_r \right)^n = \sum_{r=1}^{R} \hat{y}_{(m,r)}[n], \tag{3.23}$$

where

$$\hat{y}_{(m,r)}[n] = \mathbf{u}_m^{\mathrm{T}} \mathbf{e}_r \alpha_r \left(\mu_r \right)^n \tag{3.24}$$

is the contribution of each mode. This allows for efficient spatio-temporal slicing and dicing of an array of measurement signals. In addition to leveraging DMD for its computational speed (see Section 3.5), it also may be of interest to compare the accuracy of reconstructed signals across different time-windows, or evaluate it with different measurements. For this, a normalized version of the optimal value of the objective function in equation (3.21a) can be utilized as a metric, i.e., $J_{\mathrm{norm}} = J(\boldsymbol{\alpha})/(RN)$.

3.4 Application of DMD

3.4.1 Synthetic measurement data via simulation

Power system operators have faced challenges in deciphering all the data that is available at control centers. Sensors such as phasor measurement units (PMUs), frequency disturbance recorders (FDRs) [59], and digital fault recorders (DFRs) are gathering huge volumes of data, and hence there has been an evolving need to view more information and less data. In this chapter, a transient stability simulation of an industry-grade dynamic model of a large-scale interconnected power grid was used to collect frequency measurements at 1696 high-voltage locations spanning a wide-area (Figure 3.1) but a small portion of the total buses in the system. All load models were augmented with a Gaussian load noise model (7% standard deviation) with a low pass filter ($\tau = 0.5$ s) to capture the effect of random load fluctuations, and hence introduce noise in the measurements. In this simulation a large
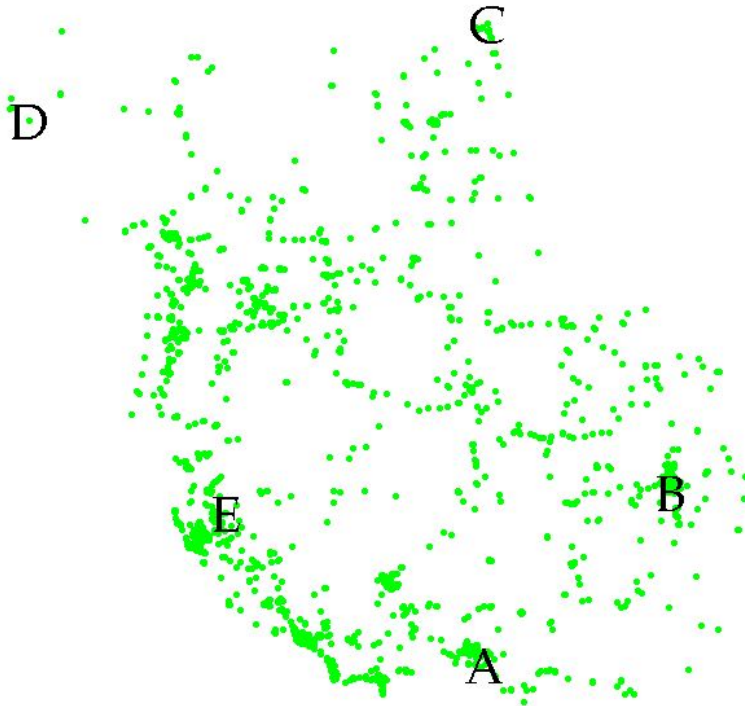

Figure 3.1: Spatial visualization of 1696 measurement locations from an interconnected power grid, with 5 locations labeled.
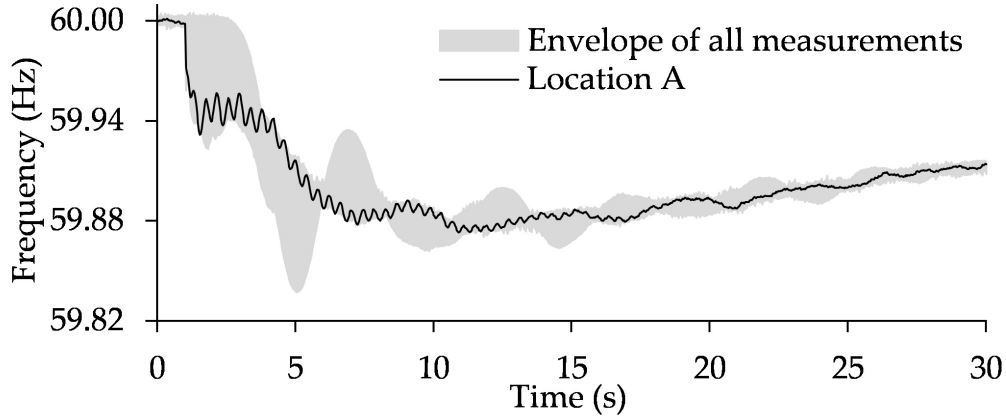
Figure 3.2: Frequency measurements from 1696 locations.

perturbation was introduced through the loss of a large generation unit at $t = 1$ s, and transient behavior was recorded for 30 s. Figure 3.2 shows the spread of frequencies at 1696 locations during the fault, with one location highlighted. Measurements were gathered at 30 samples/second, which translated to a raw data rate of about 3.26 Mbits/s. Even though this may seem reasonable, its spatio-temporal analysis and visualization are challenging. Practical limits to displaying data at control centers necessitate holistic measures such as mode frequencies and damping ratios to be tracked during transient contingencies, which can possibly be incorporated into alarm processing. On-line modal identification via DMD can be a way to process such time-series data, as it seems to be computationally advantageous [27].

The set of measurements gathered from the simulation in Section 3.4.1 is treated as a streaming data source input. The DMD algorithm was implemented in a software code, which accepts this data stream. A trailing T-second time-window concept was utilized, such that the output data reflects the modal content in the prior T seconds of measurements. This time-window was advanced with a step-size, t_{step}. The idea of sliding time-windows is common for speech recognition, where the signal content is time-varying, and has also been utilized in power systems literature [60]. The power system measurements being processed in this example originate from a non-linear time-varying system. Therefore, frequency-domain information is expected to vary with time. The choice of the window length, T, is application specific [61] as it presents a trade-off between resolutions in time-domain or frequency-domain. For power system measurements, this value of T can be

44

tuned based on historical knowledge of the approximate system eigenvalues. In the example being presented here, $T = 6$ s and $t_{\text{step}} = 0.2$ s were chosen. However, these are suggested values, which could be modified based on user preference. In comparison to other moving-window implementations in power systems literature (e.g. [60]), a much smaller value of t_{step} could be used, as DMD is expected to be computationally much faster. This significant overlap between consecutive time-windows, and the fast solution of DMD, is hoped to allow for continual short-interval mode tracking. This is elaborated on in Sections 3.5 and 5.1.

3.4.2 Results from one time-window

As discussed in Section 3.3, DMD is capable of analyzing multiple signals simultaneously. In this example, all 1696 measurement signals were ana-

Table 3.1: Modal analysis of frequency measurement at location A during time-window $\mathcal{T}_{[4.0,10.0]}$.

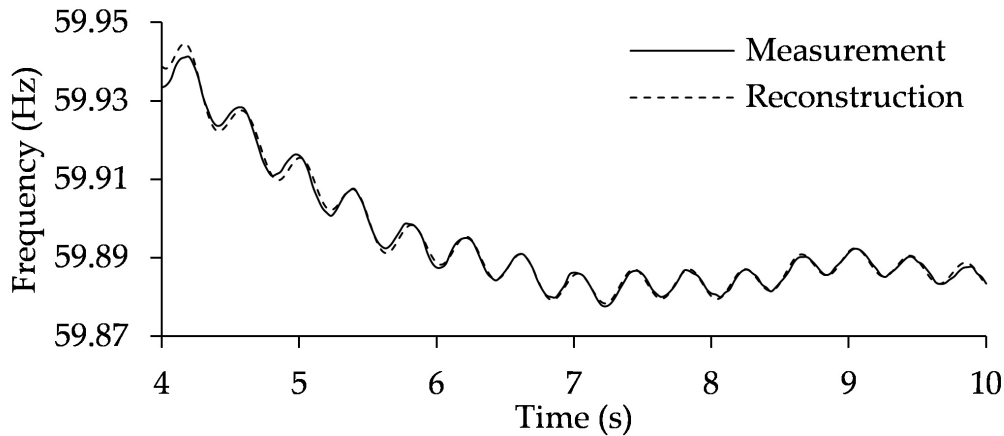| Modes	Oscillation frequency (Hz)	Damping ratio
1	0.23072	0.10387
2	0.29410	-0.092304
3	0.47078	0.26472
4	0.62376	0.00099628
5	2.4786	0.0069160

Figure 3.3: Measured and reconstructed frequency signals at Location A, during time-window, $\mathcal{T}_{[4.0,10.0]}$.
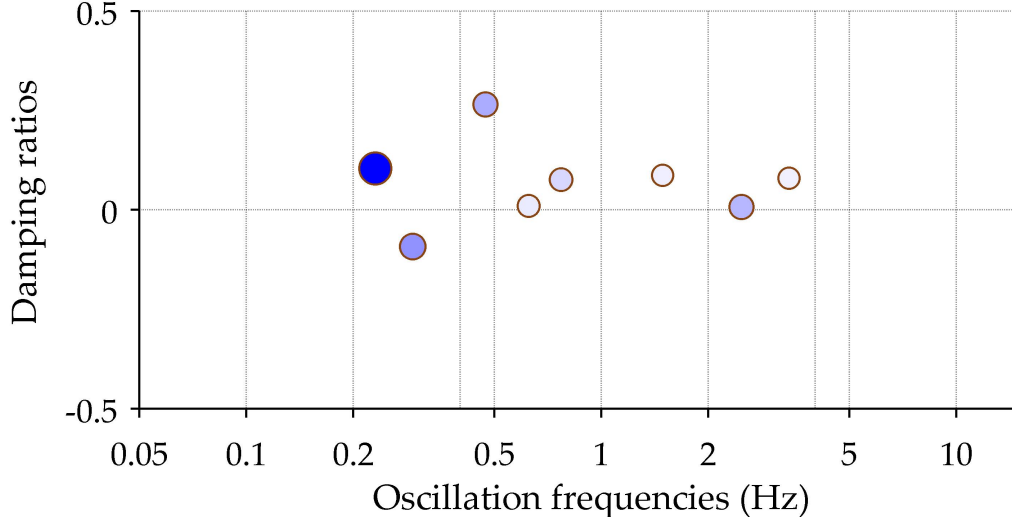
45

Figure 3.4: Plot of damping ratios vs. oscillation frequencies (Hz) at Location A, during time-window, $\mathcal{T}_{[4.0,10.0]}$.
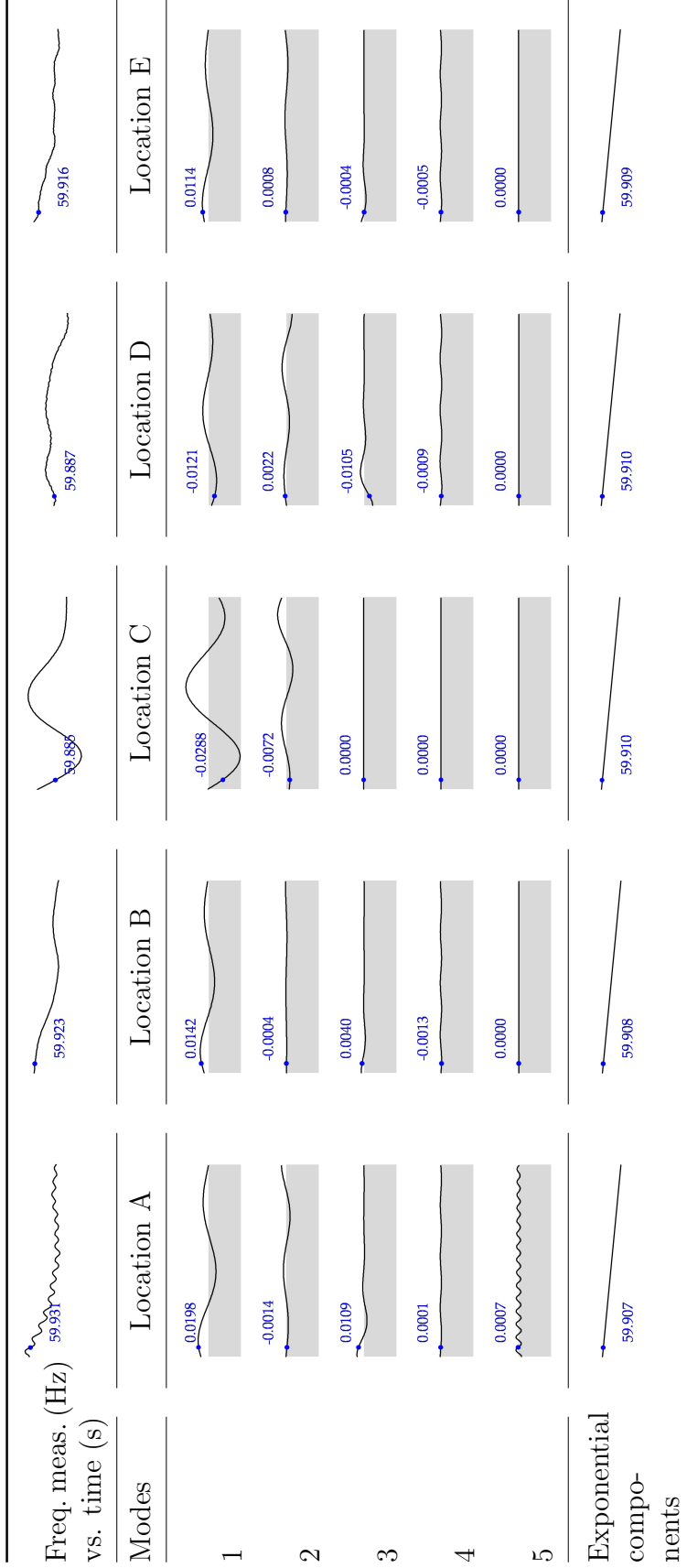
lyzed concurrently for each time-window. Assuming one of those signals, say at location A, was being monitored, its modal content for time-window $\mathcal{T}_{[4.0,10.0]}$ is summarized in Table 3.1. Listed are some of the modes, where modes 1-3 are the three most dominant modes observed in this signal. The time-series frequency measurement in Figure 3.3 shows a zoomed in view of the highlighted measurement signal from Figure 3.2. Also shown here is the DMD-based reconstruction of this signal, which is a close match. Quantitatively, the optimization residue was $J_{\text{norm}} = 3.12 \times 10^{-12}$, representing the combined residue of all signal reconstructions in this time-window.

Similar to the observations in [27], DMD is able to perform well and provides meaningful results. Figure 3.4 is a plot of the damping ratios and oscillation frequencies. Both the size of the dot and the filled shading represent the rms amplitude of the corresponding modal component. As seen, mode 1 is the dominant ac mode, and hence has the most influence on the frequency signal at location A. The damping ratios for modes 2 and 4, are negative and very close to zero, respectively, which could be a cause of concern if they fail to improve in subsequent time-windows.

3.4.3 Temporal analysis

Similar to methods like Prony, MPM, and ERA, efficient reconstruction of time-series signals (see Section 3.3.3) can be done using outputs of DMD. Table 3.2 shows the modal breakdown of five of the 1696 locations shown in Figure 3.1, where each column corresponds to one location. The temporal analysis shown is for time-window $\mathcal{T}_{[4.0, 10.0]}$, and the modes correspond to those in Table 3.1. At locations B and C, the effect of mode 1 is clearly visible in the measurements. In contrast, the contribution of mode 1 to the measurements at locations D and E is less obvious, but DMD is able to show that mode 1 is approximately anti-phase at D vs. E. Through DMD, differences in phase shifts and amplitudes can be efficiently quantified for multiple signals. It is interesting that mode 5 almost exactly aligns with the higher frequency oscillation observed in the measurement at location A. This highly granular information about individual modes' amplitude and phase, or their time-series reconstruction could be a distilled input for wide-area control strategies. As illustrated, all modes have a zero dc value, except for the exponential components that originate from real eigenvalues. Similar to [27], no de-trending or removal of dc offsets has been applied to the measurements in this analysis, which is sometimes otherwise necessary in methods.

Table 3.2: Temporal visualization of modes at locations A-E during time-window $\mathcal{T}_{[4.0,10.0]}$ (modes 1-5 are listed in Table 3.1).
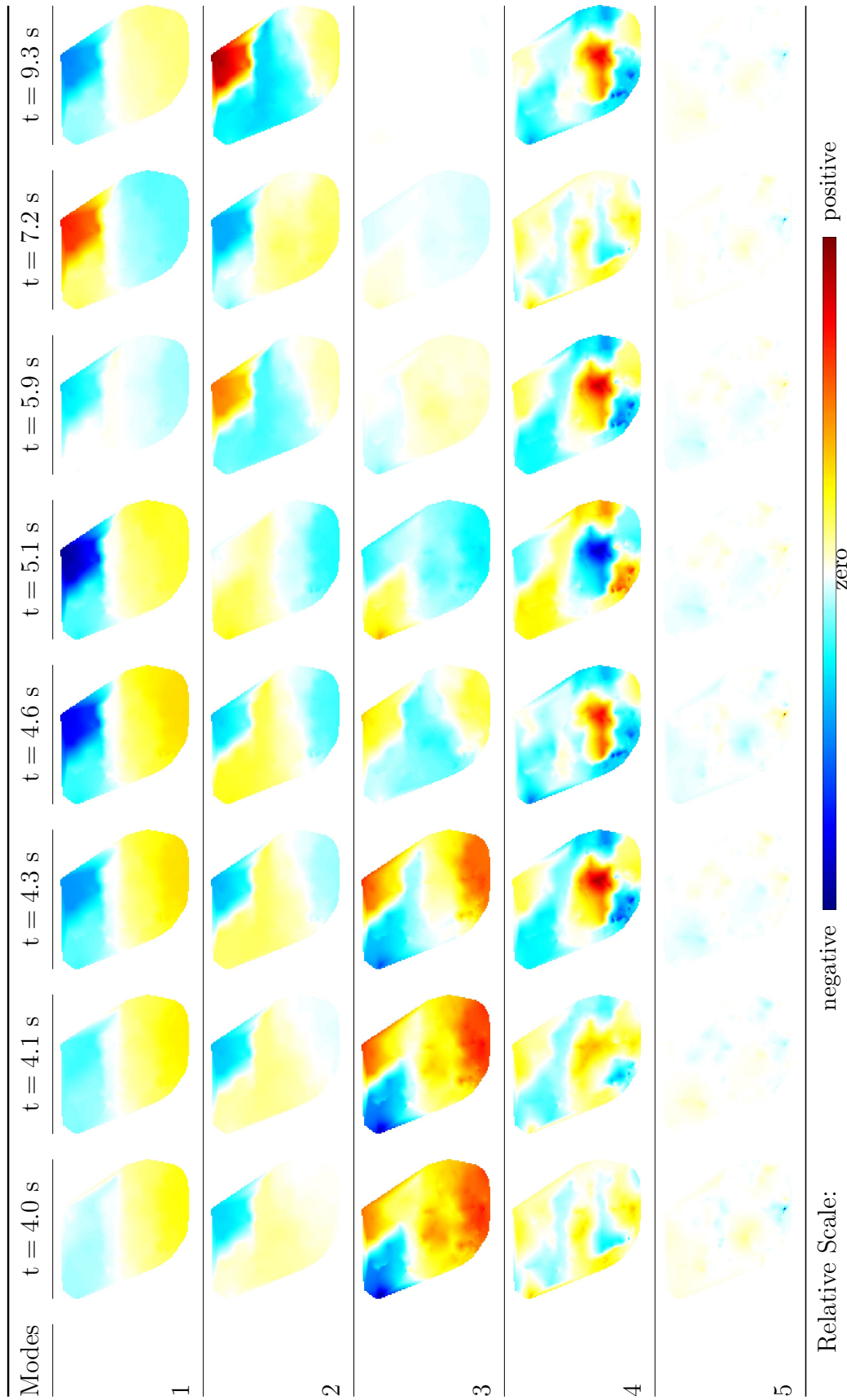
Freq. meas. (Hz) vs. time (s)	Location A	Location B	Location C	Location D	Location E
	59.931	59.923	59.885	59.887	59.916
Modes	**Location A**	**Location B**	**Location C**	**Location D**	**Location E**
1	0.0198	0.0142	-0.0288	-0.0121	0.0114
2	-0.0014	-0.0004	-0.0072	0.0022	0.0008
3	0.0109	0.0040	0.0000	-0.0105	-0.0004
4	0.0001	-0.0013	0.0000	-0.0009	-0.0005
5	0.0007	0.0000	0.0000	0.0000	0.0000
Exponential components	59.907	59.908	59.910	59.910	59.909

Note: Sparklines show time-series values at the same scale, where negative values are contained within the grey regions.

3.4.4 Spatial analysis

In real-time operations, the right information at the right time can be crucial for operating power systems within desired limits. The true potential of measurement data can be harnessed with real-time computational intelligence, and DMD might be able to contribute significantly. Since the implementation of DMD in this chapter seems to meet the speed and accuracy standards for on-line use, many traditionally off-line analyses could be done closer to real-time. One example is spatio-temporal visualization of individual mode amplitudes (i.e., the values in equation (3.24)) via on-line creation of simple animation. Table 3.3 shows snapshots from such animation. The area shown corresponds to that from Figure 3.1, and is able to capture wide-area effects of individual modes. For confidentiality reasons, the absolute value of the amplitudes have been excluded; however, the snapshots show modal amplitudes varying in time and space. These holistic animations provide a more intuitive approach than looking at numerical values of modal amplitudes and phase shifts. For example, the spatial evolution of mode 4 can been seen as a ripple (or wave) propagating through the entire interconnection. Areas oscillating against each other at mode 4 frequency are quickly noticeable. Dominant mode 1 partitions the interconnection into two regions oscillating against one other. Also seen is the growth of undamped mode 2, and it partitions the interconnection into three regions. The faint coloring in the last row of spatial snapshopts indicates that mode 5 is mainly observed around location A, and has very small amplitudes elsewhere in the interconnection.

For more practical purposes, modal content triggers/alarms could be used to automatically create such animation, which could aid in system-wide situational awareness of dynamic trajectories. The data for creating this animation is readily available from the matrices used in the DMD calculation, and animation could be created and destroyed on-the-fly, based on system-specific modal monitoring criteria. If sufficient resources are available, spatio-temporal visualization of one or more modes could be continually viewed at control centers.

Table 3.3: Spatial visualization of mode amplitudes during time-window $\mathcal{T}_{[4.0,10.0]}$ (modes 1-5 are listed in Table 3.1).

Modes	t = 4.0 s	t = 4.1 s	t = 4.3 s	t = 4.6 s	t = 5.1 s	t = 5.9 s	t = 7.2 s	t = 9.3 s
1								
2								
3								
4								
5								

Relative Scale: negative — zero — positive

3.5 On-line Modal Content Monitoring

Similar to Figure 3.4, Table 3.4 contains the same type of plots showing the evolution of modes for three successive time-windows. Once again, both the size of the dot and the intensity of the fill shading represent the relative rms amplitudes. Although only one signal is shown here, the current code calculates the same information for all measurements simultaneously. The analysis shows that the modal content of measurements varies through time, as well as the energy content of each mode. Viewed as an animation, the movement of these dots resembles a root-locus, where some dots merge/split at different points in time. As discussed in [27], DMD is known to have shown close agreement with Prony and Koopman methods. With seemingly negligible loss in accuracy, the key advantage of DMD is its fast computation. DMD has already been able to perform in real-time for background/foreground separation in video [62], and for tumor ablation simulations [63]. In this chapter, DMD was also able to perform fast on-line calculation of modes and their complex amplitudes. This amounted to a computation time of 0.105 s for simultaneous processing 1696 measurements, each with 181 time samples from a 6 s sliding window. In the current implementation and with the data set mentioned, modal identification can be repeated every 0.105 s on a 2.7 GHz dual core processor. Advancing the time-window every 0.1 s allowed the algorithm to run on par with real-time.

In addition to the above-mentioned settings, the software was also evaluated by varying the number of measurement signals and the number of samples in each time-window. Simple timing tests with the current code showed that the DMD computation time scaled at about $\mathcal{O}(N^3)$ with respect to the number of samples in the time-window of interest, and at about $\mathcal{O}(M)$ with respect to the number of measurement channels, similar to the result published in [64]. Given the computational complexity and absolute time needed to solve, DMD is efficient for modal identification, especially in being able to accommodate a large number of measurement channels. This characteristic is further exploited in Section 5.1, to improve precision, with a low trade-off in computation time.

From the example in Table 3.4, it can be seen that the variation of the dominant ac mode around 0.2 Hz is in the range of about 0.17-0.23 Hz, across sliding time-windows separated by 0.2 s. Similarly, its damping ratio

Table 3.4: Real-time modal content monitoring of frequency signal measurement at location A (labeled in Figure 3.2).
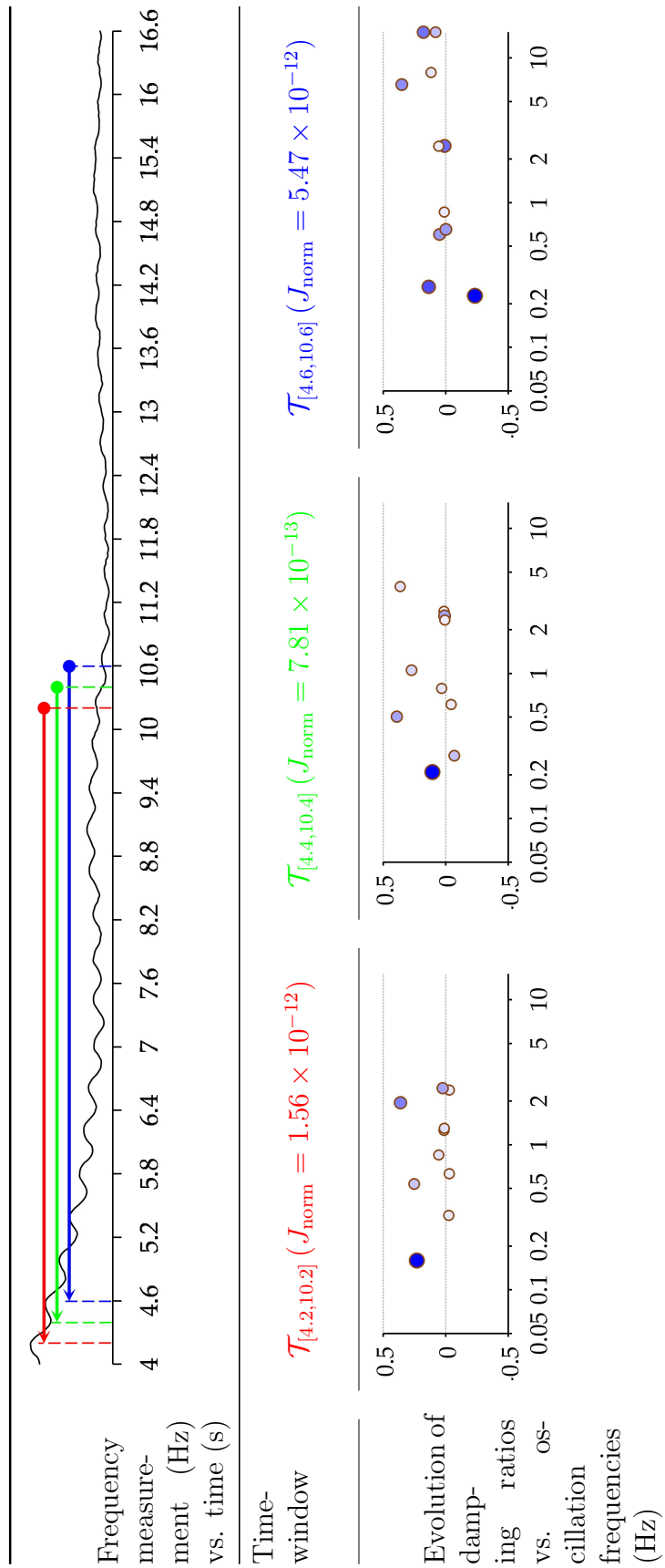
also varies. This relatively rapid change in the dominant mode calls attention to some of the limitations of DMD, specifically in terms of the precision and the practical usefulness of mode values, which seem to be changing rapidly. An important conclusion in [64] is that the error in DMD is significantly attributed to the form, quality, and quantity of the input data. One of the suggested approaches is to incorporate as many measurement channels as possible, which helps for datasets with poorer signal-to-noise ratios. Prior work in fluid dynamics has also concluded that measurement locations need to be widely distributed throughout the system of interest [26], and even better if they collectively capture the full phase cycle of the modal constituents [64]. In an attempt to improve the time-varying precision of DMD results, the effects of augmenting datasets, and using a slightly longer time-window are studied in the next chapter.

3.6   Summary

The speed and precision demonstrated by DMD, while utilizing multiple channels of frequency data, positively demonstrate the usability of DMD in on-line modal analysis implementations for large-scale power systems from measurement data, with noise. As a result of this real-time capability, additional intelligence could be incorporated into existing control center frameworks used in the industry. Modal content alarm processing could be a direct consequence of this work, and it is also expected that the outputs of DMD can be further utilized for a variety of control and stability algorithms. It is proposed that all transmission-level power system measurements could be channeled through a DMD-powered modal analysis engine, which would assign criteria-based modal tags at particular time points and/or certain measurements. Pertaining to these tags, the most critical spatio-temporal information could be made available at control centers in an on-line fashion. All these tags could also be saved with the measurements, and it could save many man-hours in retrieval of data for post-event analyses.

CHAPTER 4

AN INTERACTIVE TOOL FOR MEASUREMENT-DRIVEN MODAL ANALYSIS OF LARGE-SCALE POWER SYSTEMS

4.1 Background

Dynamic Mode Decomposition (DMD) is a relatively new method for measurement driven multi-signal modal identification. It originated in the field of fluid dynamics [26, 50] and has recently been applied to power systems. DMD has exhibited good accuracy, and significantly faster speed than Prony [27]. The work in [65] has continued to build on the work in [27], and has been able to further demonstrate DMD's computation speed and scalability in accommodating more measurement signals and higher sampling rates. As part of ongoing research efforts, an interactive modal analysis tool has been designed. This tool has been coded in Matlab, and uses DMD to conduct modal analysis. In this chapter, the focus is on describing the capabilities built into this tool, and explaining the various user options that are available in the current version.

Modal analysis is an integral part of dynamic stability assessments. A system's temporal evolution and stability attributes can be characterized by knowing the dominant oscillation frequencies and damping ratios [20]. Power system modal analysis helps accomplish this, and is a task usually done by dispatchers, planning engineers, and/or operational engineers, for the purpose of oscillation detection and mitigation [66]. The type of analysis can be either off-line or on-line depending on the intended use; however, engineers make use of commercial applications for proper data management and automated analyses.

These tools have aided engineers in automating their daily tasks, and ultimately provide quantitative results to support decision making. There are various commercial power system analysis software packages that contain modal analysis tools. Some of these tools are model-driven, while others are

measurement-driven. Regardless of the approach taken, the two methods provide information about the mode frequencies, damping ratios and their respective mode shapes. With these, the impact of each mode on the system's dynamic states, or measurement signals, can be understood. This analysis can also provide an understanding of inter-area or local oscillation modes, which can be utilized for various control strategies.

In recent years, measurement-driven modal analysis has gained more traction within the power industry [21]. To address this need, various commercial software packages such as Phasor Grid Dynamics Analyzer (PGDA) [67] and PowerWorld Simulator [68] now have modal analysis tools. These tools utilize algorithms such as Prony [22], Matrix Pencil [23], Hankel Total Least Squares, Yule Waker, Fast Fourier Transforms, and Variable Projection.

Similarly in academia, modal analysis continues to be an active area of research, and there are tools that have been developed in academic institutions. One example is a tool based on Variable Projection [31] that was recently developed in partnership with industry. Also, there are several other publications that have presented improvements in algorithms [47, 44, 43], and have utilized hybrid methods. MANGO is such a hybrid algorithm, which aims to provide recommended actions (such as generation re-dispatch or load reduction) and aid grid operation decision making for mitigating inter-area oscillations [39].

The tool that will be presented in this chapter utilizes DMD for modal identification. The purpose of this tool is to illustrate the concepts of modal analysis in an interactive and visual manner. As shall be shown, spatio-temporal analysis of modes and their respective amplitudes can be done relatively quickly, and the outputs of the DMD algorithm make it possible to slice and dice measurements to better understand their constituent signals.

This chapter gives details on the input file format and user interface, and provides an example of modal analysis. Also presented are explanations of customizable user options, and a brief study that emphasizes the importance of choosing appropriate time-window durations and measurement sampling rates. Before describing the tool in greater detail, a summary of the DMD algorithm, along with key references, is presented.

As described in Chapter 3, DMD is a data processing method that can extract coherent structures with a single frequency from numerical or experimental data sequences [50]. DMD consists of two parts – (i) estimation

of discrete-time eigenvalues, and (ii) estimation of complex amplitudes of respective modes. Since DMD is inherently an ensemble spectral analysis technique, modal analysis is carried out using a multi-signal approach. The method described earlier in Chapter 3 is shown below in Algorithm 2. Although not shown in this chapter, DMD utilizes a least-squares optimization approach [58]. Hence, the optimal value of $\boldsymbol{\alpha}$ given in Algorithm 2 minimizes the least-squares residue between all the measurement and reconstructed signals. The tool being described in this chapter utilizes this algorithms to implement modal identification.

Algorithm 2 DMD.

Data: $\mathbf{Y} = \begin{bmatrix} \mathbf{y}_0 & \mathbf{y}_1 & \ldots & \mathbf{y}_N \end{bmatrix} \in \mathbb{C}^{M \times (N+1)}$
Result: $\mathbf{U}$, $\mathbf{E}$, $\boldsymbol{\alpha}$, and $\boldsymbol{\mu}$

1: $\mathbf{Y}_0 \leftarrow \begin{bmatrix} \mathbf{y}_0 & \ldots & \mathbf{y}_{N-1} \end{bmatrix}$, and $\mathbf{Y}_1 \leftarrow \begin{bmatrix} \mathbf{y}_1 & \ldots & \mathbf{y}_N \end{bmatrix}$

    Part I Estimation of discrete-time eigenvalues
2: $\mathbf{U}\boldsymbol{\Sigma}\mathbf{V}^{\mathrm{H}} \leftarrow$ economy size SVD of $\mathbf{Y}_0$, and retain R non-zero singular values
3: $\tilde{\mathbf{A}} \leftarrow \mathbf{U}^{\mathrm{H}}\mathbf{Y}_1\mathbf{V}\boldsymbol{\Sigma}^{-1}$
4: $\mathbf{E}\mathbf{D}_{\mu}\mathbf{E}^{-1} \leftarrow$ eigen decomposition of $\tilde{\mathbf{A}}$
5: $\boldsymbol{\mu} \leftarrow \mathrm{diag}(\mathbf{D}_{\mu})$

    Part II Estimation of complex amplitudes
6: $\boldsymbol{\alpha} \leftarrow \left(\left(\mathbf{E}^{\mathrm{H}}\mathbf{E}\right) \circ \overline{\left(\mathbf{V}_{\mathrm{and}}\mathbf{V}_{\mathrm{and}}^{\mathrm{H}}\right)} \right)^{-1} \overline{\mathrm{diag}(\mathbf{V}_{\mathrm{and}}\mathbf{V}\boldsymbol{\Sigma}^{\mathrm{H}}\mathbf{E})}$
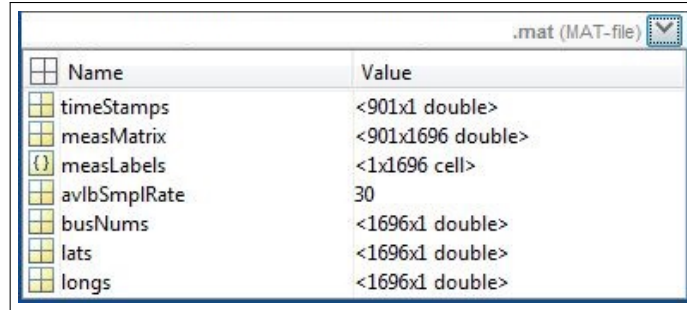
Notes:

(i) $\mathbf{U}, \mathbf{V} \in \mathbb{C}^{M \times R}$, $\mathbf{U}^{\mathrm{H}}\mathbf{U} = \mathbf{I}$, and $\mathbf{V}^{\mathrm{H}}\mathbf{V} = \mathbf{I}$.

(ii) $\tilde{\mathbf{A}} \in \mathbb{C}^{R \times R}$.

(iii) $\mathbf{M} \circ \mathbf{M}$ represents element-wise multiplication of two matrices.

(iv) $\mathbf{V}_{\mathrm{and}} = \begin{bmatrix} \mu_1^0 & \mu_1^1 & \ldots & \mu_1^{N-1} \\ \mu_2^0 & \mu_2^1 & \ldots & \mu_2^{N-1} \\ \vdots & \vdots & \ddots & \vdots \\ \mu_R^0 & \mu_R^1 & \ldots & \mu_R^{N-1} \end{bmatrix}$.

Figure 4.1: Contents of the input data file.

4.2 Input Data

Although $\mathbf{Y}$ is the only required input for the DMD algorithm, a few other inputs are necessary to make use of all the features contained in the tool that will presented in Section 4.3. The current version of this tool accepts an input data file in the MAT format. As an example, Figure 4.1 shows $M = 1696$ measurements, with 30 samples/s, and a total of 901 time samples. From these values, the tool extracts the relevant $\mathbf{Y}$, based on time time-window of interest. If the measurement data is in a CSV file format, it should be straightforward to transform it into the format described below. Geographical coordinate data is optional, but is needed for spatial visualization.

  (i) *timeStamps*: Time stamps for the measurements

 (ii) *measMatrix*: Time series values of measurements

(iii) *measLabels* and *busNums*: Text labels and numbering

(iv) *avlbSmplRate*: Sampling rate of the measurements series

 (v) *lats* and *longs*: Latitude-Longitude, or X-Y coordinates

4.3 Interactive User Interface

Figure 4.2 shows a screen-shot of the user interface of the modal analysis tool that was designed in Matlab and is based on the DMD algorithm. It incorporates a spatio-temporal visualization approach in presenting the estimated
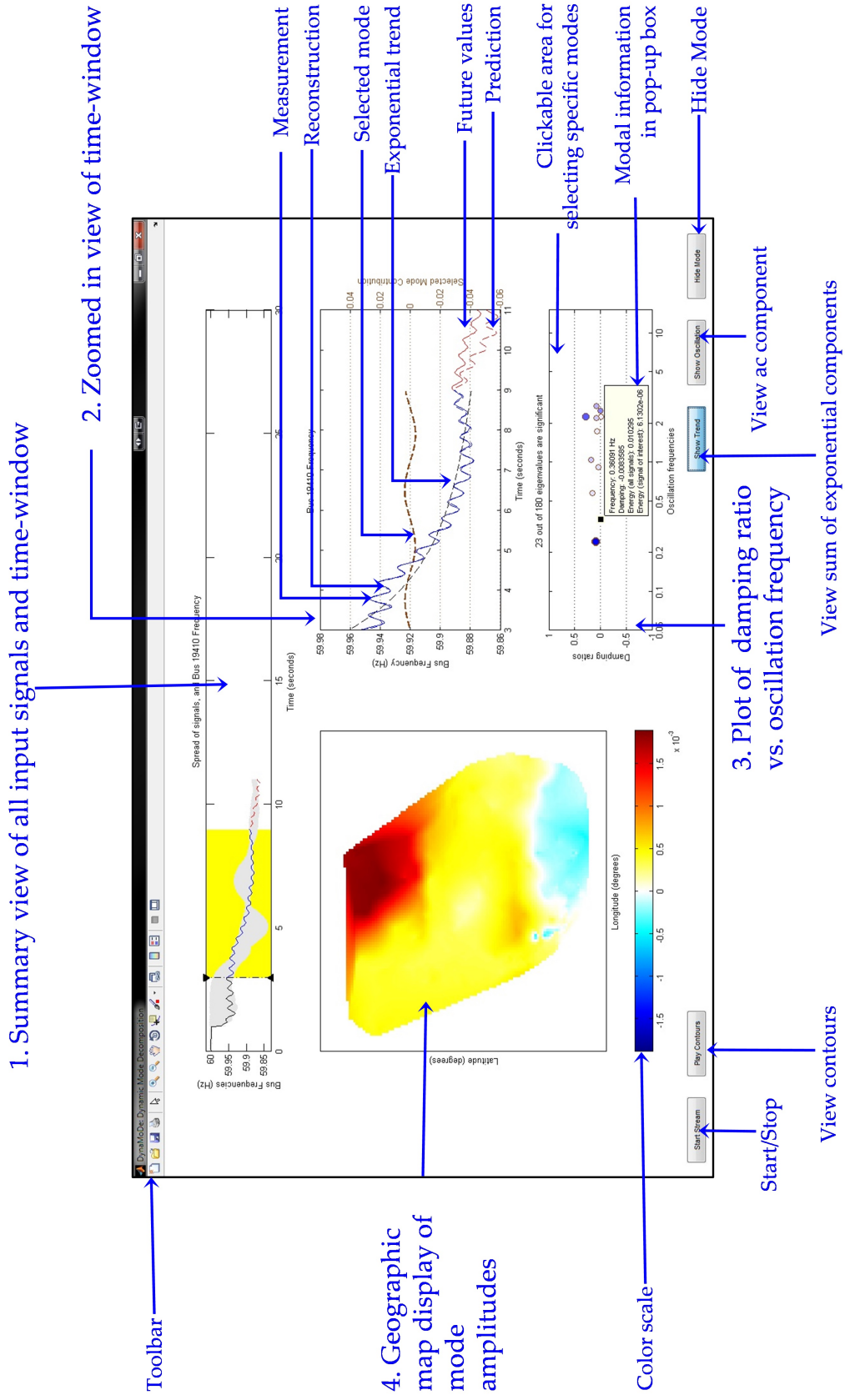
1. Summary view of all input signals and time-window

2. Zoomed in view of time-window

Measurement
Reconstruction

Selected mode
Exponential trend

Future values
Prediction

Clickable area for
selecting specific modes

Modal information
in pop-up box

Hide Mode

View ac component

3. Plot of damping ratio
vs. oscillation frequency

View sum of exponential components

View contours

Start/Stop

Color scale

4. Geographic
map display of
mode
amplitudes

Toolbar

Figure 4.2: User interface of the interactive tool developed with DMD in Matlab.

modes and mode shapes from measurement data, as opposed to reading values of eigenvalues and eigenvectors. As shown here, the user interface consists of four sections – (i) Summary view of all input signals and time window, (ii) Zoomed-in view of time-window, (iii) Plot of damping ratio vs. oscillation frequency, and (iv) Geographic map display of mode amplitudes.

Upon launching this tool in Matlab, users are first presented with an option to select a main input file, as described in Section 4.2. In addition to this, users have the capability to customize several options such as (i) the time-window duration for the analysis, (ii) the sampling rate of the raw measurements, (iii) the signal to monitor and visualize, (iv) the energy-based thresholds for signal reconstruction, (v) the time horizon for prediction of signals, (vi) the time-step for the sliding window, and (vii) the choice between streaming or snapshot mode. These user options are explained later in Section 4.4. Depending on the choices made, the user interface adapts to reflect the desired options.

Figure 4.2 shows a screen-shot of the quantitative outputs and visualization capabilities, while the tool is in use. In this view, a set of frequency measurements are being simultaneously analyzed. Although modal analysis is being performed on all of the input data, only one measurement is being visualized. The highlighted signal from the summary view is enlarged in the zoomed-in view, which also provides a reconstruction of the signal, and is capable of showing the contribution of each individual mode. Predicted and future values of the signal are also shown. The modal content of the chosen signal can be quickly deciphered by looking at the plot of damping ratio vs. oscillation frequency. The color of the dots represents the rms amplitude of the constituent modes. This area of the tool has a clickable interface, which allows users to pick a mode to learn more about it. As a mode is selected, the time-series mode constituent is populated in the zoomed-in view, and the wide-area modal amplitude values are populated in the geographic map display. With the buttons in the lower-right, it is possible to view the damped-sinusoid and pure-exponential components (shown in Figure 4.2 of the signal. The spatial visualization can also play back an animation showing wide-area time evolutions of modal amplitudes. The tool is also capable of displaying state/national boundaries, but they have been excluded from this chapter due to confidentiality reasons associated with the measurement data being used.

This tool was designed so that users could interact with the results and better understand modal analysis by utilizing its spatio-temporal animation capabilities. Space limitations in this chapter prohibit the inclusion of more screenshots; however, the example described in Section 4.5 are supported with graphics generated by this tool, which will further illustrate its spatio-temporal visualization capabilities.

4.4 User Options

This tool is a work-in-progress, and is being improved based on feedback obtained. Despite its minimalistic user-interface, there are several options that users can customize to adapt the tool for their target measurement data. Some of these options are listed in Table 4.1, and are described in this section. As with any analysis involving time-series data, the duration of time-window and the sampling rate are two settings that users may want to modify. These two options are made available in this tool, and users can specify this as a setting for the tool. The window duration can be specified in seconds, and the sampling rate in samples/s. It should be noted that the choice of window duration and sampling rate can have a significant impact on the results and the speed of computation. Some of these issues are discussed in Section 4.6.

Users can also specify a choice of signal to visualize. This is a cosmetic option, and only affects the visualization of results. It has no impact on the underlying DMD algorithm that processes all measurements simultaneously. Similarly, an energy-based threshold can be specified for the reconstruction of the signal. This setting controls the number of modes that are presented, as it may be of practical interest to only see the modes that have a significant contribution to the signal being visualized. The default value of this setting is at 99%, which means that the highest energy modes are selected so that at least 99% of the energy content is captured in the reconstructed signal.

There are two modes available in this tool – (i) streaming mode, and (ii) snapshot mode. If a particular time-window of measurements is to be analyzed, the snapshot mode could be used. However, the streaming mode might be a more convenient option while analyzing a new set of measurements. Users can specify the time-step for the sliding time window, which

Table 4.1: Some user options in the DMD-based modal analysis tool.

#	Options
(i)	Duration of time-window
(ii)	Sampling rate
(iii)	Choice of signal to visualize
(iv)	Energy based threshold for signal reconstruction
(v)	Duration of time-step for sliding window
(vi)	Choice between streaming and snapshot modes
(vii)	Duration of time-horizon for prediction

will control how often the DMD calculation is repeated.

The tool also provides a prediction of the signal being visualized based on the modal content of the current time window. Users may specify a time-horizon for prediction, which will plot the predicted time-series values along with the actual future measurements. Future measurements are available since the analysis is being done in an off-line fashion, and this kind of comparison can help convey the non-linear and time varying aspects of the measurements. It is expected that prediction and future measurements will not match as well as the reconstructed signal in the trailing time-window.

4.5   Example

To illustrate the use of this tool, frequency measurements at 1696 high-voltage locations (a small portion of the total buses in the system, spanning a wide-area, as shown in Figure 4.3) were collected from a transient stability simulation of an industry-grade dynamic model of a large-scale interconnected power grid. A Gaussian load noise model (7% standard deviation) with a low pass filter ($\tau = 0.5$ s) was augmented to all load models to capture the effect of random load fluctuations, and hence introduce noise in the measurements. Transient behavior was recorded for 30 s from a simulation of the loss of a large generation unit at $t = 1$ s. Measurements were gathered at 30 samples/second. Figure 4.4 shows the spread of frequencies at 1696 locations during the fault, with location D highlighted. These measurements were saved in the format described in Section 4.2, and then analyzed with the modal analysis tool.
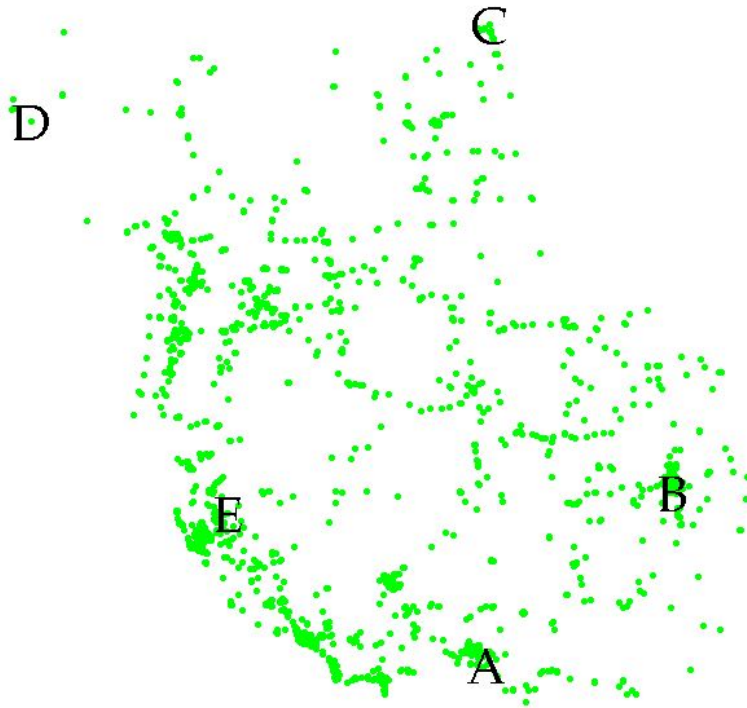
Figure 4.3: Spatial visualization of 1696 measurement locations from an interconnected power grid, with 1 locations labeled.

First, the input data file was loaded, and location D was selected to be visualized. A trailing 5 s sliding time window and a time-step of 0.1 s were specified as user options. This allowed the tool to recompute every 0.1 s,
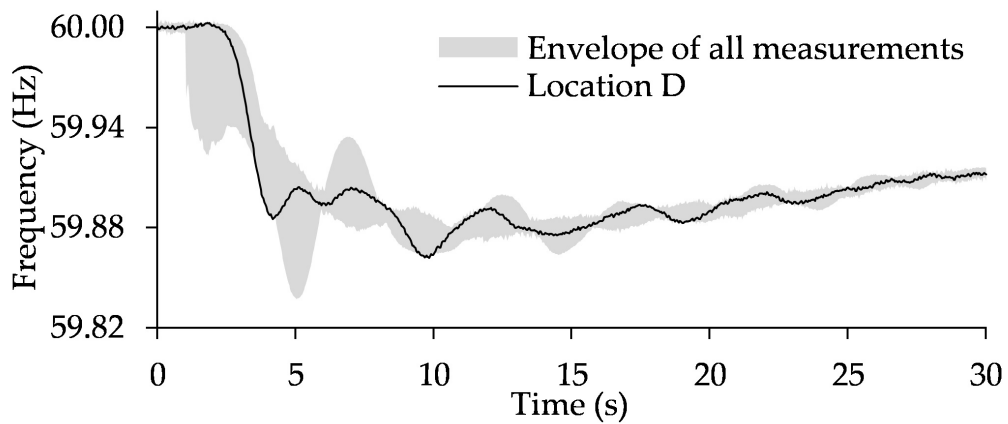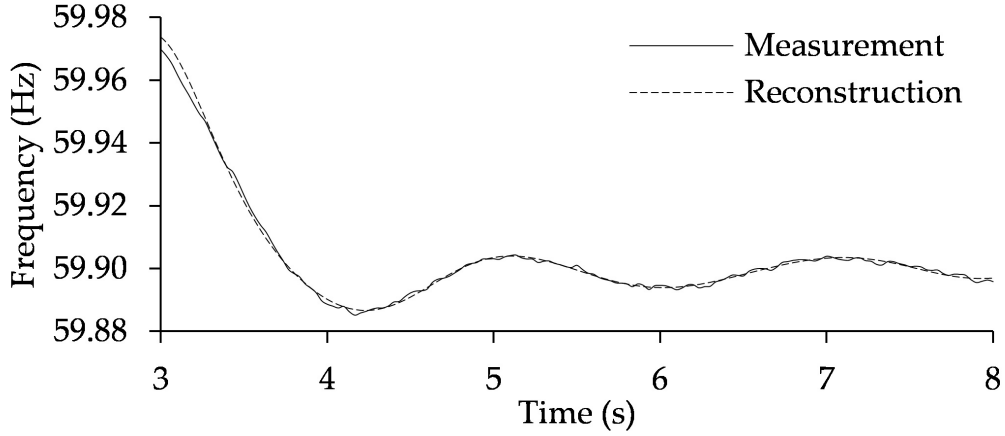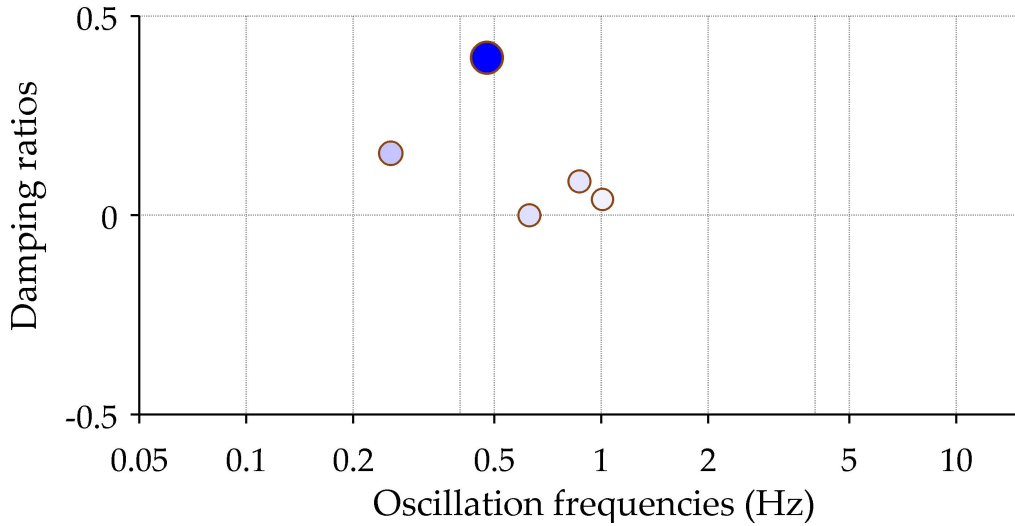

Figure 4.4: Frequency measurements from 1696 locations, with measurement from location D highlighted.

(a) Measured and reconstructed frequency signals.

(b) Plot of damping ratios vs. oscillation frequencies (Hz).

Figure 4.5: Location D, during time-window, $\mathcal{T}_{[3.0,8.0]}$.

while considering 5 s of measurements at a time. As the sliding time-window moved forward in time, the analysis was paused during the trailing time window at 8 s, i.e., $\mathcal{T}_{[3.0,8.0]}$. For each of these time windows, the tool cumulatively performed the modal analysis of all measurements, and then displayed the modal content of the measurement at location D. While using this modal analysis tool, the reconstructed and the measurement signals are both displayed in the zoomed-in view, which is able to visually convey the degree of their similarity. Figure 4.5a shows such an illustration corresponding to the measurement at location D. This reconstruction is based on the modes shown in Figure 4.5b. In the tool, this damping ratio vs. oscillation frequency plot is located in the lower-right section. For each of the modes displayed, users

Table 4.2: Modal analysis of frequency measurement at location D during time-window $\mathcal{T}_{[3.0,8.0]}$.

Modes	Oscillation frequency (Hz)	Damping ratio	Reconstructed time-series values
1	0.47574	0.39543	0.0433
2	0.2552	0.1557	0.0068
3	0.62619	0.000035526	-0.0009
4	0.86687	0.084713	-0.0039
5	1.0067	0.040246	-0.0009

can click on them to display details about them, and also view their time-series representation. For this example, a summary of the constituent modes is presented in Table 4.2. Sparklines show the reconstructed time-series values at the same scale, where negative values are contained within the grey regions.

Users can also view the spatio-temporal variations of the modal amplitudes by first selecting the desired mode and then clicking on the play contours button. The tool will then display an animation showing the evolution of wide-area modal amplitudes. Table 4.3 shows some snapshots from such animation, for the area shown in Figure 4.3. As seen here, the effect of mode 3 is spatially varying, and areas oscillating against one another are easily noticeable. The same information could have been presented with mode shape plots, but the tool presents an animation as a more intuitive alternative. Using such animation, users can drill down into each mode, and also drill across to view its wide-area effects.

Table 4.3: Spatial visualization of mode amplitudes during time-window $\mathcal{T}_{[3.0,8.0]}$ (mode 3 is listed in Table 4.2).

Time	Mode 3
t = 3.0 s	
t = 3.6 s	
t = 4.1 s	

Relative Scale: negative   zero   positive
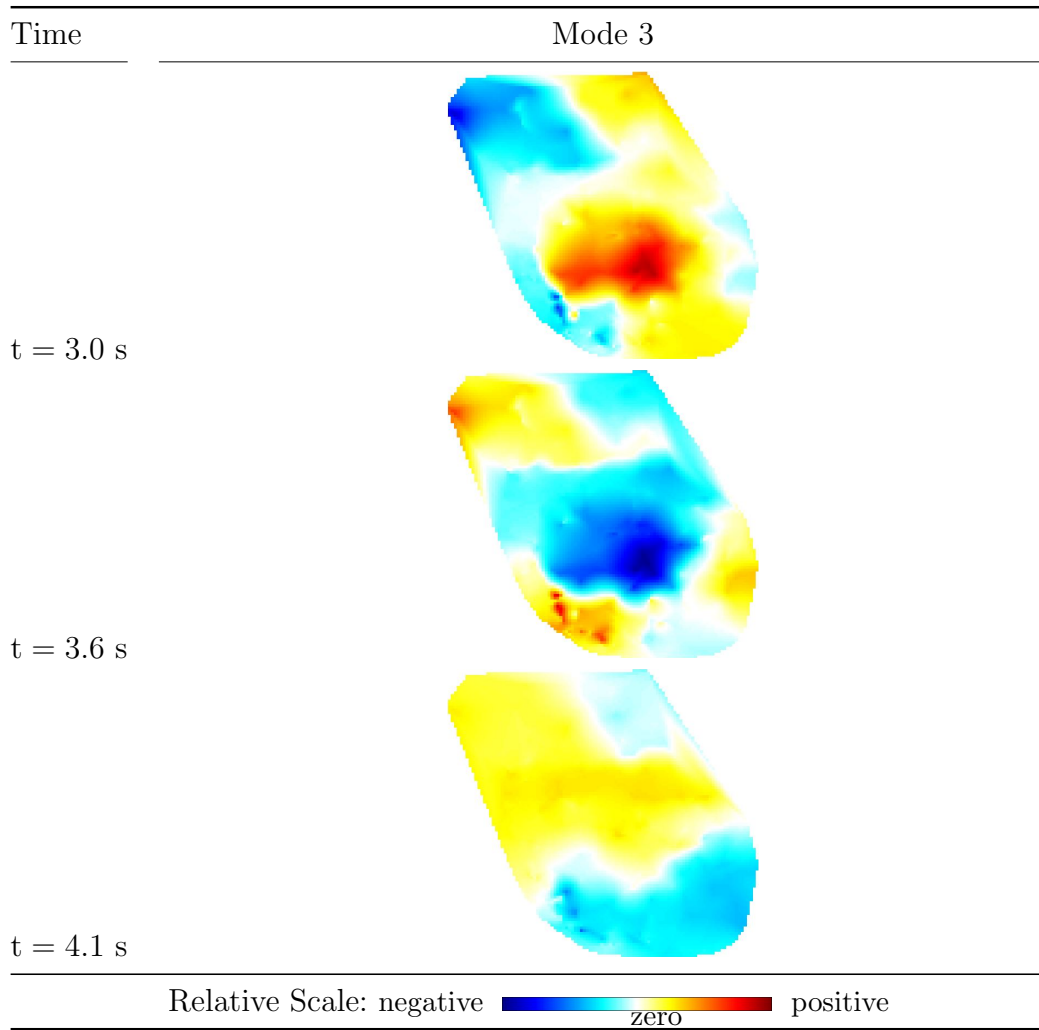
4.6   Performance Tests

As with using any software tool, it is important to know its limitations, as well as have a basic understanding of the input data being analyzed. The modal analysis tool presented in this chapter empirically estimates oscillation frequency, damping ratios, amplitude, and phase, and therefore has some error. The article in [64] provides a more general error analysis for DMD. However in this section, the focus is on understanding the variations in DMD-based modal analysis due to windowing effects and sampling granularity. In addition to these, the computation speed of the tool is also discussed.
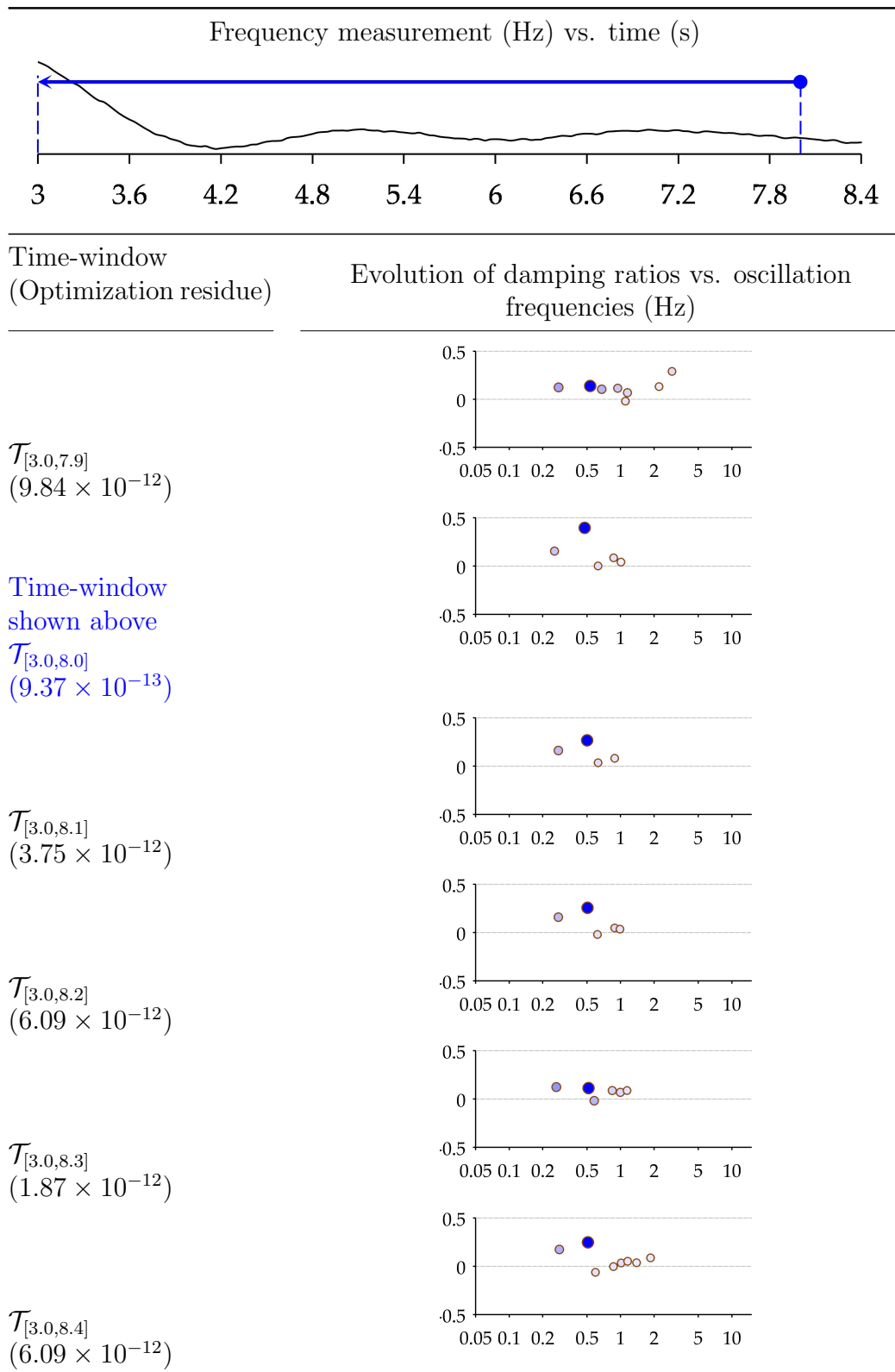
4.6.1   Effect of changing duration of time-window

In the earlier example in Section 4.5, a 5 s time-window was used for DMD, and the modal analysis results were from time window $\mathcal{T}_{[3.0,8.0]}$. The measurement at Location D from the same time-window is shown at the top of Table 4.4. A natural question would be to wonder about the sensitivity of these results to small variations in the length of the time-window selected. As a parametric test, only the end-time of this time window was varied in steps of 0.1 s between 7.9 to 8.4 s. For each window of modal analysis, the respective modal content plots are shown in Table 4.4.

As expected, DMD provides different results for the values of modes and their amplitudes. Although there is seemingly very little difference in the overall signal if the end-time is varied within 7.9 and 8.4 s, it does lead to different results. It should be noted that the DMD algorithm simultaneously optimizes these modes and amplitudes for all the signals being analyzed. Hence, it cannot be directly concluded that the choice of one time-window is better than another. However, it is definitely application specific, and needs to be tuned based on the time-scale of the dynamics being analyzed. The different time-windows also yield different values of optimization residues. These numbers (see Table 4.4) indicate how well all reconstructed signals match the measurements in their respective time-windows. A smaller value symbolizes a better match.

Focusing on the most dominant mode (i.e., the dot with the darkest color), it is interesting to quantitatively observe its sensitivity to the changes in the duration of the time-window. Figure 4.6 shows a plot of the variations in

66

Table 4.4: Sensitivity of estimated damping ratios vs. oscillation frequencies (Hz) of frequency signal measurement at location D (labeled in Figure 4.3) to variations in duration of time-window.
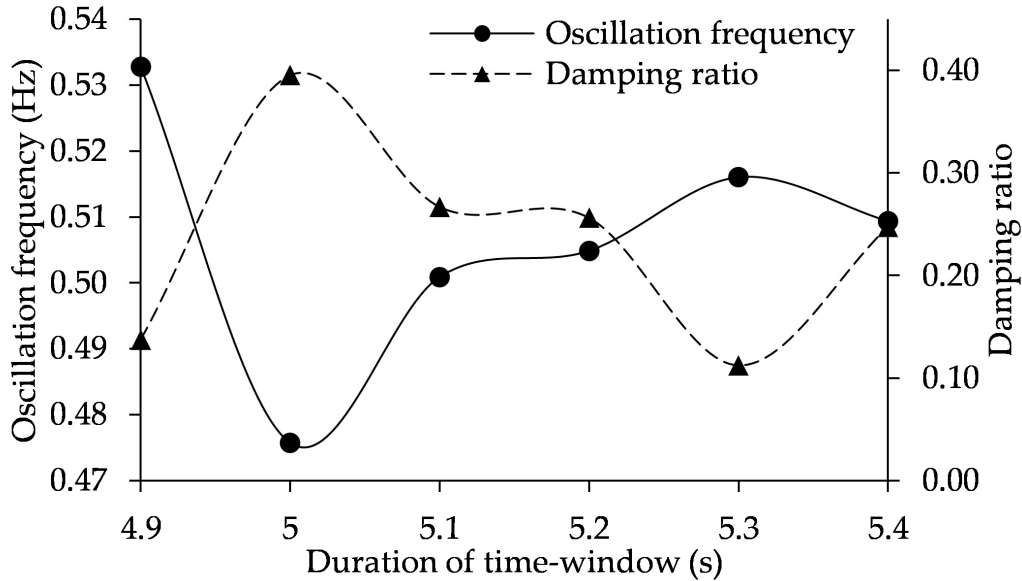

Frequency measurement (Hz) vs. time (s)

Time-window (Optimization residue)	Evolution of damping ratios vs. oscillation frequencies (Hz)
$\mathcal{T}_{[3.0,7.9]}$ (9.84×10^{-12})	
Time-window shown above $\mathcal{T}_{[3.0,8.0]}$ (9.37×10^{-13})	
$\mathcal{T}_{[3.0,8.1]}$ (3.75×10^{-12})	
$\mathcal{T}_{[3.0,8.2]}$ (6.09×10^{-12})	
$\mathcal{T}_{[3.0,8.3]}$ (1.87×10^{-12})	
$\mathcal{T}_{[3.0,8.4]}$ (6.09×10^{-12})	

Figure 4.6: Estimation of oscillation frequency and damping ratio of the dominant mode, with respect to variations in duration of time window, but with a fixed sampling interval of 1/30 s.

the oscillation frequency and the damping ratio. The variation in oscillation frequency is observed to be about 0.06 Hz. In contrast, the variation in damping ratio is about 0.30.

It is also interesting to observe the shape of the plot shown in Figure 4.6. The variations in oscillation frequency and damping ratio seem to be opposite of each other, indicating an underlying trade-off in the estimation of these two quantities.

4.6.2   Effect of changing sampling rate

The sampling rate of a set of measurements determines the range of oscillation frequencies that can be observed in the data. The work in [69] discusses sampling adequacy issues in Prony analysis of power system measurements. Inspired by this work, the effect of variations in sampling rate in DMD is explored. For this parametric analysis, time window $\mathcal{T}_{[3.0,8.0]}$ is chosen, and the sampling rate of input measurements is varied.

As expected, the DMD analysis resulted in different mode values (similar to plots in Table 4.4). Once again, the movement of the dominant mode was tracked, and the values are shown in Figure 4.7. The negative correlations in
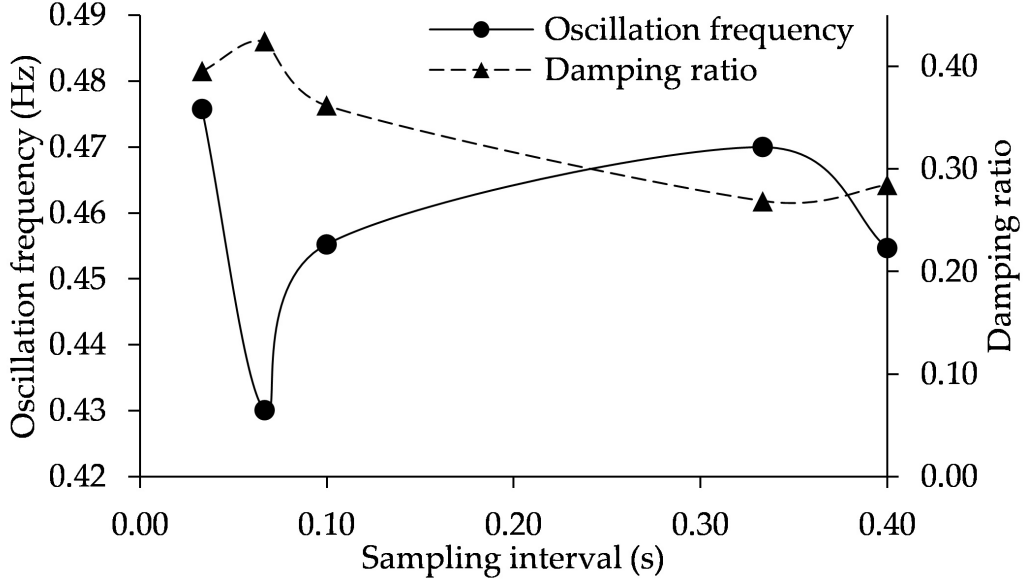
Figure 4.7: Estimation of oscillation frequency and damping ratio of the dominant mode, with respect to variations in sampling interval, but with a fixed time window $\mathcal{T}_{[3.0,8.0]}$.

the relative movements of oscillation frequency and damping ratio are also observed here. However, in contrast to the fluctuation in Figure 4.6, the variation of damping ratio in Figure 4.7 is within a narrower range of about 0.12.

With this brief analysis using this particular measurement set, it is apparent that there are certain trade-offs in using different lengths of time-window and down-sampling. Users are encouraged to experiment and choose options that are best suited for the measurement data. Regardless of the choices in window length and sampling rate, DMD is able to give very small optimization residues between the measurement and reconstructed signals.

4.6.3 Computation speed

The work in both [27] and [65] shows that the DMD algorithm is significantly faster than methods such as Prony. In this tool, modal analysis can be performed fairly quickly, and can be done repeatedly using a sliding time-window approach. For a 6 s time window of 1696 measurements sampled at 30 samples/s, the tool takes about 0.2 s to calculate and visualize the reconstruction on a 2.7 GHz dual core processor. The DMD calculation

takes 0.1 s out of the 0.2 s stated above. Tests showed that the computation duration varies cubicly with the number of samples and linearly with the number of measurements. The tool has also been able to perform well with larger time-windows and more measurements.

4.7 Summary

In contrast to the commercial tools that utilize methods like Prony, Matrix Pencil and Variable Projection, the tool presented in this chapter utilizes DMD, which is a fairly new algorithm, and has only very recently appeared in power systems academic research papers. The key advantage of this tool is its relatively fast computation. Nevertheless, this DMD-based tool is a work-in-progress and has room for improvement. The current version of the tool provides users with a few options that allow some flexibility in the desired analysis; however, users are advised to exercise caution in interpreting the results. Future versions of this tool are expected to incorporate more settings to allow users to concurrently analyze different quantities such as voltages, angles and frequencies. It is also expected that more options will be added to enhance the spatio-temporal visualization capabilities of this tool.

CHAPTER 5

MIXED-MULTI-SIGNAL DMD

In Chapters 3 and 4, only one type of data, i.e., frequency, was used to illustrate the concept of DMD, especially in relation to the spatio-temporal aspects. In practice, there are a variety of measurement types that are gathered from all parts of interconnected power systems. These could be voltage angles, voltage magnitudes, line flows, generator outputs, etc. These data types could also be used in an ensemble manner in a DMD algorithm. Depending on the area of coverage of these other measurement channels, it may also be possible to generate contour plots for them as well. Nevertheless, the idea is to utilize all (or as many as possible) available measurement channels as it will help in mutually enhancing the results, and simultaneously process a large set of channels. This chapter focuses on utilizing voltage magnitude and frequency data simultaneously. It also goes on to present analyses based on DMD, which can be augmented with transient stability analyses.

5.1 Augmenting Frequency Measurements with Voltage Magnitude Measurements

An important conclusion in [64] is that the error in DMD is significantly attributed to the form, quality, and quantity of the input data. One of the suggested approaches is to incorporate as many measurement channels as possible, which helps for datasets with poorer signal-to-noise ratios. Prior work in fluid dynamics has also concluded that measurement locations need to be widely distributed throughout the system of interest [26], and even better if they collectively capture the full phase cycle of the modal constituents [64]. In an attempt to improve the time-varying precision of DMD results, the effects of (i) augmenting datasets, (ii) using longer time-windows, and (ii) down-sampling are studied in this section. Specifically, the impact on the

dominant ac mode is illustrated.

With reference to DAE models for transient stability analysis, and participation factor analysis [28], voltage magnitude and frequency quantities could be thought of as different outputs of the same underlying dynamic system. Hence, time-series voltage magnitude and frequency signals are expected to contain the same modal constituents, but with different coefficients. In other words, during a transient contingency, voltage magnitude and frequency readings at the same location may not exhibit much similarity in their time-domain trend, but still contain varying amounts of the same modal content. This is illustrated in Figure 5.1, which shows the voltage magnitude and frequency readings at location A, during the same transient contingency described in Section 3.4.1.

In an attempt to enhance DMD results, the frequency signals from Section 3.4 are augmented with voltage magnitude signals gathered from the same transient contingency as the earlier section, at 30 samples/s. Using the same software code, the DMD analysis is repeated. This time the input data consists of 3392 measurement channels, with a trailing time-window of $T = 6$ s, and $t_{\text{step}} = \frac{1}{30}$ s. Once again, these are user-defined. The choice of $t_{\text{step}} = \frac{1}{30}$ s is the smallest possible value, and is intentional so that variation in the dominant ac mode can be studied.

For the frequency signal at location A, Figure 5.2 shows the variation of the dominant ac mode with time, i.e., the points at $t = 10.2$ s are calculated based on a trailing time window $\mathcal{T}_{[4.2,10.2]}$. Since $t_{\text{step}} = \frac{1}{30}$ s, there are 31 data
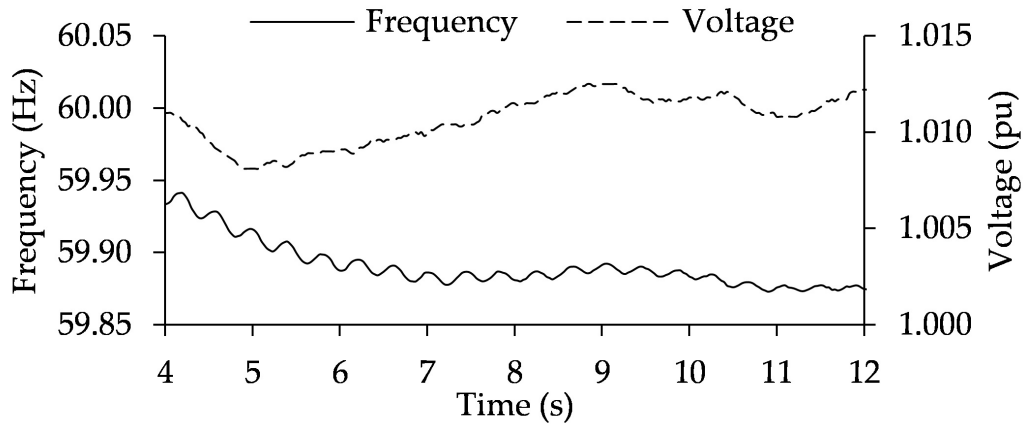

Figure 5.1: Frequency and voltage magnitude channels at Location A, between 4 and 12 s.

points in this plot. This can be compared to the dominant ac mode in Table 3.4, which is seen to vary between 0.17-0.23 Hz. By augmenting frequency with voltage magnitude readings, the dominant mode is now contained in a narrower band with a standard deviation of 0.0137 Hz. Similarly, the damping ratios are also contained within a narrower band. This improvement in precision is practically more useful. In the case of the dominant mode, it was relatively easy to track visually, or a nearest-neighbor type of algorithm could be implemented for automated tracking. However, it has been observed that some eigenvalues bifurcate and rejoin as the system passes through its dynamic trajectory. Nevertheless, the variation in modes is smoothed out.

In Section 3.4, 1696 measurement channels with 181 time points were processed in about 0.105 s. Upon the inclusion of voltage magnitude measurements along with frequency, 3392 measurement channels with 181 time points were processed in about 0.137 s. The incremental computation time was only 0.032 s.

If a 7 second time-window had been used, i.e., 1696 measurement channels with 211 time points, it would be processed in about 0.144 s. This would have incrementally cost 0.039 s extra, which is about the same CPU time as doubling the number of measurement channels. This goes to show that if extra measurement channels are available, then they should be included, especially in the case of augmenting frequency with voltage magnitude data,
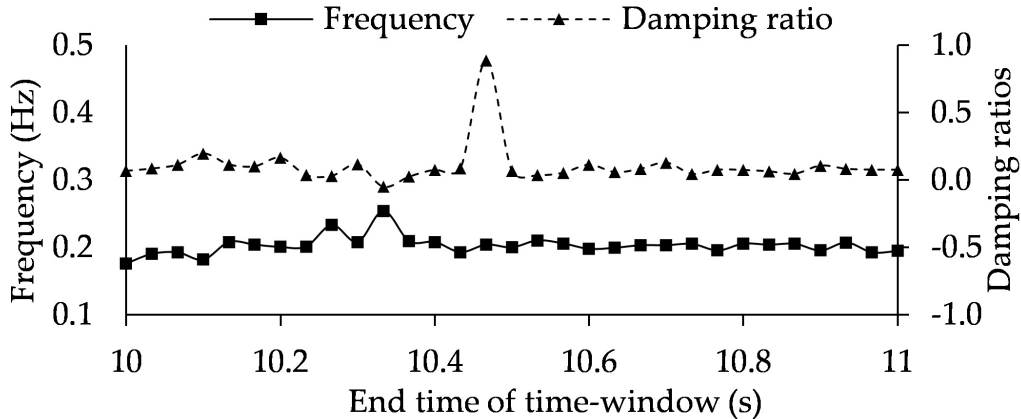

Figure 5.2: Variation in oscillation frequency and damping ratio of the dominant ac mode, using a trailing time window, $T = 6$ s, and $t_{step} = \frac{1}{30}$ s, and input data at 30 samples/s.
Standard deviation of oscillation frequency: 0.0137 Hz.
Standard deviation of damping ratio: 0.152.

73

as it provides a different "view" of the systems dynamic behavior. Ultimately, it helps with improving the precision of results, without needing a longer time-window. Hence, precision of shorter time-interval modal estimation is improved.

As seen in Figure 5.2, there were some spikes observed in the variation of frequency and damping ratios. Hence the effect of using a longer time-window and down-sampling is studied in the following sections.

5.2 Using a Longer Time-Window

Figure 5.3 shows the variation of the dominant ac mode with time, i.e., the points at $t = 11.2$ s are calculated based on a trailing time window $\mathcal{T}_{[4.2,11.2]}$. Since $t_{\text{step}} = \frac{1}{30}$ s, once again there are 31 data points in this plot. This can be compared to the dominant ac mode in Figure 5.2. By using a longer time-window, the frequency variation of the dominant mode is contained in an even narrower band with a standard deviation of 0.00764 Hz. Similarly, the standard deviation of the damping ratios decreased from 0.152 to 0.0324. It should be noted that the mode value variations in time-domain are less responsive to sudden changes, which may or may not be desired, depending on the application.
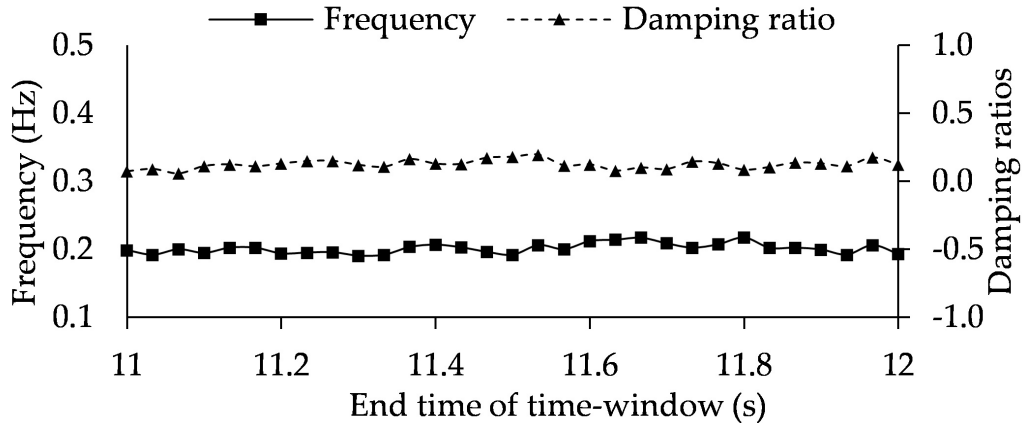

Figure 5.3: Variation in oscillation frequency and damping ratio of the dominant ac mode, using a trailing time window, $T = 7$ s, and $t_{\text{step}} = \frac{1}{30}$ s, and input data at 30 samples/s.
Standard deviation of oscillation frequency: 0.00764 Hz.
Standard deviation of damping ratio: 0.0324.

The computational cost of processing 3392 measurement channels with 211 time points was about 0.185 s. In comparison to the analysis in Figure 5.2, this helped in smoothing out some variations, but came at an incremental cost of $0.185 - 0.137 = 0.048$ s.

5.3   Effects of Down-Sampling

Next, the effect of down-sampling is studied using the same setup as those in Figures 5.2 and 5.3, but using data at 15 samples/s instead of 30 samples/s. In general, down-sampling may not be advised in all situations, especially if higher-frequency oscillations are of interest. However, in the case of wide-area power system electromechanical oscillations, most of the frequency-domain content should be in the lower frequency range [20], and hence down-sampling is a feasible option. In this section, data at 15 samples/s translates to frequency-domain range of $0 - 7.5$ Hz, based on the Nyquist-Shannon sampling criterion [61].

Figures 5.4 and 5.5, are the counterparts of Figures 5.2 and 5.3, respectively. In both cases, the effect of down-sampling is significant in terms of reducing the standard deviation of oscillation frequency and damping ratio of the dominant ac mode. With a 6 second time-window, the smoothing
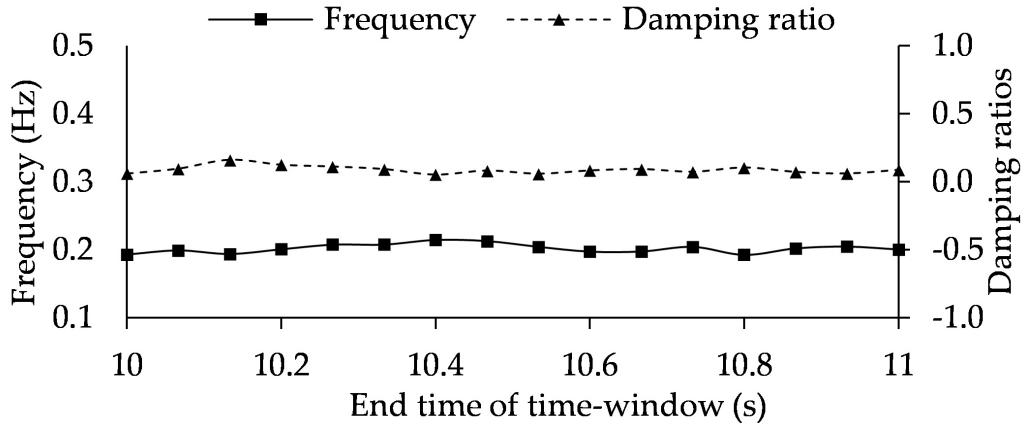

Figure 5.4: Variation in oscillation frequency and damping ratio of the dominant ac mode, using a trailing time window, $T = 6$ s, and $t_{\text{step}} = \frac{1}{15}$ s, and input data at 15 samples/s.
Standard deviation of oscillation frequency: 0.00656 Hz.
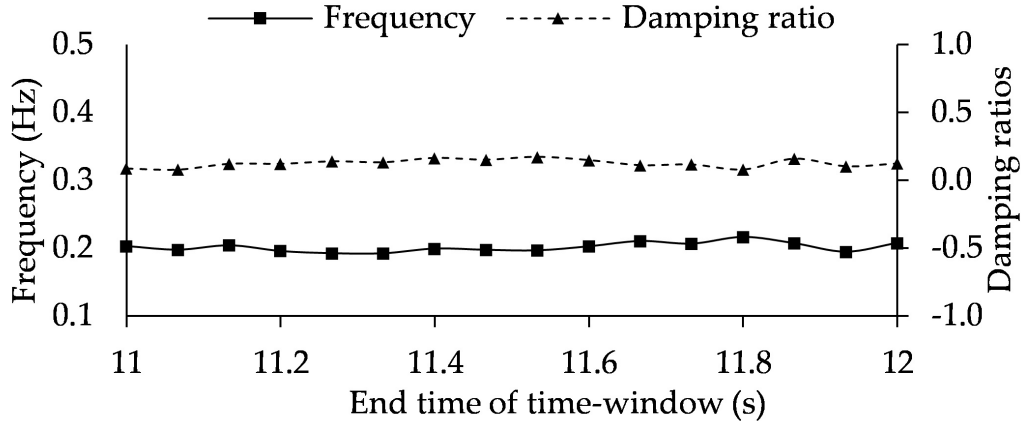Standard deviation of damping ratio: 0.0280.

75

Figure 5.5: Variation in oscillation frequency and damping ratio of the dominant ac mode, using a trailing time window, $T = 7$ s, and $t_{\text{step}} = \frac{1}{15}$ s, and input data at 15 samples/s.
Standard deviation of oscillation frequency: 0.00682 Hz.
Standard deviation of damping ratio: 0.0286.

effect of the dominant ac mode is more apparent after down-sampling, i.e., and order of magnitude less standard deviation. In the case of a 7 second time-window, down-sampling helps in smoothing variations but within the same order of magnitude.

For the down-sampled DMD calculations, 3392 measurement channels with 91 time points (6 second time-window) were processed in about 0.0358 s, and 3392 measurement channels with 106 time points (7 second time-window) were processed in about 0.0473 s. Recall that their 30 samples/s counterpart analyses took about 0.137 s and 0.185 s per time-window. In specific applications, such as the study of inter-area oscillations, it may be possible to down-sample data, without compromising on the accuracy of DMD analyses. Furthermore, the advantage of using less CPU time can help speed up modal estimation of archived data, or even real-time data.

5.4   Discussion

DMD has shown good capability in being able to accommodate a large number of measurement channels. The incremental cost of adding a measurement channel is significantly lower ($\mathcal{O}(M)$) than adding an extra time point ($\mathcal{O}(N^3)$). This is even true when $M \gg N$. Figure 5.6 shows a plot of this
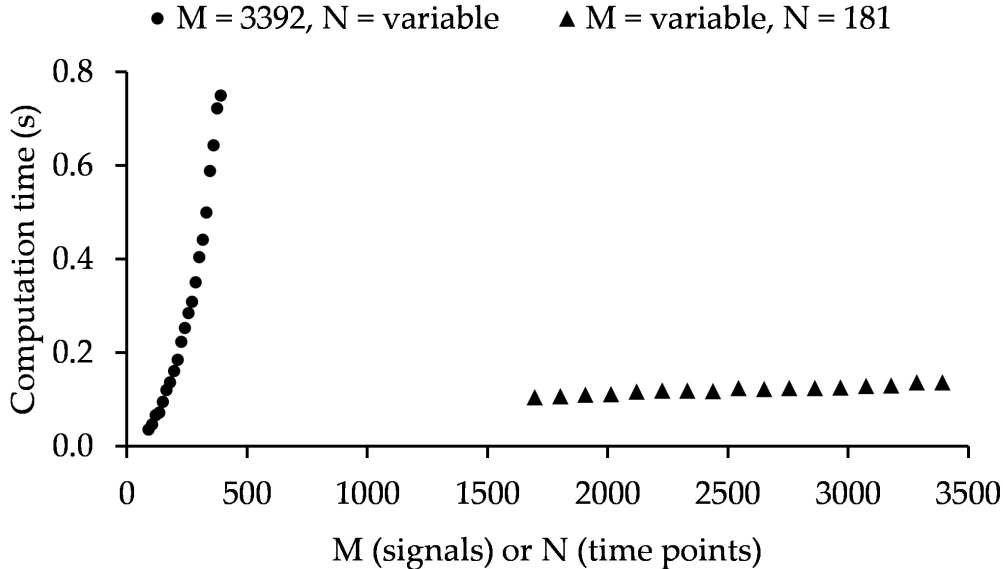
Figure 5.6: Computation times using a 2.7 GHz CPU vs. variations in number of signals, M, and number of time points, N.

trend. The studies in Section 3.4 and this chapter show the improvement in tracking of the dominant oscillation mode during the transient contingency, when voltage magnitude data was augmented with frequency data. Furthermore, the effects of choosing a different time-window and down-sampling have been studied, along with explanations on the impact on precision, time-averaging, and frequency-domain content. There are trade-offs associated, as elaborated earlier.

DMD is inherently an ensemble analysis method, and it is computationally cheap to incorporate a large number of measurement channels. On the other hand, using a subset of the measurement channels, which are pre-selected based on historical information or heuristics, fast modal estimation might be possible by using methods such as Prony, MPM, or ERA. However, using many measurement channels helps with noisy data, and also mitigates data quality issues (as shown in Sections 3.4, this chapter, and [64]). If one of many signals being used is "bad," then the effect on modal estimation would be minimal, as opposed to if data is corrupted in one of a few measurement channels being used. Another reason for using multiple signals is to be able to process them in parallel and detect instability in a small number of signals during their initial unstable growth.

As stated in [64], having measurement channels that capture a full phase

cycle is helpful for DMD's performance. In this chapter, augmenting frequency with voltage magnitude signals did help in reducing the rapid change in modal constituents. Using a longer time window could have also helped in averaging out the modes and reducing the fluctuations. An example of this is the work in [27], which utilized time-windows of about $20-40$ seconds. So instead of using longer time-windows, multiple measurement channels of different data types should be used in DMD analyses, if they are available. The result is better precision, even though a smaller time-window is used (Figure 5.2), and fast modal estimation. By using a smaller time-window, the time-varying estimates of a dominant mode are less influenced by averaging over a longer time-window. Also, using multiple channels can help maintain the quality of modal estimates; therefore, using smaller time-windows would be sufficient.

In all North American interconnections, PMUs and PMU-like devices are being installed in large numbers, and communication pipelines are being commissioned to collect and store this data. Since the computational cost associated with DMD is low, it may be of interest to process multiple channels of measurements at data concentrator locations or control centers, and then broadcast holistic measures such as oscillation frequencies, damping ratios, and respective amplitudes. In this way, the circulation of raw measurement data would be reduced, and wide-area closed loop control schemes could be designed by incorporating the above-mentioned holistic metrics.

As an example, DMD is able to process 3392 measurement channels with 181 time points in 0.137 s. This implies that DMD can be repeated with new time points as soon as the previous DMD calculation is completed. Once a particular time-window of measurement channels has been gathered at a data concentrator, the algorithmic latency of a moving window DMD analysis would be 0.137 s.

There are other on-line tools which automatically calculate and monitor the modal content of a collection of power system measurements. DMD is hoped to be a good addition to the list of such tools, and to be especially useful for the simultaneous analysis of thousands of measurement channels. DMD might also prove useful in the case of a series of transient contingencies, or possibly a cascading failure scenario. Since the "ring-down" time interval will be relatively short for each consecutive fault, DMD would be able to accommodate short-time interval data (from many channels), and still give

good modal estimates in a reasonable computation time. This could be utilized in alarm processing, i.e., to create a new category of modal content alarms for alerting operators of undesired dynamic conditions. Hence, multiple measurements can be automatically processed in real-time, and operator attention would only be required when any desired criterion is being violated.

## 5.5 Spatio-Temporal Results from Frequency and Voltage Magnitude Data

So far the discussion in this chapter was on the dominant oscillation mode in the entire system. However during dynamic behavior, the dominant mode in one part of the system might differ from another location in the same system. In other words, the amplitude (or the energy content) of a particular mode can vary based on the location, the fault, and the operating point. Therefore, for the voltage magnitude and frequency data used in the earlier sections of this chapter, the collection of dominant modes is shown in Table 5.1. This is for the time-window of $\mathcal{T}_{[4.0,11.0]}$. The input data sampling rate is at 30 samples/s. Even though the same set of simulated transient contingency data is used, it should be noted that the estimates of modes are different from earlier chapters. This is because the time-window used is different, and also the fact that frequency data has been augmented with voltage magnitude data. As discussed in the previous sections of this chapter, one of the benefits observed is the consistency (or precision) of the modes in a sliding time-window analysis. In this particular time-window, modes 1 and 2 have low damping ratios, while the damping ratio for mode 3 is significantly greater. Hence, mode 3 can be considered to be well damped.

Since both frequency and voltage magnitude data have been utilized for

Table 5.1: Modal analysis of frequency and voltage magnitude measurements during time-window $\mathcal{T}_{[4.0,11.0]}$.

Modes	Oscillation frequency (Hz)	Damping ratio
1	0.19886	0.074679
2	0.31007	0.027697
3	0.40178	0.46923

Table 5.2: Spatial visualization of mode amplitudes during time-window $\mathcal{T}_{[4.0,11.0]}$ (modes 1 and 2 are listed in Table 5.1).
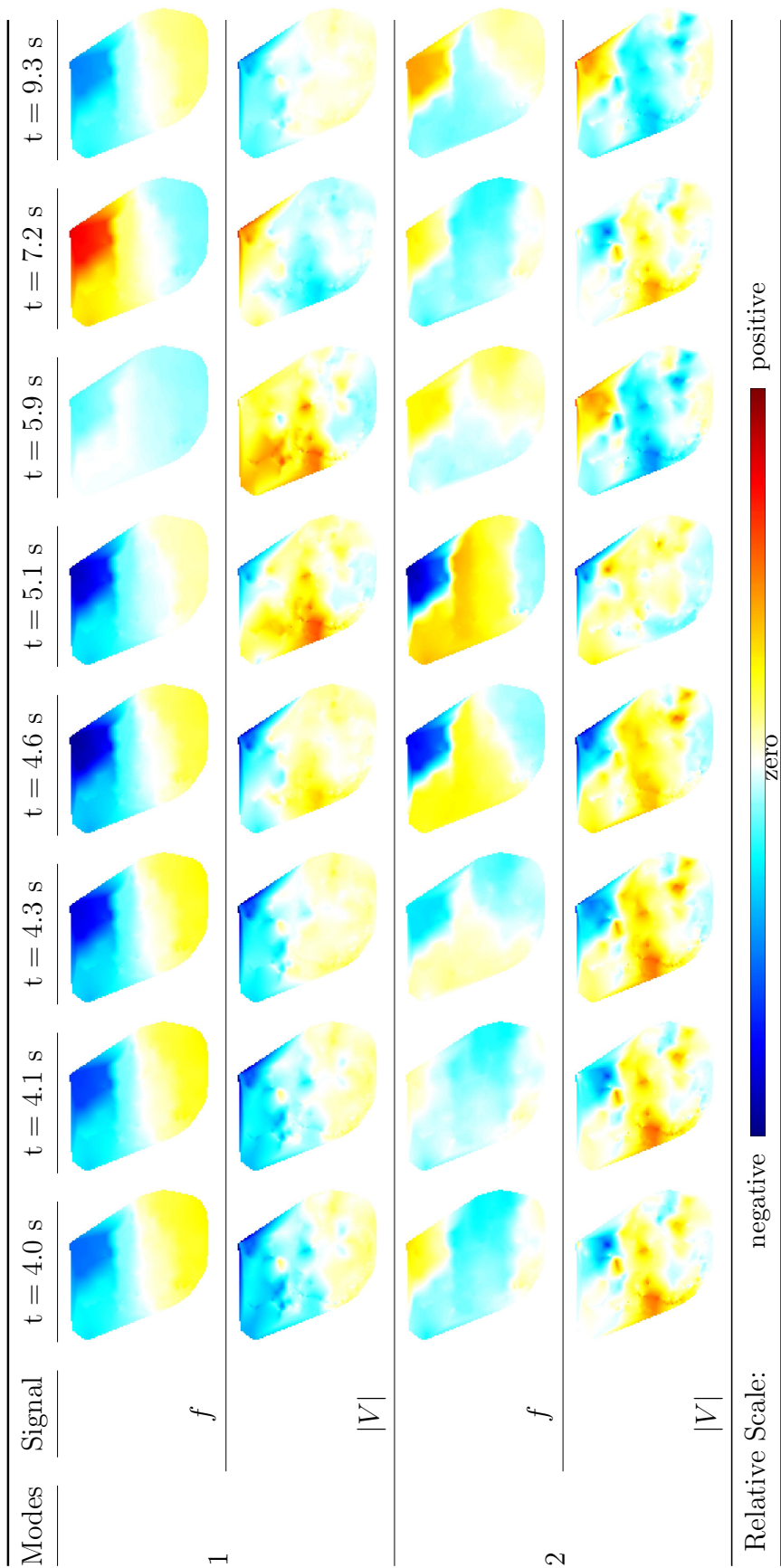
the analysis in this chapter, each location is associated with two types of signals. From a geographic viewpoint, one could imagine two layers of data associated with the footprint of the system being studied. Modal estimation with DMD is done simultaneously for all these signals, which expresses each layer of measurement data as a location-wise sum of several modes. If there are R modes, then that would correspond to R sub-layers for each layer of measurement data. Figure 5.2 shows the temporal evolution of two such sub-layers, which corresponds to modes 1 and 2 from Table 5.1. The contours shown correspond to the geographic area of the large-scale system.

The series of snapshots shown in Figure 5.2 is from an animation of the mode amplitudes during time-window $\mathcal{T}_{[4.0,11.0]}$. As seen here, the spatio-temporal variation of each mode can be observed. The animation of the frequency layers for both modes is similar to those in Figure 3.3. The spatial variation of mode amplitudes is gradual in the frequency layer. From a system-level view, there is a phase difference between the two modes, and this is expected due to the presence of many dynamic components in the system. The contour animations associated with the voltage magnitude layer are more interesting, as they exhibit the inter-area manifestation of modes, but also show localized effects. The spatial variation in modes is more pronounced in the voltage layer, which ties in well with the idea that voltage dynamics are often in localized clusters.

From the perspective of the frequency layer, mode 1 is seen to divide the system into two areas, and mode 2 divides the system into 3 areas. These are usually known as inter-area modes. However for each of these modes, the corresponding voltage layer exhibits different spatial areas. So if an inter-area mode is observed between a particular set of areas in the frequency layer, the areas observed in the voltage layer can be different. This indicates that the amplitude and the phase of a particular mode can be different between the frequency and voltage magnitude signals measured at the same location.

As discussed in Chapter 3, the animation of modes can be useful for wide-area visualization. In this section, the voltage magnitude and frequency layers can be studied similarly, but two sets of animation are needed to capture the spatio-temporal effect of each mode. These animations could be viewed independently for each layer, or side-by-side, to understand the combined effect of each mode on both layers of measurement data.

In addition to the spatio-temporal animation of each mode, the phase of

Table 5.3: Contours of phase of voltage magnitude w.r.t. frequency, visualized per mode (modes 1 and 2 are listed in Table 5.1).

Mode 1	Mode 2

Scale: −180°　0°　180°
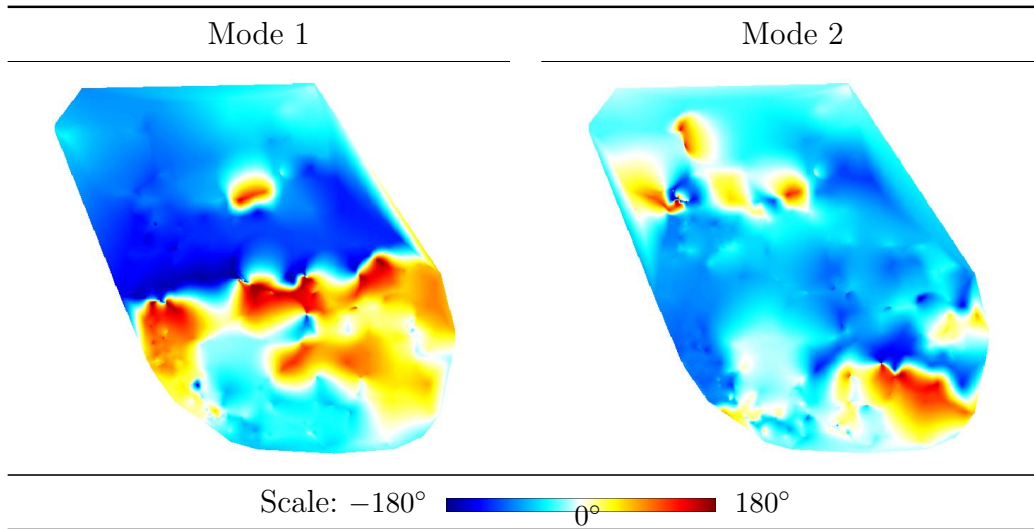
the voltage magnitude w.r.t. to the frequency for each mode is shown in Table 5.3. The contours here represent a value in degrees. The yellow-red areas are regions where modal oscillations in voltage magnitude are leading their frequency counterparts, and the turquoise-blue areas show lagging regions. It is interesting to observe that this phase difference in mode 1 shows a contour that exhibits some kind of a system-level behavior. A similar contour is also observed in the case of mode 2. The significance of this phase difference seems to be unexplored in power system literature. At each location, the phase difference signifies that the ac voltage waveform amplitude is compressed the greatest at a slightly different point in time w.r.t to the maximum compression of its period. However, further research is required to understand the significance of the relation of this phase difference across locations.

The analysis showed the use of voltage magnitude and frequency data in an ensemble manner. However, this framework is extensible to any type of measurement from an interconnected power system. If the same type of measurement is available from several locations, then spatio-temporal visualization can be created for those layers of measurement data as well. Even if there are just a few measurements of a particular type, they should still be utilized in an ensemble manner to enhance the results of DMD. An example of this could be real power flow across major transmission lines.

5.6 Effect of Varying Inter-Area Real Power Transaction

It is known that the modes observed during a transient contingency are a function of the operating point of the system. From a system-level perspective, the pre-fault real power transactions between balancing authorities could be thought of as an indicator of a particular operating point. In this section, the operating point of the large-scale system used earlier is systematically varied by adjusting the real power transactions between two geographically distant areas. The two areas considered in this case were located in the Northwest (NW) and the Southwest(SW) regions of the system. There was a 4632 MW transaction that was present in the base case operating point, from NW to SW. This value was decreased at 100 MW decrements, and also increased at 100 MW increments. For each of those operating points the same transient contingency was simulated, i.e., the loss of a large generation unit in the southern part of the system. From each of the transient contingencies, voltage magnitude and frequency data were gathered and a DMD analysis was carried out for the time-window $\mathcal{T}_{[4.0,11.0]}$ with data at 30 samples/s. The aim was to observe the resulting variation in the $\sim$ 0.2 Hz and $\sim$ 0.3 Hz modes of the system.

Figures 5.7 and 5.8 show the variation in modes as the transaction between NW and SW is varied. The transaction value has an effect on both the oscillation frequency and damping ratio of modes. With respect to the original
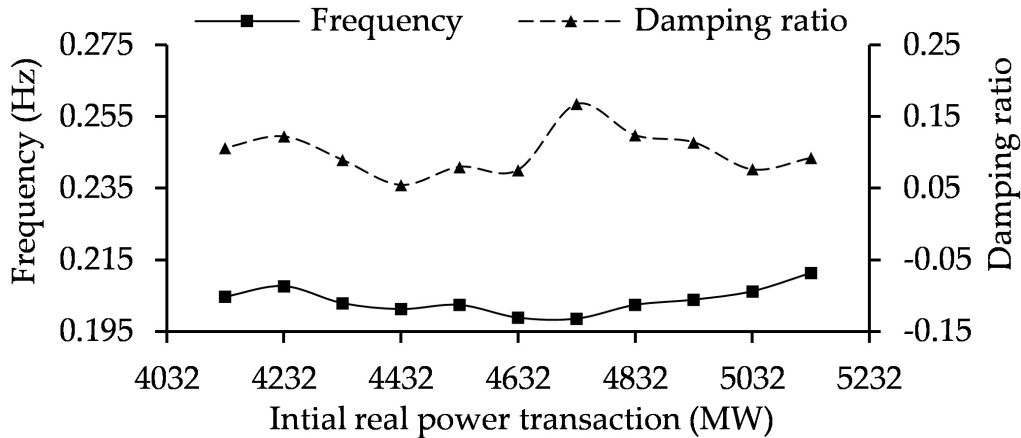

Figure 5.7: Variation in oscillation frequency and damping ratio of the mode around $\sim$ 0.2 Hz , w.r.t. initial real power transaction.
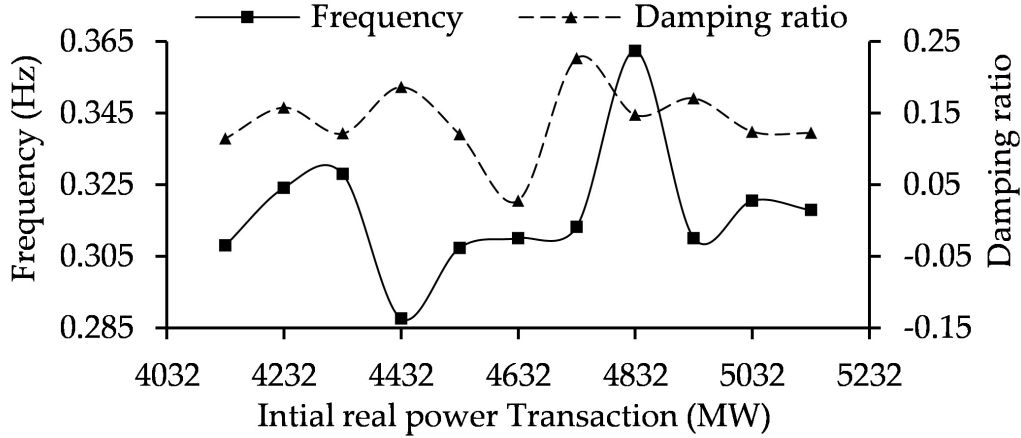
83

Figure 5.8: Variation in oscillation frequency and damping ratio of the mode around ~ 0.3 Hz , w.r.t. initial real power transaction.

transaction of 4632 MW, the transaction of 4132 MW (and some others) leads to better damping ratios of both the modes. However, the variation is not linear. From a transient stability analysis perspective, such analyses could be done to understand the effect of operating points on dynamic behavior. In a planning scenario where different operating points might be tested for their transient stability response, DMD can be used to better understand the evolution of modes w.r.t operating points. Since the DMD computation time would be on the order of a second, compared to the transient stability simulation on the order of minutes, the incremental computational burden would be minimal.

5.7   Effect of Using a Different Transient Contingency, But of Similar Intensity

For consistency reasons, the same transient contingency was utilized for the simulated measurements in prior sections. To recap, the fault applied was the loss of a large generation unit in the southern part of the system. Let this be contingency X. As per the locations labeled in Figure 3.1, location C is situated in the northeast part of the system. In this location the frequency signal during contingency X consisted of 3 modes as shown in Figure 5.9. The circles show the position of the modes, and the color intensity shows the relative energy content of each mode, in the time-window of analysis.
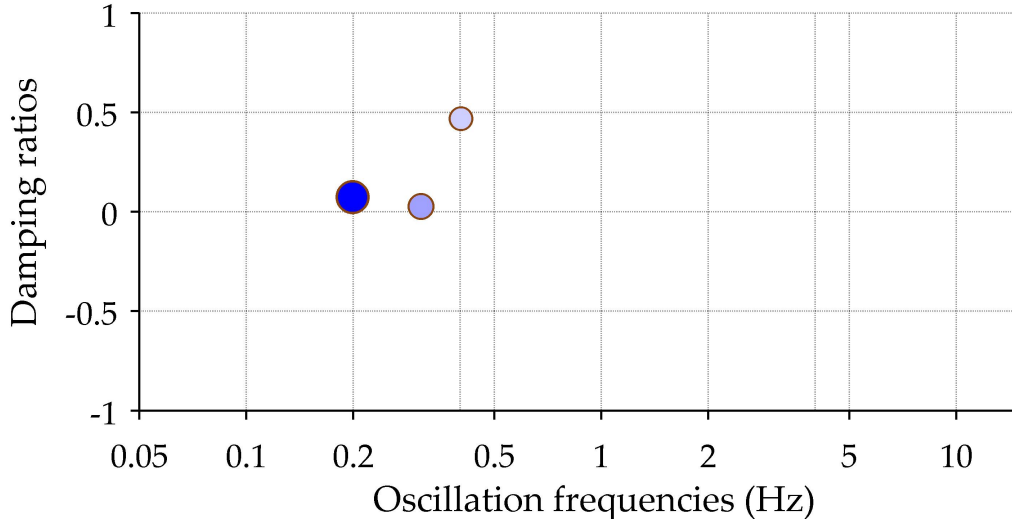
Figure 5.9: Plot of damping ratios vs. oscillation frequencies (Hz) at Location C (frequency signal), during time-window, $\mathcal{T}_{[4.0,11.0]}$, during transient contingency X.

For a second contingency Y, a generation loss of a very similar size was introduced in the western side of the system. Figure 5.10 shows the modes observed in the frequency signal at location C. In contingency X, the disturbance propagated in the general direction of south to north. In contrast, the disturbance in contingency Y propagated from West to East. For the same
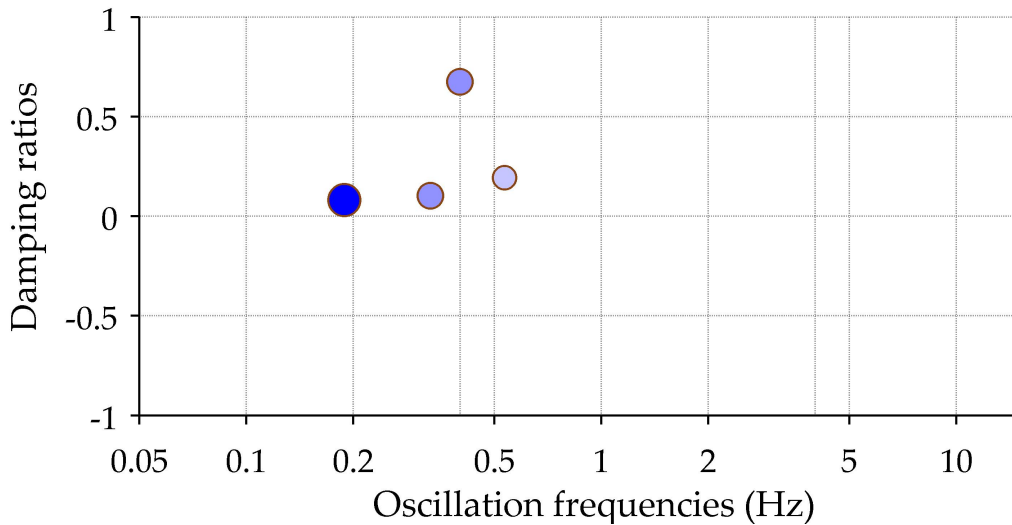

Figure 5.10: Plot of damping ratios vs. oscillation frequencies (Hz) at Location C (frequency signal), during time-window, $\mathcal{T}_{[4.0,11.0]}$, during transient contingency Y.

time-window, the time-domain frequency and voltage signals were significantly different between contingencies X and Y. It is interesting to observe that the modes perturbed at location C were very similar in the case of both contingencies.

As mentioned earlier, the modal estimates calculated by DMD have been obtained without the use of de-trending on the raw data. From a dynamic system theory perspective, the calculated modes could be likened to the modes of the closed-loop system of equations governing the dynamics.

5.8 Comments and Future Work

The work presented in Chapters 3, 4, and 5 is directly applicable to the results of any transient stability simulation. In a planning environment values of frequency, voltage magnitudes, line flows, etc., can be saved for processing with DMD. As mentioned earlier, DMD is efficient in estimating modes, and could significantly enhance transient stability analyses, with minimal extra computation time. Based on the outputs of DMD, several rule-based logic or heuristics could be applied to simultaneously screen thousands of signals. Uses of this screening could be to identify regions with low damping ratios, or to detect unstable oscillation growth. During transient stability analyses a large volume of data can be generated very quickly, especially while studying interconnections and running multiple contingencies. In those situations it is prohibitive to store large-quantities of time-series results. Commercial software packages usually have types of limit-monitoring criteria so that essential information can be selectively saved. The use of DMD along with modal content monitors is expected to provide an efficient method of screening large quantities of data, and to save essential plots and contours as shown in the studies in this chapter.

In an operational environment, modal estimation has been implemented to analyze ambient data from interconnections. However, a survey of existing work has not revealed implementation where the calculated modes have been used for automatic control actions. To inspire this, the use of DMD for real-time modal content monitoring has been presented in Chapter 3, the key benefits being the fast computation time and short-time interval modal estimation. However, to bring modal estimation into a closed-loop control

framework requires future work. The concept of DMDc (DMD with control) [70] can be utilized to further extend DMD analysis. It is expected that the output of DMDc analysis could provide a measurement-driven understanding of the effect of inputs (e.g., generator real power output, or generator terminal voltage) on the outputs (e.g., frequency, voltage magnitudes) of a system. Future work is planned to implement DMDc to enhance understanding between inputs and outputs of large-scale interconnected power systems.

REFERENCES

[1] A. D. Ker, "Quantitative evaluation of pairs and RS steganalysis," in *Electron. Imaging 2004*, E. J. Delp III and P. W. Wong, Eds. International Society for Optics and Photonics, June 2004, pp. 83–97.

[2] N. Johnson and S. Jajodia, "Steganalysis: the investigation of hidden information," in *1998 IEEE Inf. Technol. Conf. Inf. Environ. Futur. (Cat. No.98EX228).* IEEE, 1998, pp. 113–116.

[3] G. Kron, *Tensor Analysis of Networks.* Chapman & Hall, 1939. [Online]. Available: http://books.google.com/books?id=3lNKcgAACAAJ\ &pgis=1

[4] J. B. Ward, "Equivalent circuits for power-flow studies," *Trans. Am. Inst. Electr. Eng.*, vol. 68, no. 1, pp. 373–382, July 1949.

[5] N. Sato and W. Tinney, "Techniques for exploiting the sparsity of the network admittance matrix," *IEEE Trans. Power Appar. Syst.*, vol. 82, no. 69, pp. 944–950, Dec. 1963.

[6] PennEnergy Editorial Staff, "Report urges better cybersecurity for North American electricity grid," 2014. [Online]. Available: http://www.pennenergy.com/articles/pennenergy/2014/03/report-urges-better-cybersecurity-for-u-s-power-systems.html

[7] J. Rommes and N. Martins, "Exploiting structure in large-scale electrical circuit and power system problems," *Linear Algebra Appl.*, vol. 431, no. 3-4, pp. 318–333, July 2009. [Online]. Available: http://www.sciencedirect.com/science/article/pii/S0024379509000184

[8] B. Jiang and I. Omer, "Spatial topology and its structural analysis based on the concept of simplicial complex," *Trans. GIS*, vol. 11, no. 6, pp. 943–960, Dec. 2007.

[9] J. Taber, D. Shawhan, R. Zimmerman, C. Marquet, M. Zhang, W. Schulze, R. Schuler, and S. Whitley, "Mapping energy futures using the SuperOPF planning tool: An integrated engineering, economic and environmental Model," in *2013 46th Hawaii Int. Conf. Syst. Sci.* IEEE, Jan. 2013, pp. 2120–2129.

[10] W. Jang, S. Mohapatra, T. J. Overbye, and H. Zhu, "Line limit preserving power system equivalent," in *2013 IEEE Power Energy Conf. Illinois.* IEEE, Feb. 2013, pp. 206–212.

[11] A. J. Wood and B. F. Wollenberg, *Power Generation, Operation, and Control.* John Wiley & Sons, 2012.

[12] C. Duthaler, M. Emery, G. Andersson, and M. Kurzidem, "Analysis of the Use of Ptdf in the Ucte Transmission Grid," *Power Syst. Comput. Conf.*, 2008.

[13] D. Shi, D. L. Shawhan, N. Li, D. J. Tylavsky, J. T. Taber, R. D. Zimmerman, and W. D. Schulze, "Optimal generation investment planning: Pt. 1: network equivalents," in *2012 North Am. Power Symp.* IEEE, Sep. 2012, pp. 1–6.

[14] P. Dimo, *Nodal Analysis of Power Systems.* Editura Academiei Republicii Socialisté România, 1975.

[15] N. Li, D. Shi, D. L. Shawhan, D. J. Tylavsky, J. T. Taber, R. D. Zimmerman, and W. D. Schulze, "Optimal generation investment planning: Pt. 2: Application to the ERCOT system," in *2012 North Am. Power Symp.* IEEE, Sep. 2012, pp. 1–6.

[16] Transmission Transfer Capability Task Force, "Available Transfer Capability Definitions and Determination," North American Electric Reliability Council, Tech. Rep., 1996.

[17] T. Overbye, D. Hale, T. Leckey, and J. Weber, "Assessment of transmission constraint costs: Northeast US case study," in *2000 IEEE Power Eng. Soc. Winter Meet. Conf. Proc. (Cat. No.00CH37077)*, vol. 2. IEEE, 2000, pp. 903–908.

[18] W. Tinney and J. Walker, "Direct solutions of sparse network equations by optimally ordered triangular factorization," *Proc. IEEE*, vol. 55, no. 11, pp. 1801–1809, 1967.

[19] W. Jang, S. Mohapatra, and T. J. Overbye, "Towards a transmission line limit preserving algorithm for large-scale power system equivalents," in *2015 48th Hawaii Int. Conf. Syst. Sci.*, 2015.

[20] P. Kundur, *Power System Stability and Control.* McGraw-Hill Education, 1994.

[21] J. Hauer, E. Martinez, A. R. Messina, and J. Sanchez-Gasca, "Identification of Electromechanical Modes in Power Systems," Tech. Rep., 2012.

[22] J. Hauer, C. Demeure, and L. Scharf, "Initial results in Prony analysis of power system response signals," *IEEE Trans. Power Syst.*, vol. 5, no. 1, pp. 80–89, 1990.

[23] Y. Hua and T. Sarkar, "Matrix pencil method for estimating parameters of exponentially damped/undamped sinusoids in noise," *IEEE Trans. Acoust.*, vol. 38, no. 5, pp. 814–824, May 1990.

[24] I. Kamwa, R. Grondin, E. Dickinson, and S. Fortin, "A minimal realization approach to reduced-order modelling and modal analysis for power system response signals," *IEEE Trans. Power Syst.*, vol. 8, no. 3, pp. 1020–1029, 1993.

[25] P. Schmid and J. Sesterhenn, "Dynamic mode decomposition of numerical and experimental data," *Bull. Am. Phys. Soc.*, vol. 53, Nov. 2008.

[26] P. J. Schmid, L. Li, M. P. Juniper, and O. Pust, "Applications of the dynamic mode decomposition," *Theor. Comput. Fluid Dyn.*, vol. 25, no. 1-4, pp. 249–259, Aug. 2010.

[27] E. Barocio, B. C. Pal, N. F. Thornhill, and A. R. Messina, "A dynamic mode decomposition framework for global power system oscillation analysis," *IEEE Trans. Power Syst.*, 2014.

[28] G. Rogers, *Power System Oscillations.* Kluwer Academic Publishers, 2000.

[29] A. R. Borden and B. C. Lesieutre, "Variable projection method for power system modal identification," *IEEE Trans. Power Syst.*, vol. 29, no. 6, pp. 2613–2620, Nov. 2014.

[30] N. Zhou, D. Trudnowski, J. W. Pierre, S. Sarawgi, and N. Bhatt, "An algorithm for removing trends from power-system oscillation data," in *2008 IEEE Power Energy Soc. Gen. Meet. - Convers. Deliv. Electr. Energy 21st Century.* IEEE, July 2008, pp. 1–7.

[31] A. R. Borden, B. C. Lesieutre, and J. Gronquist, "Power system modal analysis tool developed for industry use," in *2013 North Am. Power Symp.* IEEE, Sep. 2013, pp. 1–6.

[32] G. Prony, *Multiexponential Fitting Algorithm. Numerical Analysis.* New York: McGraw-Hill, 1974.

[33] V. Jain, "Filter analysis by use of pencil of functions: Part I," *IEEE Trans. Circuits Syst.*, vol. 21, no. 5, pp. 574–579, Sep. 1974.

[34] V. Jain, "Filter analysis by use of pencil of functions: Part II," *IEEE Trans. Circuits Syst.*, vol. 21, no. 5, pp. 580–583, Sep. 1974.

[35] J. N. Juang and R. S. Pappa, "An eigensystem realization algorithm for modal parameter identification and model reduction," *J. Guid. Control. Dyn.*, vol. 8, no. 5, pp. 620–627, Oct. 1985.

[36] G. H. Golub and V. Pereyra, "The differentiation of pseudo-inverses and nonlinear least squares problems whose variables separate," *SIAM J. Numer. Anal.*, vol. 10, no. 2, pp. 413–432, Apr. 1973.

[37] G. Golub and V. Pereyra, "Separable nonlinear least squares: the variable projection method and its applications," *Inverse Probl.*, vol. 19, no. 2, pp. R1–R26, Apr. 2003.

[38] L. L. Scharf and C. Demeure, *Statistical Signal Processing: Detection, Estimation, and Time Series Analysis.* Addison-Wesley Publishing Company, 1991.

[39] Z. Huang, N. Zhou, F. Tuffner, Y. Chen, D. Trudnowski, R. Diao, J. Fuller, W. Mittelstadt, J. Hauer, and J. Dagle, *MANGO: Modal Analysis for Grid Operation: a Method for Damping Improvement Through Operating Point Adjustment.* Pacific Northwest National Laboratory, 2010.

[40] J. Pierre, D. Trudnowski, M. Donnelly, N. Zhou, F. Tuffner, and L. Dosiek, "Overview of system identification for power systems from measured responses," in *Syst. Identif.*, vol. 16, no. 1, July 2012, pp. 989–1000.

[41] J. Pierre, D. Trudnowski, and M. Donnelly, "Initial results in electromechanical mode identification from ambient data," *IEEE Trans. Power Syst.*, vol. 12, no. 3, pp. 1245–1251, 1997.

[42] D. Trudnowski, J. Pierre, and W. Mittelstadt, "Electromechanical mode online estimation using regularized robust RLS methods," *IEEE Trans. Power Syst.*, vol. 23, no. 4, pp. 1670–1680, Nov. 2008.

[43] N. Zhou, J. W. Pierre, and D. Trudnowski, "A stepwise regression method for estimating dominant electromechanical modes," *IEEE Trans. Power Syst.*, vol. 27, no. 2, pp. 1051–1059, May 2012.

[44] L. Dosiek, J. W. Pierre, and J. Follum, "A recursive maximum likelihood estimator for the online estimation of electromechanical modes with error bounds," *IEEE Trans. Power Syst.*, vol. 28, no. 1, pp. 441–451, Feb. 2013.

[45] L. Dosiek and J. W. Pierre, "Estimating electromechanical modes and mode shapes using the multichannel ARMAX model," *IEEE Trans. Power Syst.*, vol. 28, no. 2, pp. 1950–1959, May 2013.

[46] Z. Tashman and V. M. Venkatasubramanian, "Modal energy trending for ringdown analysis in power systems using synchrophasors," in *2014 47th Hawaii Int. Conf. Syst. Sci.* IEEE, Jan. 2014, pp. 2475–2482.

[47] E. Rezaei, L. Zhang, and V. Venkatasubramanian, "Self-correction strategies for frequency domain ringdown analysis," in *2015 48th Hawaii Int. Conf. Syst. Sci.* IEEE, 2015, pp. 2690–2699.

[48] J. H. Tu, C. W. Rowley, D. M. Luchtenburg, S. L. Brunton, and J. N. Kutz, "On dynamic mode decomposition: Theory and applications," *J. Comput. Dyn.*, vol. 1, no. 2, pp. 391–421, Nov. 2014.

[49] C. W. Rowley, I. Mezić, S. Bagheri, P. Schlatter, and D. S. Henningson, "Spectral analysis of nonlinear flows," *J. Fluid Mech.*, vol. 641, p. 115, Nov. 2009.

[50] P. J. Schmid, "Dynamic mode decomposition of numerical and experimental data," *J. Fluid Mech.*, vol. 656, pp. 5–28, July 2010.

[51] L. N. Trefethen and D. Bau III, *Numerical Linear Algebra.* SIAM, 1997.

[52] A. Greenbaum, *Iterative Methods for Solving Linear Systems.* SIAM, 1997.

[53] Y. Susuki and I. Mezic, "Nonlinear Koopman modes and power system stability assessment without models," *IEEE Trans. Power Syst.*, vol. 29, no. 2, pp. 899–907, Mar. 2014.

[54] F. Raak, Y. Susuki, T. Hikihara, H. R. Chamorro, and M. Ghandhari, "Partitioning power grids via nonlinear Koopman Mode Analysis," in *ISGT 2014.* IEEE, Feb. 2014, pp. 1–5.

[55] P. Hémon and F. Santi, "Simulation of a spatially correlated turbulent velocity field using biorthogonal decomposition," *J. Wind Eng. Ind. Aerodyn.*, vol. 95, no. 1, pp. 21–29, Jan. 2007.

[56] N. Aubry, "On the hidden beauty of the proper orthogonal decomposition," *Theor. Comput. Fluid Dyn.*, vol. 2, no. 5-6, pp. 339–352, Aug. 1991.

[57] S. L. Brunton, J. L. Proctor, and J. N. Kutz, "Compressive sampling and dynamic mode decomposition," Dec. 2013. [Online]. Available: http://arxiv.org/abs/1312.5186

[58] M. R. Jovanović, P. J. Schmid, and J. W. Nichols, "Sparsity-promoting dynamic mode decomposition," *Phys. Fluids*, vol. 26, no. 2, p. 024103, Feb. 2014.

[59] Z. Zhong, C. Xu, B. Billian, L. Zhang, S.-J. Tsai, R. Conners, V. Centeno, A. Phadke, and Y. Liu, "Power system frequency monitoring network (FNET) implementation," *IEEE Trans. Power Syst.*, vol. 20, no. 4, pp. 1914–1921, Nov. 2005.

[60] V. Venkatasubramanian, "Oscillation monitoring from ambient PMU measurements by frequency domain decomposition," in *2008 IEEE Int. Symp. Circuits Syst.* IEEE, May 2008, pp. 2821–2824.

[61] A. V. Oppenheim and R. W. Schafer, *Discrete-Time Signal Processing.* Pearson Education, 2011.

[62] J. Grosek and J. N. Kutz, "Dynamic mode decomposition for real-time background/foreground separation in video," Apr. 2014. [Online]. Available: http://arxiv.org/abs/1404.7592

[63] G. C. Bourantas, M. Ghommem, G. C. Kagadis, K. Katsanos, V. C. Loukopoulos, V. N. Burganos, and G. C. Nikiforidis, "Real-time tumor ablation simulation based on the dynamic mode decomposition method," *Med. Phys.*, vol. 41, no. 5, p. 053301, May 2014.

[64] D. Duke, J. Soria, and D. Honnery, "An error analysis of the dynamic mode decomposition," *Exp. Fluids*, vol. 52, no. 2, pp. 529–542, Dec. 2011.

[65] S. Mohapatra and T. J. Overbye, "Real-time modal identification, monitoring, and visualization for large-scale power systems using dynamic mode decomposition," submitted for publication.

[66] Western Electricity Coordinating Council, "Oscillation detection and analysis applications in WECC," Western Electricity Coordinating Council, Salt Lake City, Utah, Tech. Rep., 2013.

[67] Electric Power Group, "Phasor grid dynamics analyzer," Pasadena, CA. [Online]. Available: http://www.electricpowergroup.com/solutions/pgda/

[68] PowerWorld Corporation, "PowerWorld FFT and Modal Analysis Tools," Champaign, IL, Tech. Rep., 2014. [Online]. Available: http://www.powerworld.com/files/clientconf2014/08OverbyeModalAnalysis.pdf

[69] J. Peng and N. Nair, "Effects of sampling in monitoring power system oscillations using on-line Prony analysis," in *Power Eng. Conf.* IEEE, 2008, pp. 1–5.

[70] J. L. Proctor, S. L. Brunton, and J. N. Kutz, "Dynamic mode decomposition with control," Sep. 2014. [Online]. Available: http://arxiv.org/abs/1409.6358